MINISTRY OF EDUCATION

FEDERAL UNIVERSITY OF RIO GRANDE DO SUL

School of Engineering

Post-graduation Program in Mining, Metallurgy and Materials

PPGE3M

ANNULUS CO_2-CORROSION OF HIGH STRENGTH STEEL WIRES FROM UNBOUNDED FLEXIBLE PIPES

(Corrosão por CO_2 de arames de aço de alta resistência mecânica provenientes de dutos flexíveis de camadas não aderentes)

RICARDO FEYH RIBEIRO

Thesis submitted for the degree of Doctor of Philosophy in Engineering.

Porto Alegre

June 2019

RICARDO FEYH RIBEIRO

Annulus CO$_2$-corrosion of high strength steel wires from unbounded flexible pipes

A study conducted at the Department of Metallurgy from School of Engineering of UFRGS within the Graduate Program in Mining, Metallurgy and Materials - PPGE3M, as part of the requirements for obtaining the title of Doctor of Philosophy in Engineering.

Concentration Area: Science and Technology of Materials

Advisor: Prof. Dr. Carlos E. F. Kwietniewski

Porto Alegre

June 2019

RICARDO FEYH RIBEIRO

Corrosão por CO_2 de arames de aço de alta resistência mecânica provenientes de dutos flexíveis de camadas não aderentes

Trabalho realizado no Departamento de Metalurgia da Escola de Engenharia da UFRGS, dentro do Programa de Pós-Graduação em Engenharia de Minas, Metalúrgica e de Materiais –PPGE3M, como parte dos requisitos para obtenção do título de Doutor em Engenharia.

Área de Concentração: Ciência e Tecnologia dos Materiais

Advisor: Prof. Dr. Carlos E. F. Kwietniewski

Porto Alegre

Junho 2019

RICARDO FEYH RIBEIRO

Annulus CO_2-corrosion of high strength steel wires from unbounded flexible pipes

This dissertation was deemed adequate to obtain a PhD degree in Engineering, area of concentration in Science and Technology of Materials, and approved in its final form, by the advisor and by the examining board of the Postgraduate Program.

Advisor: Prof. PhD. Carlos Eduardo Fortis Kwietniewski

Coordinator of PPGE3M: Prof. Dr. Carlos Pérez Bergmann

Examining board:

Prof. Dr. André Ronaldo Froehlich, UNISINOS

Prof. Dra. Cristiane Pontes de Oliveira, UFRGS

Prof. Dr. Tiago Falcade Nunes, UFRGS

Eu dedico esta dissertação a meus familiares, a minha esposa e a meus amigos.

ACKNOWLEDGEMENTS

ABSTRACT

Recent premature failures of unbounded flexible pipes brought life to the discussion of the detrimental effects of the CO_2 on the structural layers of unbounded flexible pipes. Flexibles are structures composed of several concentric layers of polymers and steel wires. The steel wires support the mechanical loads and reside inside a highly confined annulus space bounded by two polymer layers. The environment in this occluded annulus region evolves as water and other chemicals permeate from the produced fluid in the bore through the inner sheath, or from breaches in the outer sheath. As a result, the armour wires can be subjected to corrosion that needs to be considered against the service environment. The complexity of the annulus environment makes the study of corrosion in it challenging. Thus, understanding the interactions between the steel and the electrolyte is essential for reproducing the corrosion of the structural layers. Despite that, many occluded CO_2-corrosion tests are conducted in environments, which neither reproduce the state of the electrolyte, nor the mechanisms found in the field. Although some studies on corrosion in annulus environments have been published, there remains further work to be done to fully understand the extent of variables that may potentially affect the annulus corrosion rate and mechanisms within it, particularly concerning the effect of CO_2 permeation. The present study describes the corrosion rates of high strength carbon steel wires in brines with carefully controlled supply rates. A simulation of the gas flow rate was carried to study the permeation behaviour on severe CO_2 service conditions. Weight loss and electrochemical measurements were conducted to evaluate the corrosion rates. Pressure, temperature and composition of the brine, covering liquid, gaseous and supercritical states of CO_2 have been explored by simulation in search for critical patterns. The data in low pressure are compared to simulation and those of previous studies in the literature. The experiments show low corrosion rates and a clear dependence between the concentration of iron, pH, open circuit potential and corrosion rate. Changes in these properties were found to describe three stages of corrosion. No substantial influence on the maximum corrosion rate was seen after a two-fold increase in the CO_2 supply rate.

Keywords: Unbounded flexible pipes; annulus CO_2-corrosion; high strength steel; electrolyte simulation.

RESUMO

Recentes falhas prematuras de dutos flexíveis de camadas não aderentes trouxeram à luz a necessidade de debater os efeitos prejudiciais do CO_2 na deterioração das camadas estruturais da tubulação. Estes tubos flexíveis são estruturas compostas por camadas concêntricas de polímero e aço, nas quais as partes metálicas têm como objetivo suportar as cargas mecânicas. As condições ambientais do interior do componente evoluem à medida que água e outras espécies químicas adentram na região anular, que são provenientes do fluido transportado, ou de rupturas na capa externa. Em consequência disto, as armaduras metálicas podem estar sujeitas à corrosão. Assim, compreender as correlações entre as variáveis ambientais com as propriedades do metal é vital para o entendimento do processo e da reprodução do dano na estrutura. Porém, a complexidade do ambiente anular torna o estudo desafiador. Por esta razão, muitos estudos encontrados na literatura foram conduzidos em ambientes que não reproduzem o ambiente anular, nem os mecanismos observados em campo. De fato, ainda há muito a ser feito para compreender o processo, particularmente no que diz respeito ao efeito da permeação de CO_2 na corrosão das armaduras de tensão. Neste aspecto, o presente trabalho tem como objetivo descrever a corrosão dos arames de aço carbono de alta resistência mecânica em solução contendo 3,5% de NaCl sob condições controladas de fluxo de CO_2. As simulações do fluxo de gás foram realizadas visando representar a permeação em condições de serviço severo. As taxas de corrosão foram avaliadas por técnicas eletroquímicas e de perda de massa. As variáveis do ambiente, pressão, temperatura e composição da solução, foram explorados por simulações cobrindo os estados líquido, gasoso e supercrítico do CO_2 em busca de padrões críticos de corrosão. Os resultados obtidos nos experimentos foram comparados com simulações e com dados encontrados na literatura. Os experimentos mostram baixas taxas de corrosão e uma clara dependência entre a concentração de ferro, o pH, o potencial de circuito aberto e as taxas de corrosão. Alterações nestas propriedades descrevem três estágios. A taxa máxima de corrosão não foi significativamente afetada pelo aumento de duas casas decimais no fluxo de gás.

Palavras chave: Dutos flexíveis de camadas não aderentes; Corrosão por CO_2 do espaço anular; Aço de alta resistência mecânica; Simulação do eletrólito.

FIGURES

TABLES

LIST OF ABBREVIATIONS

$\emptyset_i$	Potential to move an electrical charge between two points
$\mathcal{E}$	Electric potential difference
$\mathcal{E}^0$	Electric potential under the standard states
ΔG	Gibbs free-energy exchange
ΔG^0	Gibbs free-energy exchange at standard conditions
a	Activities of the main species
a_j^0	Ion-specific parameter
a_{ox}	Activity of the chemical species being oxidized
a_{red}	Activity of the chemical species being reduced
B	Stern Geary Factor
b_a	Anodic slope
b_c	Cathodic slope
b_j	Ion-specific parameter
c	Concentration of chemical species
C	Constant
$C1$	Constant 1
$C2$	Constant 2
$C3$	Constant 3
$C4$	Constant 4
C_a	Anodic constant
C_c	Cathodic constant
CR	Corrosion rate
CR_{LPR}	Corrosion rate given by LPR
CV	Cyclic Voltammetry
DIC	Dissolved inorganic carbon
E	Electric potential
e	Margin of error
$E'_{I,II,III}$	Constants of reduction potentials regarding the three stages of the steel surface
E_{corr}	Corrosion potential
EOR	Enhanced Recovery of Oil
EW	Equivalent weight of the steel,
F	Faraday constant (96,487 coulombs)
FR/SS	Flow rate of gas per surface of the steel
G	Gibbs free energy
$HDPE$	High-density polyethylene
HSS	High strength steels
I	Current
i	Current density
I_0	Net current
I_a	Anodic current
i_a	Anodic current density
I_c	Cathodic current
i_c	Cathodic current density
j_{corr}	Corrosion current density
IS	Ionic strength

k	Rate of the reaction
K_1	Equilibrium constant
K_2	Equilibrium constant
K_H	Henry's equilibrium constant
K_w	Equilibrium constant
LPR	Linear polarization resistance
LSV	Linear sweep voltammetry
m_1	Initial weight of the corrosion coupon
m_2	Weight of the corrosion coupon after the end of the experiment
m_3	Weight of the corrosion coupon after complete removal of the corrosion scale
M^{n+}	Metal ion
MPT	Mixed potential theory
$MWFeCO_3$	Molecular weight of iron carbonate
N	Inlet nozzle
n	Number of electrons exchanged
n_n	Number of moles of given substance in a mixture
OCP	Open circuit potential
P	Pressure
$P_1^{v"}$	Vapour pressure of water
PA11	Polyamide 11
PA12	Polyamide 12
PA6	Polyamide 6
pCO_2	Partial pressure of CO_2
pP	Partial pressure of a given chemical component
P_T	Total pressure
PVDF	Polyvinylidene difluoride
R	Universal gas constant (8.3144621 J.K^{-1}.mol^{-1})
R_b	Rate of the backward reaction
R_f	Rate of the forward reaction
Rp	Polarization resistance,
S	Surface area of the steel
SCC	Stress corrosion cracking
SCE	Standard Calomel Electrode
Sd	Sample standard deviation
SHE	Standard Hydrogen Electrode
ST	Scaling tendency
T	Temperature
t	Time
V/S	Degree of occlusion or free volume to steel surface area
W	Chemical species
w	Stoichiometric coefficient of the chemical species W
WE	Working electrode
X	Chemical species
x	Stoichiometric coefficient of the chemical species X
x_j	Mole fraction of component "j" in the liquid
XRD	X-ray diffraction
Y	Chemical species
y	Stoichiometric coefficient of the chemical species Y
y_j	Mole fraction of component "j" in the liquid
Z	Chemical species
z	Stoichiometric coefficient of the chemical species Z
z_j	Valence of ion j
$Z_{\alpha/2}$	Confidence level

α	symmetry factor
$\gamma_{\pm}$	Activity coefficient
η	Overpotential
η_a	Anodic overpotential
η_c	Cathodic overpotential
ρ	Density of the steel

SUMMARY

1. INTRODUCTION

Fossil fuel should remain the dominant source of energy until 2040, despite the efforts of replacing it with renewable sources. Therefore, in the absence of easy oil extraction, countries that have reserves are compelled to invest in more efficient ways of exploiting oil in areas that require greater technological efforts, such as the deep waters of the Brazilian pre-salt. In line with this statement, the transport of oil and gas with flexible pipe technologies has been gaining importance in recent years. In Brazil, a large portion of the crude oil is transported via flexibles, because these ducts are well suited to operate for long periods without or with little maintenance in very aggressive environments (4SUBSEA, 2013; AMERICAN PETROLEUM INSTITUTE, 2008; FERGESTAD; LØTVEIT, 2014; ORGANIZATION OF THE PETROLEUM EXPORTING COUNTRIES, 2017; PETROBRAS, 2015).

Aside from oil extraction, some oil operators opt to employ unbounded flexible pipes for the reinjection of carbon dioxide into the wells in a process called Enhanced Recovery of Oil (EOR). EOR is designed to avoid the release of gas into the atmosphere while maximising the yield from a reservoir by raising the well pressure. However, despite the significant advantages of reinjection of CO_2 with unbounded flexibles, highly pressurised CO_2 and seawater may permeate from the bore through polymer barriers. The presence of water, salt and noxious chemicals in the annulus can potentially corrode the structural layers of the pipe severely, causing damage to the environment or financial losses. Thus, it is clear that the corrosion assessment of these layers is paramount to calculating the lifetime of unbounded flexible pipes (4SUBSEA, 2013; DÉSAMAIS; TARAVEL-CONDAT, 2009; DOS SANTOS, 2011; FERGESTAD; LØTVEIT, 2014; HAAHR et al., 2016; LANGLO, 2013; LEMOS, 2009; PAUL, 2010; SANTOS et al., 2013, 2013; TARAVEL-CONDAT; GUICHARD; MARTIN, 2003; THOMAS, 2012).

However, the corrosion of the annulus is a challenging field of science. For example, monitoring the evolution of pH and composition of the solution could be difficult. Because, if not carefully thought and executed, the simple process of extracting aliquots may significantly change the degree of occlusion or, even, increase the risk of contamination of the solution by oxygen. The permeation rates of the gases and water entering the annulus are still misunderstood fields. In addition, the practical limitations attributed to the geometry and operation of the pipe make the corrosion process challenging to reproduce. Aside from those, many other restrictions could also apply to the traditional electrochemical techniques, such as the arrangement of the electrodes (ERIKSEN; ENGELBRETH, 2014).

Hence, this work aims at improving the understanding of corrosion in the annulus environment and occluded CO_2-corrosion, thus enhancing the ability to make predictions of risk and life assessments. The focus is driven towards the electrochemical correlations between the corrosion rate with other variables in a dense packed corrosion cell at a low flow rate regime of CO_2. The most standard corrosion tests employ relatively high flow rates to obtain saturated solutions from the start of a test, which contrasts with the relatively slow establishment of the annulus conditions evolving in service. Experimental data are compiled and compared with simulations and literature. Pressure, temperature and composition of the 3.5%wt. NaCl brine are also critical factors explored, searching for plausible states of confined electrolytes that could induce critical corrosion patterns. The fact that the degradation of metals by aqueous corrosion essentially relies on the electrochemical interaction between the electrolyte and the surface of materials serves to justify this approach.

1.1. OBJECTIVES

1.1.1. General objectives

This work proposes an investigation of the annulus environment of flexible pipes. It aims at understanding of the environment, the corrosion process and products. The focus is driven to the study of dense-packed tests and simulation of the electrolyte. It is expected the production of novel data regarding the relationship between parameters. The work is intended to contribute to the improvement of life assessments and industry standards and practices.

1.1.2. Specific objectives

This work contains the following specific objectives:

• Replicate the annulus CO_2-corrosion aiming at the obtainment of data and evidence that contribute to the selection of materials for the metallic layers of flexible lines.
• Investigation of parameters affecting the annulus CO_2-corrosion of unbounded flexible pipes. Attention is given to the combination of parameters of flow rate of CO_2, composition of the electrolyte, pressure and temperature, which were not entirely addressed by the literature.
• Comparison of experimental data obtained in laboratory to models of the electrolyte and literature.

- Investigate the appearance and composition of the corrosion product.

- Investigate properties of the system and electrolyte.

- Search for critical corrosion patterns through modelling the electrolyte.

- Produce novel data, in order to reduce conservatism regarding the corrosion of flexible pipes

1.2.   BENEFITS TO INDUSTRY

Flexible risers are modern technologies and particularly complex structures. The full integrity life has not been achieved, and gaps related to the lack of complete analysis of the failure and degradation mechanisms remains (Figure 1). As a result, life assessments continue challenging and unreliable (4SUBSEA, 2013; FERGESTAD; LØTVEIT, 2014). Regardless, the use of flexible risers has increased in the past two decades. For instance, the use of flexible risers in the Norwegian petroleum production grew from around 50 to 326, between the years of 1993 to 2013. In turn, the broad usage of flexible pipes is followed by a higher risk of failure (see Figure 2) (4SUBSEA, 2013).

Figure 1: Sketch of the lifetime attribution of flexible pipes.
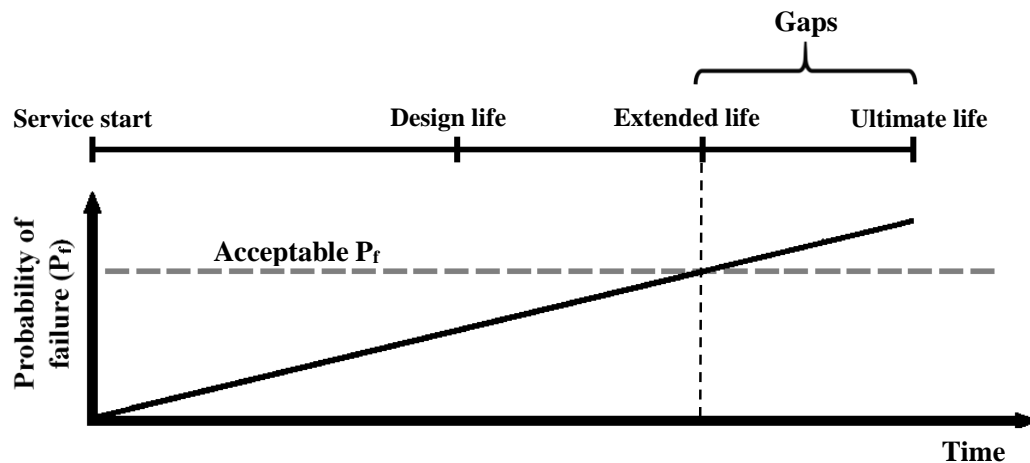
Source: Adapted from (FERGESTAD; LØTVEIT, 2014).

Figure 2: Norwegian statistics of the major incidents rate per riser operational year.
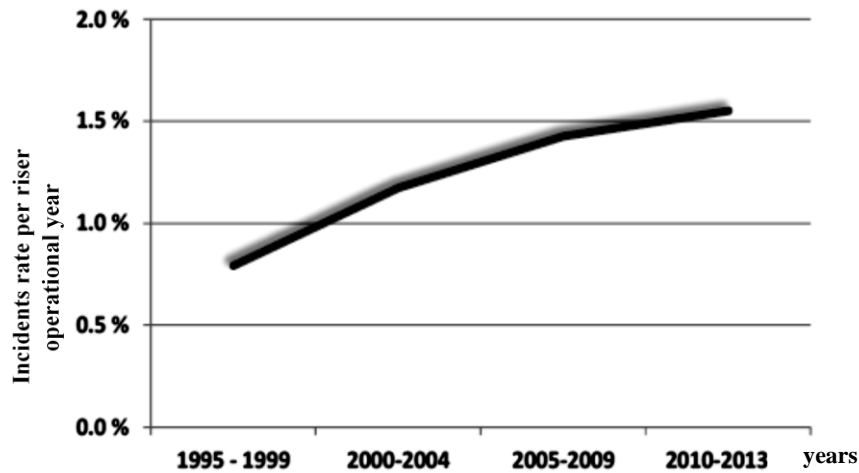
Source: Adapted from (4SUBSEA, 2013).

The leading causes of serious failures are the inadequate qualification for service and appreciation of the failure mechanisms. To overcome these uncertainties, the conventional engineering assessment procedures start with simple and highly conservative analysis, even though such assumptions usually lead to sub-optimal designs and may prohibit the usage of the pipelines under perfectly safe environmental conditions. As a result, one could expect a significant financial loss, due to premature maintenance or inaccurate design of components.

At this point, to better understand the operating limits, provide enhanced life predictions and cost-effective operations, the oil and gas industry requires not only additional knowledge of materials corrosion but also continuous updates of the industry standards, practices and guidelines. Advances in such areas allow that more rigorous and complex analysis be performed on a routine basis, encompassing more complex materials and structural responses. Novel data and deepening in the available knowledge on the occluded CO_2-corrosion are in order to support more complex analysis, that lead to enhancing of the current- or design life of flexible pipelines (4SUBSEA, 2013; FERGESTAD; LØTVEIT, 2014).

## 2.	LITERATURE REVIEW

The literature review has been divided into four subjects, as follows: unbounded flexible pipes, general aspects of corrosion, annulus environment and corrosion of unbounded flexible pipes. Due to the considerable number of uncertainties commonly attributed to the subject of this work, the first three chapters were drafted in order to provide a foundation for the forthcoming sections (CO_2-corrosion of flexible pipes, methodology and results).

## 2.1.	UNBOUNDED FLEXIBLE PIPES

Unbounded flexible pipes represent one option available for the transport of hydrocarbons from the seabed to the production units. The term "unbounded" embody a constructive peculiarity of the design, regarding the relative movement between the constitutive parts of the structure. Flexible pipes are comprised of several concentric layers of steel and polymer. The particular constructive design enables low bending stiffness combined with substantial axial tensile stiffness. Consequently, long sections of pipes can be prefabricated, spooled, stored and transported in offshore reels. In other words, unbounded flexible pipes simplify the stages of fabrication, transport and installation in comparison to rigid pipes. While each flexible tube is designed for specific applications, the structures can be re-deployed with relative ease in configurations such as risers, flowlines or jumpers (4SUBSEA, 2013; BORGES, 2017; BRAESTRUP et al., 2005; FERGESTAD; LØTVEIT, 2014; TECHNIP, 2015).

### 2.1.1.	Structure

Unbounded flexible pipes are comprised from the inner diameter to the outer diameter of the following parts: carcass, inner sheath, pressure armour, backup pressure armour, anti-wear layers, tensile armour, holding bandage and outer sheath (see Figure 3). The volume between the polymeric layers is called the annulus. (AMERICAN PETROLEUM INSTITUTE, 2008; BRAESTRUP et al., 2005).

Figure 3: Scheme of an unbonded flexible pipe structure.
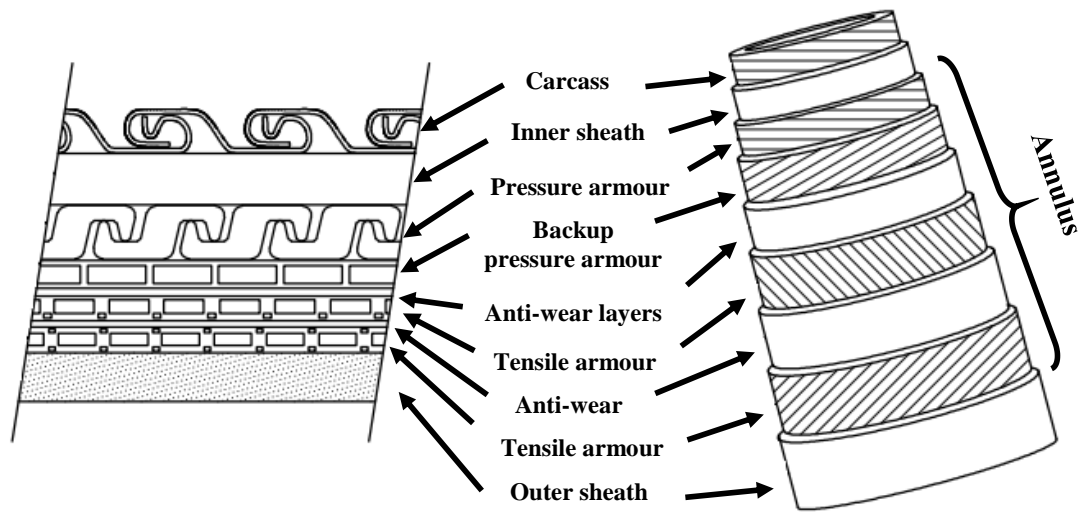
Source: Adapted from (AMERICAN PETROLEUM INSTITUTE, 2008).

Each layer has a unique shape and specific functions. According to the literature, (AMERICAN PETROLEUM INSTITUTE, 2008; BORGES, 2017; BRAESTRUP et al., 2005; DE SOUSA, 1999; DE SOUSA et al., 2014; XAVIER, 2009) the main layers are described as follows:

• Carcass: often produced in stainless steel (AISI 304/304L, AISI 316/316L, UNS 2507, UNS 2205, UNS 2750) or nickel-based alloys. The carcass is a structural layer of the pipe designed to support radial loading and prevent excessive ovalisation, erosion, yielding, abrasion and collapse when empty. The innermost surface has physical contact with the product being transported, even though it is not leak proof. Therefore, the selection of materials shall focus not only on mechanical aspects but also on compatibility with the internal fluids being transported.

• Inner sheath: layer made from extruded polymers, typically polyamide 11 (PA11), high-density polyethylene (HDPE) or polyvinylidene difluoride (PVDF). The polymeric sheath is designed for the chemical containment of the bore fluid. The chemical composition of the annulus is highly dependent on the permeation properties of the material employed in this layer.

• Pressure armour: the pressure armour consists of tight helix inter-locking carbon steel wires, designed to endure the internal and external pressures. This structural layer is found confined in the annulus, presenting one of the four possible shapes as shown in Figure 4.

Figure 4: Profile geometries of the pressure armour. a) Z-shape. b) C-shape. c) T-shape 1 with clip. d) T-shape.
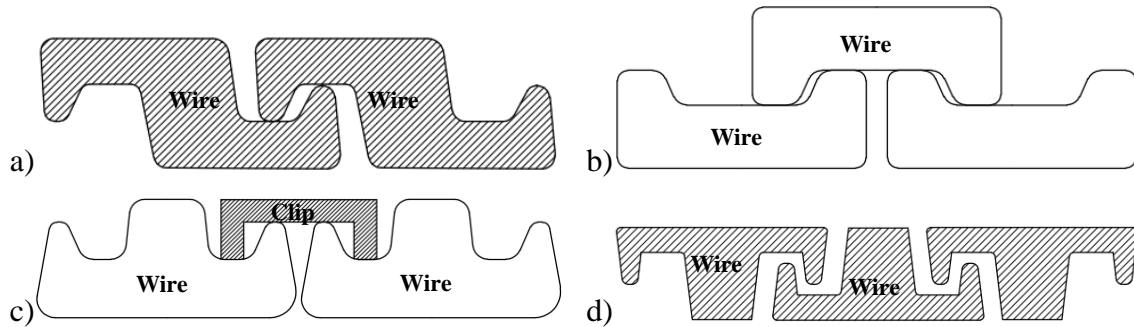
Source: Adapted from (AMERICAN PETROLEUM INSTITUTE, 2008).

• Backup pressure armour: the backup pressure armour is an optional structural layer used for higher-pressure applications, consisting of flat shaped wires of carbon steel disposed in helicoidal fashion. The chemical compositions of the steel is usually similar to the employed in the pressure armour (UTS ranging from 700 to 900 MPa).

• Anti-wear layers: anti-wear layers are made from polymeric tapes (e.g. PA6, or PA11), and is designed to prevent wear and improve fatigue performance. The layer minimises friction by separating the metallic armour layers. Anti-wear tapes are optional for static applications.

• Tensile armour: "the tensile-armour layers often use flat, or round, or shaped metallic wires, in two or four layers crosswound at an angle between 20° and 60°". (AMERICAN PETROLEUM INSTITUTE, 2008, p. 15). The layer is designed to support axial, hoop and torsional loads. The angle of the wires dictates the stiffness of the structure according to each stress. The microstructure and chemical composition of the steel is selected considering each application. High strength steels (HSS) are usually preferred for deep-water developments.

• Holding bandage: the holding bandage is applied around the tensile armours as a manufacturing aid to prevent failure by "birdcaging", that is the buckling of the tensile-armour wires caused by extreme axial compression. The bandages are used to control the radial displacement of the tensile armour wires. The material consists of a fibre-reinforced polymer.

• Outer sheath: the outer sheath is typically built from extruded polymers (PA11, or PA12, or HDPE). It is designed to accommodate the tensile armour and to prevent direct contact between seawater and wires. It should be stressed that the integrity of the material confined in the annulus depends to a large extent on the permeation and mechanical properties of the material used in the outer sheath.

2.1.2. End-Fittings

End fittings are the terminations attached to both ends of the flexible pipe. Various geometries exist, such as bolted flanges, clamp hubs and welded joints. A typical end-fitting system is shown in Figure 5. The main functions are to provide a pressure-tight transition between the pipe body and the connector and to transfer the loads sustained by the structural layers (axial and bending) against the vessel structure (AMERICAN PETROLEUM INSTITUTE, 2008; BAI; BAI, 2010).

Figure 5: End-fitting system.
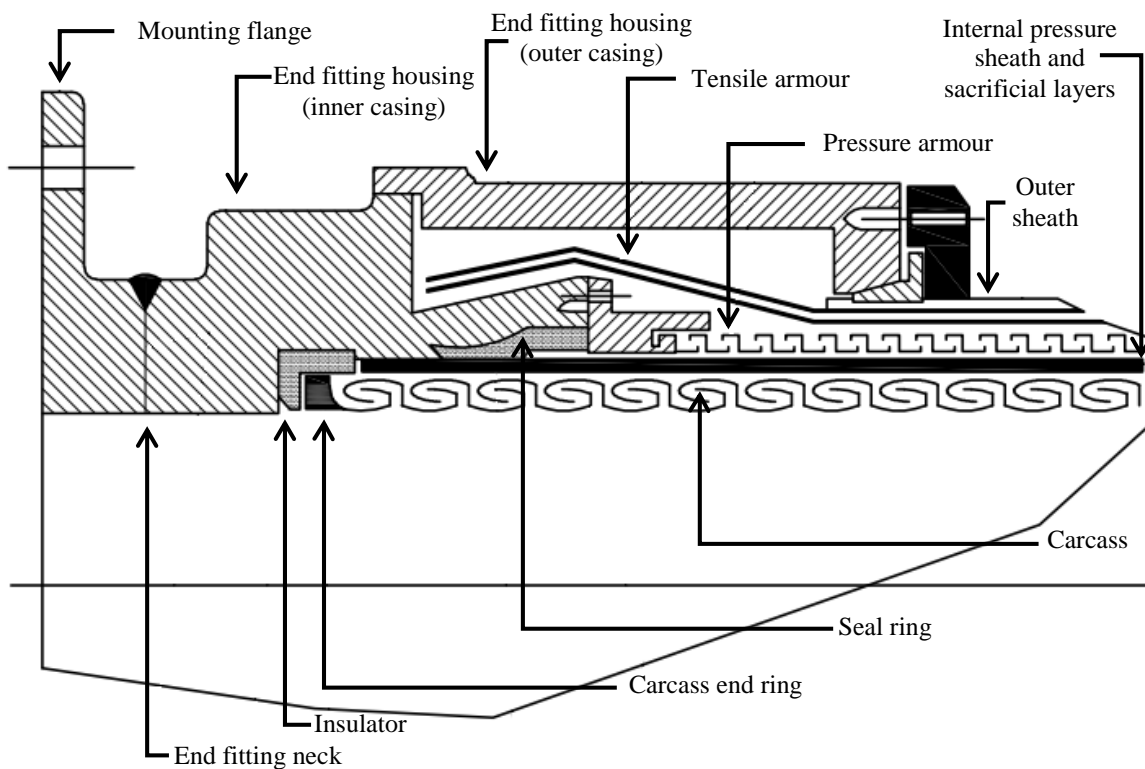
Source: Adapted from (AMERICAN PETROLEUM INSTITUTE, 2008).

2.1.3. Annulus venting system

During normal operation, the gas molecules and water tend to permeate from the bore to the annulus, so, unless ventilated, the pressure will build up in the annulus until bursting of the outer sheath occurs. Therefore, to prevent an excessive increase in the pressure of the pipe the structure incorporates a venting system. The venting valve is designed to open at specific pre-determined pressures.

2.1.4. Classification of unbounded flexible pipes

Unbounded flexible pipes are distinguished according to the location in the field, application and constructive characteristics. The distinction is made possible by the modular aspect of the tubes, which allows fit-for-purpose constructions. Standard API RP 17B (AMERICAN PETROLEUM INSTITUTE, 2008) classifies the unbounded flexibles according to 3 families. The main distinguishing features are the presence (or absence) of carcass and pressure armours (see Table 1).

Table 1: Classification and constructive features of the standard unbounded flexible pipes.

	Product family I (smooth bore)	Product family II (rough bore)	Product family III (rough bore, reinforced pipe)
Carcass	Absent	Yes	Yes
Inner sheath	Yes	Yes	Yes
Pressure armour	Yes	Absent	Yes
Tensile armour	Yes	Yes	Yes
Outer sheath	Yes	Yes	Yes
Internal fluids:	Fluids, not containing gas or particulates	Water/gas/chemicals containing gas or particulates	Water/gas/chemicals containing gas or particulates
Applications:	Water injection	Extraction and transport of oil	Injection and exportation
Temperatures:	-50 to +130 °C	-50 to +130 °C	-50 to +130 °C
Pressures:	Lower external pressures	Moderate external pressures	High external pressures

Source: Adapted from (BORGES, 2017; GLEJBØL, 2011; NOV, 2015; XAVIER, 2009).

The carcass is the element absent in family I; thus, the inner sheath functions as the primary barrier for the fluid being transported. So, to prevent excessive wear of the inner sheath by erosion, family I pipes shall not carry fluids containing particulates. Moreover, to avoid collapse by rapid depressurisation, the fluid shall not contain gas. Otherwise, rapid decompression of the gas would result in massive expansions within the annulus, forcing the polymer sheath to collapse. Moreover, given the absence of the carcass, the pressure armour is integrally responsible to withstand the mechanical loads respective to the pressure of the internal fluid and to absorb the crushing force, resultant from the combination of the external pressure and the squeeze exerted by the axial loads on the tensile armour (BORGES, 2017; GLEJBØL, 2011; XAVIER, 2009).

Unbounded flexible pipes belonging to family II comprise a carcass but not a pressure armour. Therefore, by being the inner sheath protected against wear and collapse of the

structure, the fluids can contain gases and abrasive particles. Moreover, given the absence of pressure armour, the carcass becomes the element responsible for preventing the collapse of the structure (AMERICAN PETROLEUM INSTITUTE, 2008). Also, according to Xavier (2009), family II pipes are preferred in situations where the internal pressure is moderated.

When the inner sheath of a family I pipe is protected by the addition of a casing, the pipe can be classified as family III pipe. Since the carcass is present, the fluids may contain gases and abrasive particles. Furthermore, the family III is intended to maintain safe operation in deep-water developments where hydrostatic pressures are high. Under such circumstances, the duct may even receive an additional backing layer to support the mechanical loads corresponding to the pressures and to support the collapse of the structure (GLEJBØL, 2011; XAVIER, 2009).

Unbounded flexibles can also be distinguished according to the application in the field, working as flowlines, jumpers or risers. Flowlines transport fluids over vast distances at the seabed. Jumpers are employed to transport fluids between subsea components. Risers transport fluids between subsea structures towards a production unit. Risers can be grouped according to depth because mechanical and environmental requirements change drastically between locations.

The usages of unbounded flexible pipes include production, injection, exportation and service applications, giving place to another classification: static or dynamic applications. On the one hand, static applications involve the interaction between the pipe and the soil. Among the many benefits of the usage of flexibles for static applications are mitigating issues related to misalignment of equipment, large movements and damage to the structures caused by mudslides. On the other hand, dynamic applications involve the interactions of the structure to the tidal action, where there is relative movement between the source and delivery points during service. In general, dynamic pipes require pliancy and high fatigue resistance. Internal and external damage resistance and minimal maintenance are also properties necessary for both static and dynamic applications (AMERICAN PETROLEUM INSTITUTE, 2008).

2.1.5. Ancillary components

Ancillary components, such as sacrifice anodes, bend-limiters, bend restrictors, buoyancy modules are structures fitted in unbounded flexible pipes, in order to ensure safe operation and to prevent early damage to the structure. Exceeding their limits may cause serious failures or allow the ingress of seawater into the annulus (4SUBSEA, 2013).

2.1.5.1. Sacrifice anodes

Sacrifice anodes are components used to reduce or eliminate corrosion by making the metal a cathode, which is achieved in flexible pipes by means of attaching highly active materials such as Zn, Mg or Al to the end fittings (BAI; BAI, 2010; DAVIS, 2000; FERGESTAD; LØTVEIT, 2014).

Despite being a traditional technique used in many offshore structures, experience shows that cathodic protection of the structural layers of flexible pipes by sacrifice anodes or impressed current cathodic protection systems is not effective (see Figure 6). Cases of corrosion on tensile and pressure armours have been reported, usually associated with damage or rupture of the outer sheath. The inefficiency of the technique lies on its inherent limitations, some of which are listed as follows (DAVIS, 2000; ERIKSEN; ENGELBRETH, 2014; GENTIL, 2011; JOEL, 2009; MUREN, 2007):

i.   The electrochemical system shall always comprise an anode (sacrificial anode), a cathode, an ionic path and electrical contact. If one or more of these parts is missing, the steel would not be protected.

ii. Electrochemical potential difference between the anode and cathode shall be significant. Meaning that the steel may not be protected, if the flooded section is located far from the anodes.

iii. Sufficient electrical energy (amperes.hour/kg of steel) shall be provided to ensure long-term protection to the steel. In other words, the sacrificial anode cannot corrode much faster than the life expectancy of the pipe.

iv. The corrosion of the anode cannot form passive layers, where the sacrificial anode becomes nobler than the steel. Changes of the environment may induce the formation of unexpected scales on the anode leading to the galvanic corrosion of the steel.

v.   Cathodic protection does not protect the steel against local galvanic couples. For example, if the copper from electrical wires in contact with the pipe is unprotected against the electrolyte.

vi. Electrical interference from other protected pipes can cause corrosion on the steel. In other words, electrical interference may induce stray current corrosion, where a current leakage can cross unintentionally a near-by unprotected structure leading to severe corrosion.

Figure 6: Corrosion caused by a rupture of the outer sheath and ineffective cathodic protection.
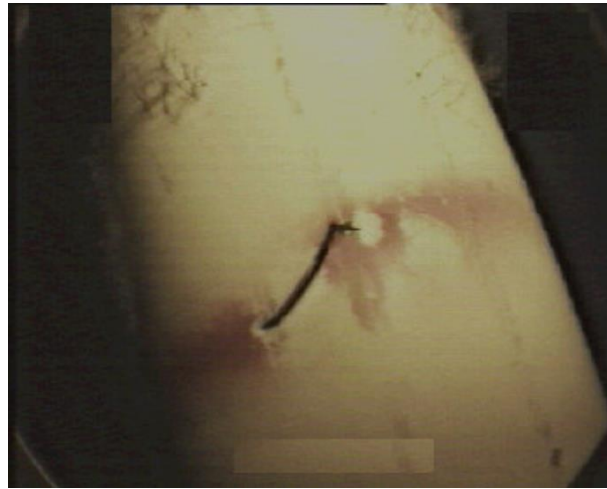
Source: (MUREN, 2007).

2.1.5.2. Bend limiters: bend stiffeners and bellmouths

The top hang-off region is typically the most susceptible zone for mechanical damage in risers. The unbounded pipes are protected from excessive bending in this zone by bend limiters, bend stiffener or bellmouth (see Figure 7). Bend stiffeners and bellmouths are built from Polyurethane. These structures are designed to provide smooth transitions of stiffness, to prevent excessive bending and to avoid stress concentration at the end fitting. The fatigue life of these ancillary components shall be equal to or larger than the fatigue life of the pipe because they cannot be replaced during operation (BAI; BAI, 2010; BORGES, 2017).

Figure 7: Scheme of a bend limiter.
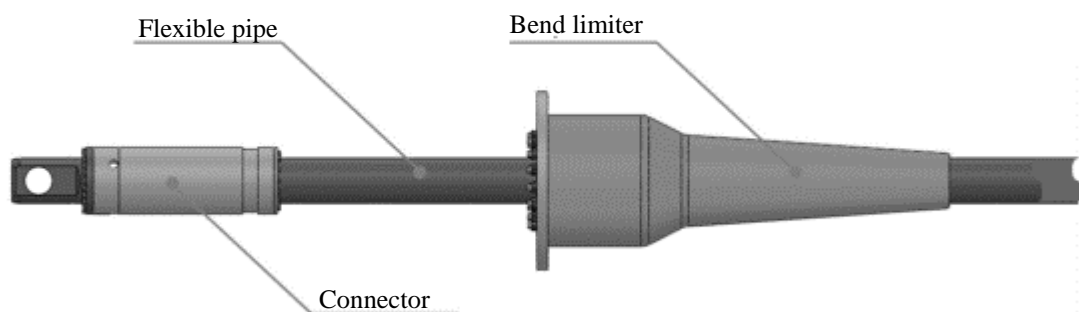
Source: (BORGES, 2017).

2.1.5.3. Bend restrictors

Bend restrictors are structures, manufactured from metallic materials, creep-resistant elastomers or fibre-glass-reinforced plastic (see Figure 8). They are designed to control the bending of the flexible pipe, preventing overbending during installation or operation. "The restrictor consists of interlocking half rings that fasten together around the pipe so that they do not affect the pipe until a specified bend radius is reached, at which stage they lock" (AMERICAN PETROLEUM INSTITUTE, 2008, p. 26). When the bend restrictors are in the locked position, they support the additional loads, preventing further bending of the pipe.

Figure 8: Bend restrictor.
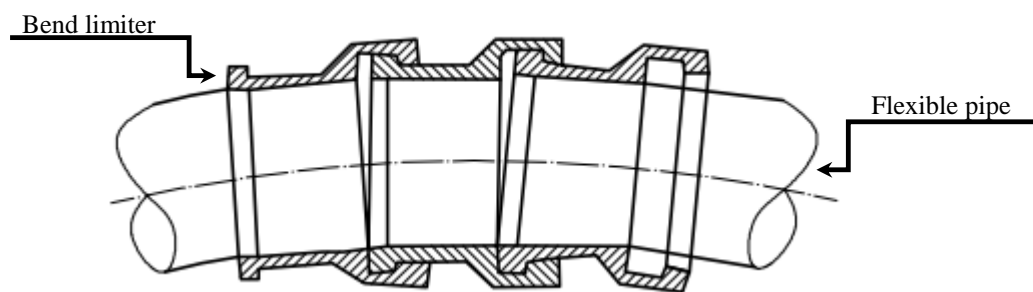
Source: Adapted from (AMERICAN PETROLEUM INSTITUTE, 2008).

2.1.5.4. Subsea buoys and buoyancy modules

Subsea buoys are installed to achieve S-shaped riser configurations and to provide a reduction on the top tension loads (see Figure 9). The structures are manufactured from steel or synthetic foam. Buoyancy modules can be attached to the pipe in order to provide uplift and maintain the specific riser configurations. The buoyancy elements are manufactured from synthetic foam involved by polyurethane casing. The casing provides impact and abrasion resistance, while the foam offers the uplift (AMERICAN PETROLEUM INSTITUTE, 2008; TRELLEBORG, 2018).

Figure 9: Subsea buoys connected to flexible pipes.
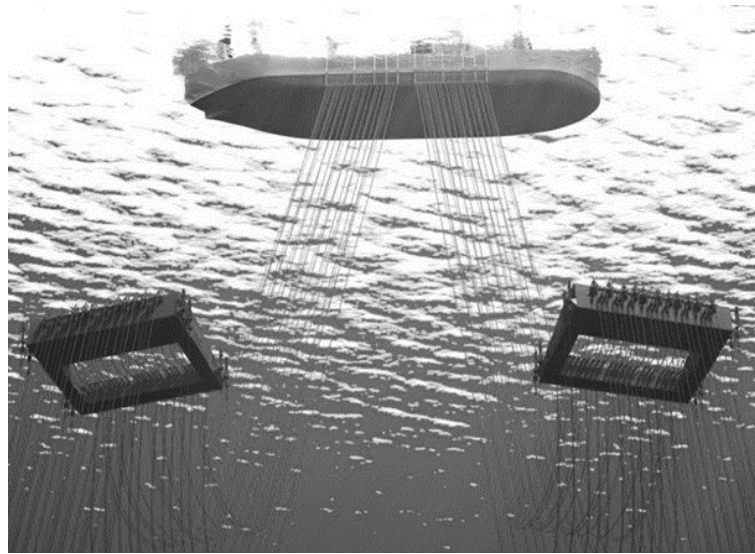
Source: (WORLEYPARSONS, 2015).

2.1.6.   Risers configurations

Figure 10 illustrates examples of riser configurations recommended by the API RP 17B standard. The geometric configuration of unbounded flexible pipes reflects the physical demands on the structure, including self-weight and all other static and dynamic loads respective to assembly and operation. The most critical sections are where the tensile forces are higher, usually at the top, or at large curvatures, sag or hog bends. Therefore, each configuration must be selected to reduce the mechanical stress while keeping the structure economically viable. For example, free-hanging catenary minimises the costs by reducing the total length of the pipeline and usage of ancillary components. However free-hanging catenary is not always applicable given the large stresses found at the topside. Steep-S, Steep Wave, Lazy-S and Lazy Wave configurations aim to reduce top traction due to the weight of the duct itself and minimise the effect of platform movements in the region where the flexible duct rests on the seabed (AMERICAN PETROLEUM INSTITUTE, 2008; BORGES, 2017).

Steep Wave and Lazy Wave configurations contain buoyancy and weight along the length of the riser. The emphasis is on decoupling the vessel motions from the touch down point of the riser. On the one side, Lazy Wave layout require minimal subsea infrastructure, on the other side Steep Wave configuration require a subsea base and subsea bend stiffener. Steep Wave configuration have the advantage of maintaining configuration when the fluid density changes (BAI; BAI, 2019).

In the S-type configurations (Steep-S and Lazy S) a subsea buoy or a buoyant buoy are employed to reduce the risk of mechanical damage in the touchdown point, because the buoy absorbs the loads induced by the floater and the structure at the touchdown point. Due to the complex installation, S-type configurations are only considered if catenary and wave configurations are not suitable (BAI; BAI, 2019). "A lazy-S configuration requires a mid-water arch, tether and tether base, while a steep-S requires a buoy and subsea bend stiffener (BAI; BAI, 2019, pg. 403)".

Figure 10: Five examples of riser configurations recommended by Standard API RP 17B.

a) Free-hanging catenary

b) Steep-S   c) Lazy-S

d) Steep wave   e) Lazy wave
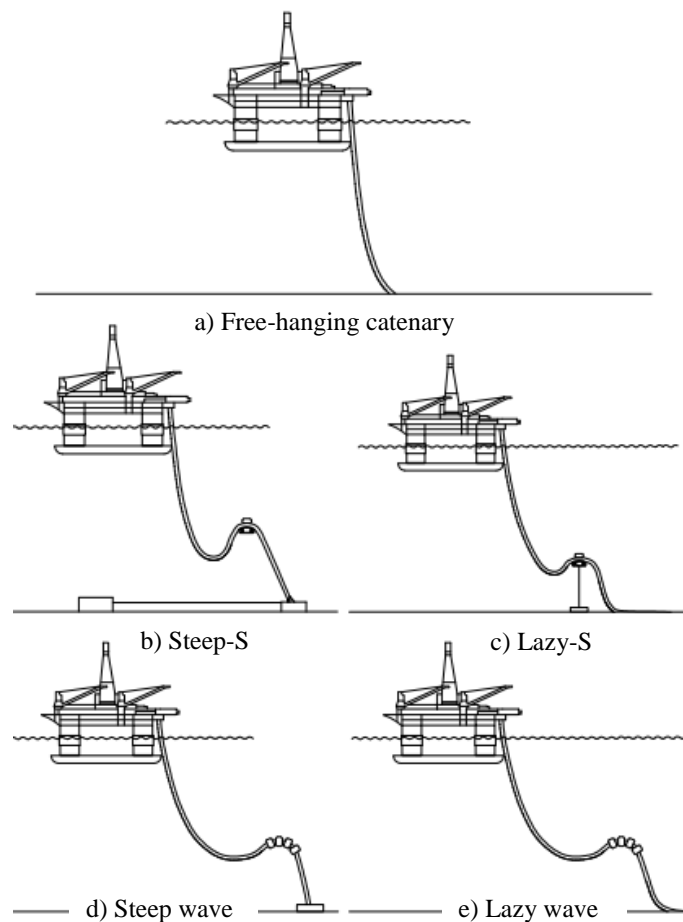
Source: (AMERICAN PETROLEUM INSTITUTE, 2008).

2.1.7. High strength steels (HSS)

Pipes designed for deeper wells often employ high strength steels (HSS), because they are cost-efficient solutions to support the mechanical loads generated by the associated high pressures and the self-weight of the structure. However, there is relatively little information on

the corrosion resistance of these kinds of steels operating under such conditions in the open literature.

2.2.   GENERAL ASPECTS OF CORROSION

Corrosion can be defined as the natural process of materials returning towards lower states of energy by the action of chemical and electrochemical reactions. The corrosion of materials occurs on the surface after the contact of a product to an aggressive environment. Corrosion should often be taken as a multidisciplinary process as several factors affect the process, such as the nature of the reactions, the corrosion mechanisms, the metallurgy, the geometry, the mechanical loads, the tides and the winds.

2.2.1.   Nature of corrosion

The nature of corrosion is defined as the combination of all relevant interactions between the environment and the materials. Accurate characterisations can be quite complex as the environment, and the surface of the material may change with time or due to an uncountable number of variables. Nonetheless, dedicating effort to identify the nature of corrosion is always advisable for corrosion assessments, since numerous steps would follow.

2.2.1.1. Aqueous corrosion

Aqueous corrosion is the degradation of materials in aqueous environments. It is quite common in nature and engineering problems, particularly to those related to the offshore oil and gas industry as a large number of structures and equipment remain underwater for long periods. Aqueous corrosion is essentially electrochemical, always involving two or more redox reactions taking place on the metal surface. The process requires the formation of a corrosion cell, which is described by four essential parts: the anode, the cathode, the electronic path and the ionic path (see Figure 11).

Figure 11: General requirements for a corrosion process.
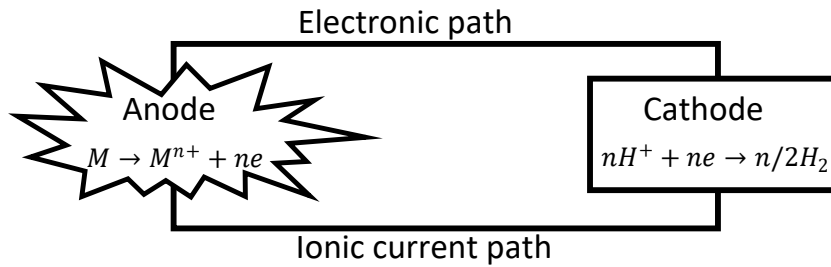
Source: Adapted from (DAVIS, 2000).

The corrosion begins when an oxidation reaction initiates at the anode, resulting in the loss of electrons and release of ions in the solution (M^{n+}), see the generalised reaction in equation 1. The electrons lost by the anode, move towards the cathode by an existing electronic path, establishing a direct current between parts. The movement of electrons is essential for the existence and continuity of the reduction reactions because the electrons lost by the anode are the ones involved in the reduction reactions at the cathode. The ionic path is also indispensable for the continuity of the process. In particular, because the dissolved ions must be somehow be transported between the anode and the cathode. Otherwise, in the absence of ions to be reduced, the degradation of the material would stop. Notice, for instance, that coating metals with paints or protective scales are effective methods to prevent corrosion because they suppress the movement of ions. Hence, it shall be stressed that all electrochemical constitutive parts must exist for the existence of an aqueous corrosion process. The suppression of one or more elements terminates the corrosion immediately (DAVIS, 2000; GENTIL, 2011).

$$M \rightarrow M^{n+} + ne \tag{1}$$

2.2.1.2. Atmospheric corrosion

Atmospheric corrosion can be defined as the chemical or electrochemical deterioration when the material remains in contact to the atmospheric air. It begins in the presence of humidity or condensed water or high temperatures. Climate factors and pollutants are also known causes capable of changing the aggressiveness of the environment (ROBERGE, 2000; SYED, 2010).

Atmospheric corrosion is classified according to the level of humidity, which is dry atmospheric corrosion, humid atmospheric corrosion or wet atmospheric corrosion. The first typically involves chemical mechanisms, characterised by slow degradation of metals in dry

atmospheres, the tarnishing of silver is a typical example. The second consists of the corrosion of metals in environments presenting relative humidity below 100%, where a thin layer of electrolyte remains in contact with the surface of the metal. In this case, the corrosion rates change according to the relative humidity and the presence of noxious species. Finally, the third type involves environments presenting condensed water in contact with the metallic surface, where the relative humidity is very close to 100%. It has been reported that the structural layers confined in the annulus of unbounded flexible pipes may experience the condensation of water; thus, atmospheric corrosion may occur in the structural layers of flexibles (ERIKSEN; ENGELBRETH, 2014; GENTIL, 2011; UNDERWOOD, 2002).

2.2.1.3. Galvanic corrosion

Galvanic corrosion is experienced after the electrical contact between two or more dissimilar metals submerged in the same solution. Accordingly, the more active metal suffers an intense attack, while the more noble metal is usually protected or has its corrosion rate greatly decreased. The galvanic coupling may induce changes in the morphology, including the growth of protective scales and build-up of passive layers. The driving force is the electrochemical potential difference between metals, forcing the electrons to flow (AMERICAN SOCIETY FOR TESTING AND MATERIALS, 2012, 2014a, 2014b; BABOIAN et al., 1976).

In general, galvanic corrosion is studied by the Mixed Potential Theory (MPT). MPT is based on the assumption that the electrochemical reactions are divided into two or more reactions (oxidation and reduction), and that there can be no net accumulation of electrical charge during the process. A general rule-of-thumb to prevent the risk of galvanic corrosion is avoiding large electrochemical potential differences between the anode and cathode. Thus, materials are often ranked into galvanic series that work as guidelines for material selections. Materials which remain close in the galvanic series shall not suffer from strong galvanic corrosion. Despite that, the galvanic series describe specific combinations of materials and environments, meaning that any variations of the electrochemical potential might affect the galvanic behaviour, for example changing the morphology of the surface or the electrolyte (AMERICAN SOCIETY FOR TESTING AND MATERIALS, 2012, 2014a, 2014b; BABOIAN et al., 1976).

2.2.2. Thermodynamics of corrosion

The concepts of thermodynamics are settled on a fundamental law of nature, in which the state of a material is always driven towards equilibrium, where the lowest state of free energy is found. Thermodynamics defines the influence of environmental aspects on the degradation of materials in equilibrium; it describes the moment when there is no measurable exchange of energy between a reactant and a product. Notice that this does not mean that the reactions would stop, rather than the rate of the reaction moving forward (R_f) would equal the rate moving backwards (R_b). Assuming the system described in equation 2, the equilibrium is mathematically characterised by the equilibrium constant, which is a function of the activities of the chemical species, equation 3. The terms "W" and "X" are the reactants; "Y" and "Z" are the products; "w", "x", "y", "z" are the stoichiometric coefficient of the main components; "a_W", "a_X", "a_Y", "a_Z" are the activities of the main species. The concepts of activities are used to describe the effective concentration of species in a mixture. In other words, whenever there is a difference between ideal and observed properties of a solution (DAVIS, 2000).

$$wW + xX \leftrightarrow yY + zZ \tag{2}$$

$$K_a = \left(\frac{a_Y^y a_Z^z}{a_W^w a_X^x} \right), \text{ when } R_f = R_b \tag{3}$$

Furthermore, thermodynamics is used to predict if a corrosive process can occur spontaneously or not. This information is revealed through the concepts of Gibbs free-energy (G). The term "G" defines the highest amount of mechanical energy that can be obtained by a substance without changing its state properties, meaning that G should be a function of state variables such as pressure (P), temperature (T) and the number of moles of given substance in a mixture (n_n), see equation 4. According to Gibbs (1873, p400), "[…] the equilibrium of the body is unstable regarding discontinuous changes, a certain amount of energy will be available under the conditions for the production of work […]".

$$G \rightarrow f(P, T, n_n) \tag{4}$$

As well as it occurs with electrical potentials, the primary importance of G does not lie on the absolute values, rather than in the variations, as ΔG reflects the chemical energy available for doing mechanical work. ΔG is mathematically determined by equation 5. The signal of ΔG

carries the information regarding the spontaneity of the reaction. If ΔG is negative, then the reaction can occur spontaneously. When ΔG is equal to zero, there is no energy available to change the state of the substance, which means that the reaction remains in equilibrium. However, if ΔG is positive, then it is possible to change the state of the substance non-spontaneously, meaning that energy should be added to the system. Figure 12 shows the free-energy diagrams for each situation. The dependence of G on the state properties, such as temperature, could explain why some materials oxidise at elevated temperatures but not at ambient conditions. In other words, this means that sources of energy like heat can enhance the chemical energy available for reactions to occur on the surface of materials (AMERICAN SOCIETY FOR METALS INTERNATIONAL, 2003; DAVIS, 2000; GENTIL, 2011).

$$\Delta G = \Delta G^0 + RT.\ln(K_a) \tag{5}$$

Figure 12: Free-energy diagrams.
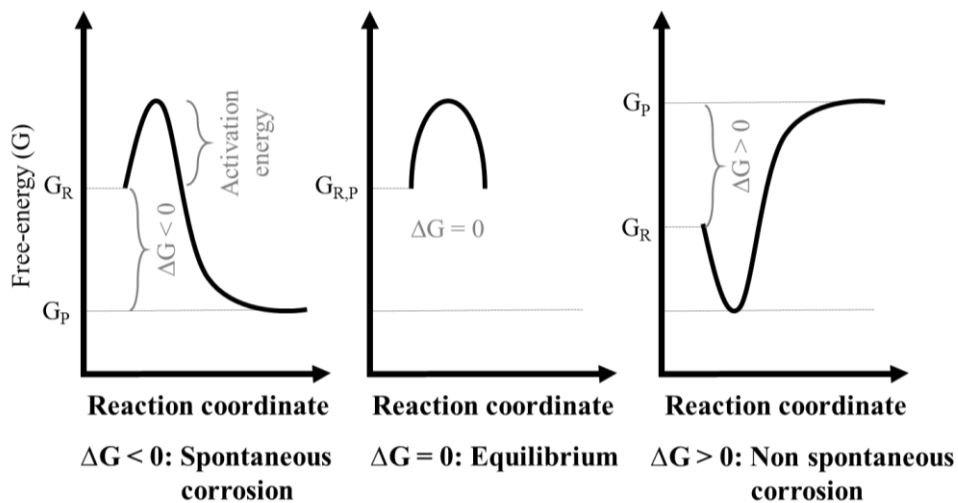
Source: Adapted from (DAVIS, 2000).

ΔG is often converted into electrical potentials to rank the oxidation or reduction tendencies of several materials in series. The conversion is achieved employing equations 6 to 8. The term "ε" is the difference in the electric potential, "ε^0" is the electric potential under the standard states, "F" is the Faraday constant (96,487 coulomb/mol), "n" is the number of electrons exchanged and "$\emptyset_i$" is the potential to move an electrical charge between two points. Such conversion is convenient to predict which direction the corrosion process could occur, once the noblest materials remain protected at the expense of the deterioration of the most active materials. Figure 13 shows an electrode potential ranking for seawater at 25 °C. The noblest

metals are found at the left side of the rank, having the higher positive electrode potentials. The most active metals are located on the right side of the list, having the most negative electrode potentials (AMERICAN SOCIETY FOR METALS INTERNATIONAL, 2003; ATLAS STEELS, 2010; DAVIS, 2000; KELLY et al., 2002).

$$\Delta G = -n.F.\mathcal{E} \tag{6}$$

$$\Delta G^0 = -n.F.\mathcal{E}^0 \tag{7}$$

$$\mathcal{E} = \emptyset_i^\alpha - \emptyset_i^\beta \tag{8}$$

Equation 9, also known as the Nernst equation for reduction half-reactions, and equation 10 describe the electrical potentials of materials regarding the activities. Notice that instead of the term "$\mathcal{E}$" is used the term "E", this happens because the electrode potentials are compared to common reference electrodes, such as standard hydrogen electrode (SHE) or standard calomel electrode (SCE).

$$E_{(ox \to red)} = E_{(ox \to red)}^0 - \frac{RT}{nF}.\ln\left(\frac{a_{red}}{a_{ox}}\right) \tag{9}$$

$$E_{(ox \to red)}^0 = \frac{RT}{nF}.\ln(K_a) \tag{10}$$

Figure 13: Electrode reduction potentials of metals (V_{SCE}), for seawater at 25 °C. The unshaded symbols show ranges exhibited by stainless steels in acidic water, which could be related to occlusion and aeration aspects.
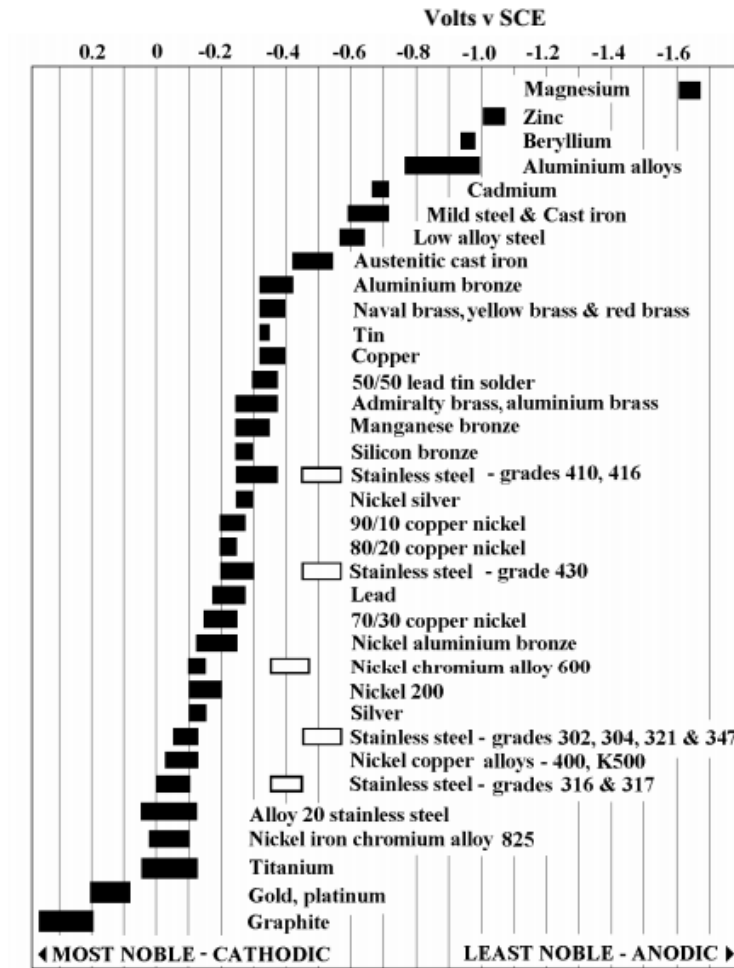
Source: (ATLAS STEELS, 2010).

2.2.3. Pourbaix diagrams

Based on the notions of chemical potential and affinity, it is possible to predict the circumstances in which electrochemical reactions are energetically possible or impossible. In other words, the equilibrium characteristics of electrochemical reactions at given environments can be represented by a point on a diagram of pH and potential (E), which derives from the Nernst equation (equation 9). The projection of the point in the diagram reveals the likely thermodynamic outcome of the contact between the material and the given environment. (AMERICAN SOCIETY FOR METALS INTERNATIONAL, 2003; AZOULAY, 2013; GHALI, 2010; POURBAIX, 1945, 1987; ROBERGE, 2000; TANUPABRUNGSUN et al., 2012; UNIVERSITY OF CAMBRIDGE, 2018).

E-pH diagrams are powerful tools for corrosion control, materials selection and for understanding the formation of scales formed by the action of nature or due to accelerated corrosion tests. Figure 14 shows an example of the equilibrium diagram of pure iron in water, taken from the original thesis of Marcel Pourbaix (POURBAIX, 1945).

Figure 14: Fe-H₂O Pourbaix diagram.
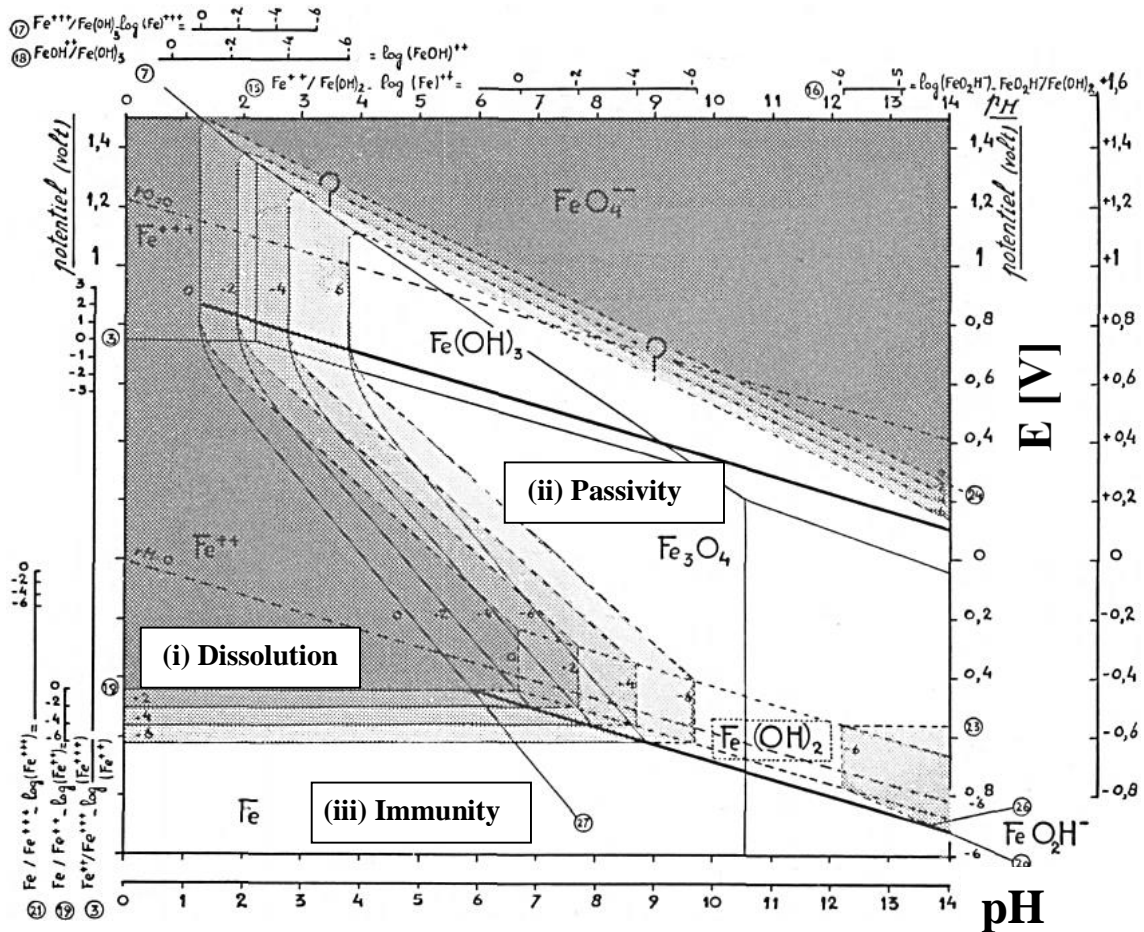
Source: Adapted from (POURBAIX, 1945).

The borderlines of the diagram represent the frontiers of stability for the electrochemical reactions. Three domains are revealed: (i) dissolution, (ii) passivity and (iii) immunity. Each domain can be associated with a particular condition of stability and corrosion surface (see Figure 15). The dissolution is related to active surfaces experiencing weight loss. Passivity is associated with surfaces containing insoluble and adherent protective corrosion products, experiencing very mild corrosion rates. Immunity is associated with the surfaces presenting thermodynamic stability on the given environment, when corrosion is unable to occur spontaneously.

Figure 15: Potential corrosion surfaces.

(i) Dissolution (ii) Passivity (iii) Immunity
Source: Adapted from (DAVIS, 2000).
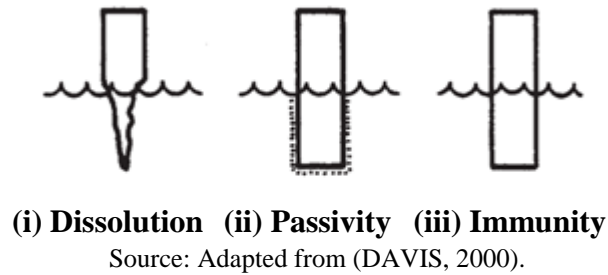
The selection of materials to sustain corrosion commonly takes into consideration the likely state in the equilibrium of the given material on the aggressive environment. For example, if carbon steel needs protection against corrosion, two possible mechanisms can be chosen by the thermodynamic principles. One is keeping the potential and pH in the immunity domain, where the material is protected. The second is inducing changes in the potential and pH in a way that a stable passive scale is formed. Therefore, one can notice the possibility of protection of the carbon steel by either a cathodic or by an anodic mechanism (AMERICAN SOCIETY FOR METALS INTERNATIONAL, 2003; AZOULAY, 2013; GHALI, 2010; POURBAIX, 1945, 1987; TANUPABRUNGSUN et al., 2012).

Despite the apparent applicability of the diagrams, the traditional E-pH plots tend to be incomplete regarding the exact representation of practical corrosion applications. Mainly, because E-pH diagrams assume pure metals submerged in solutions and because dynamic, unstable, or transitional states are not comprised in the calculations. One can notice that a substantial portion of the engineering corrosion problems is related to alloys in transient states or in the presence of fluids containing many chemical species. Therefore, it is essential to understand that the cases where the Pourbaix diagrams can be used in full could be limited (GHALI, 2010).

2.2.4. Kinetics of corrosion

Kinetics is the field of corrosion focused on the corrosion rates (CR). It is applied to a number of occasions, including corrosion control, life assessments, understanding the corrosion mechanisms, materials selection, quality control, verification and validation of new materials and alloys. It shall be stressed that the scope of kinetics is outside of the domain of thermodynamics (AMERICAN SOCIETY FOR METALS INTERNATIONAL, 2003).

The rate at which a material deteriorates in a given environment can be expressed by many units, such as the penetration rate, the rate of weight loss or the current density. Various methods can be used to measure corrosion rates, including weighing coupons with known weight after submersion in aggressive fluids, for determining the average corrosion rates. Other, and more complex electrochemical techniques, such as linear sweep voltammetry (LSV), cyclic voltammetry (CV) and linear polarisation resistance (LPR) may also be employed with the advantage of describing corrosion properties, such as: corrosion potentials, polarisation resistance, resistance of the electrolyte and Tafel slopes (AMERICAN SOCIETY FOR TESTING AND MATERIALS, 1989, 1997, 2003, 2014c; RIBEIRO, 2014).

Electrochemical methods are commonly preferred for laboratory testing because of the high degree of specificity offered in relatively short periods. These techniques usually describe the corrosion rates by sweeping or disturbing the electric potential (or current) of the material of interest, also known as the working electrode (WE). The underlying assumption behind electrochemical testing is that the corrosion rate of a material is proportional to the electric current passing through the components of the system. The combination of the generalised oxidation reaction (equation 1), equation 6 and the Arrhenius expression (equation 11) results in equation 12, which reveals the exponential relationship between electric current with the overpotential (η). The term "k" is the rate of the reaction and "C" is a constant. The term "η_a" defines the difference between artificially driven potential (anodic) and equilibrium potential. "I_a" is the term used for anodic current, "I_0" for the current flowing in both directions when an electrode reaction is at equilibrium and "α" is a symmetry factor. The step-by-step description to obtain equation 12 can be found in the literature (AMERICAN SOCIETY FOR METALS INTERNATIONAL, 2003; UNIVERSITY OF CAMBRIDGE, 2018).

$$M \rightarrow M^{n+} + ne \tag{1}$$

$$\Delta G = -n.F.\varepsilon \tag{6}$$

$$k = C\, e^{\left[-\Delta G/RT\right]} \tag{11}$$

$$I_a = I_0\, e^{\left[\alpha nF\eta_a/RT\right]} \tag{12}$$

Equation 12 is also known as one form of the Tafel equation, which can be adjusted to obtain equation 13. Accordingly, "b_a" is the Tafel slope, and "C_a" a constant. Moreover, because the reactions are essentially electrochemical rather than chemical, the anodic and cathodic currents can be studied independently and should share equal magnitudes. Therefore, a similar

approach can be followed for the cathodic reactions, which results in equation 14. In this case, "b_c" is the cathodic Tafel slope and "C_c" a cathodic constant.

$$\eta_a = C_a + b_a \log_{10} i_a \tag{13}$$
$$\eta_c = C_c + b_c \log_{10} i_c \tag{14}$$

The Tafel slopes are defined as measures of energy barrier symmetry of the potential energy curves. They can be calculated by equation 15 when all of the reactions involved in the corrosion process are known in depth. Otherwise, the Tafel slopes are estimated from the slopes at the linear portions of semi-log plots i x E, as shown in Figure 16 (AMERICAN SOCIETY FOR TESTING AND MATERIALS, 1989, 1997, 2014c; ROBERGE, 2000).

$$b_{a,c} = {2.303.RT}/{\alpha nF} \tag{15}$$

Figure 16: Hypothetical scheme of a polarisation diagram.
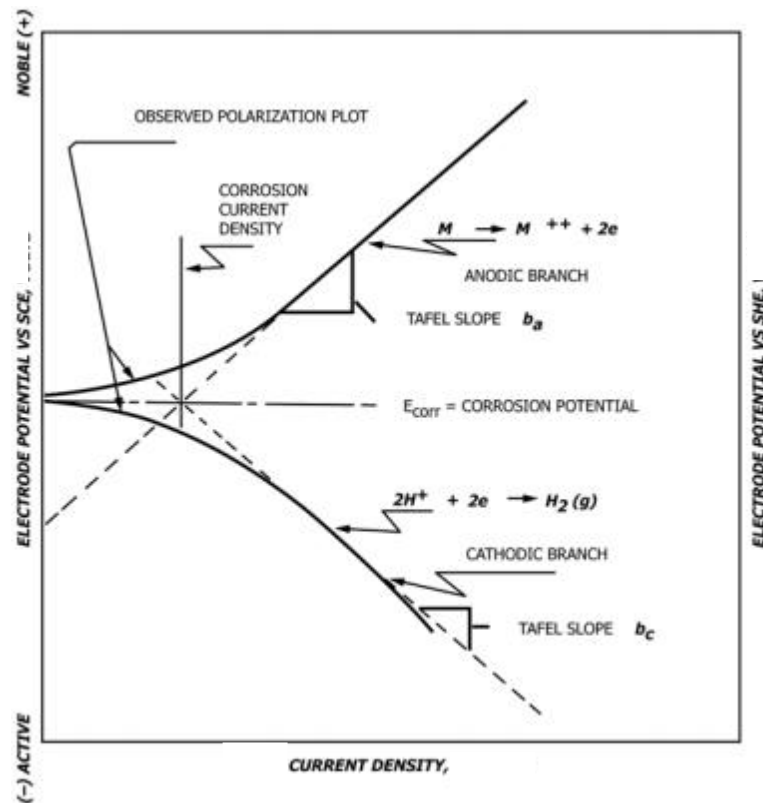
Source: (AMERICAN SOCIETY FOR TESTING AND MATERIALS, 2014c).

2.2.5.   Electrochemical corrosion mechanisms

The corrosion phenomena of metals involve a great variety of mechanisms that are grouped according to the nature of the corrosion. This work focusses on the electrochemical degradation of metals in aqueous environments. Under such circumstances, the corrosion of metals often occurs by charge-transfer or diffusion controlled or even mixed-mechanisms. Each one presents its specific behaviour regarding the corrosion rates. For example, the charge-transfer mechanism, also known as activation-control, can be identified by the linear behaviours on semi-log plots of current density (i) versus potential (E). The second mechanism, called diffusion controlled, refers to the corrosion process where the concentration of a particular chemical cannot be sustained at the same level as that in the bulk of the solution, so the process becomes controlled exclusively by the transport of chemical species from the bulk solution to the metal-electrolyte interface. This way, any factor changing the diffusive or advective properties, such as fluid velocity, shall disturb the corrosion rates. These mechanisms are visualised in Figure 17, where linear voltammetry sweeps were performed in rotating electrodes. The overlapping straight lines, seen in the anodic branches, reveal the charge-controlled mechanism, once the diffusive and advective factors show no impact on the current density. The portion of the plot with non-overlapping corrosion densities, seen in the cathodic branches, reveals the mass-controlled mechanism, where the relative velocities between the working electrodes and electrolyte change the supply of reactants available for the redox reactions, thus impacting on the current density (HERNANDEZ; MUÑOZ; GENESCA, 2012).

Figure 17: Polarisation curves of steel at different rotation rates. A test carried in brine solution saturated with carbon dioxide at 20 °C.
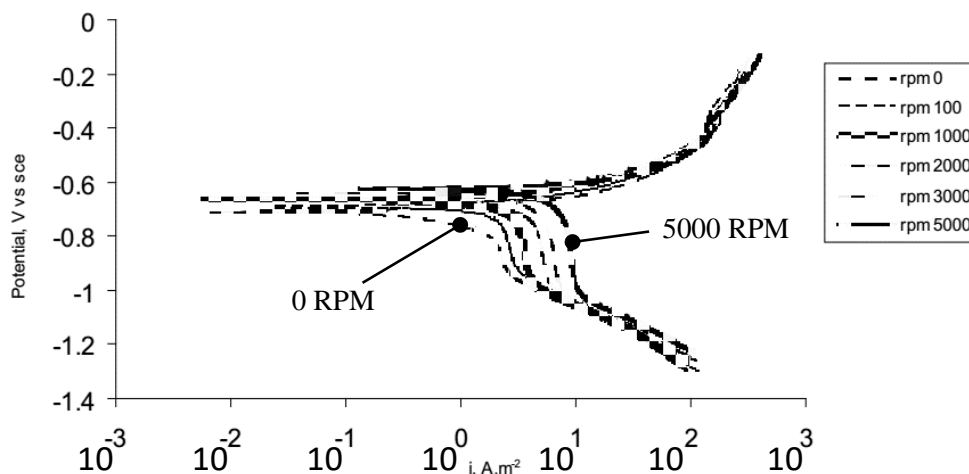
Source: Adapted from (HERNANDEZ; MUÑOZ; GENESCA, 2012).

2.3.   ANNULUS ENVIRONMENT

The annulus was initially designed to operate under dry conditions. However, reality shows that it evolves into very complex environment, whose severity hinge on numerous factors, such as the atmospheric variables, the composition of the solution, the operating conditions, the geometric factors and the integrity of the outer sheath. And, many of these vary along the pipe length and depth.

The large gradients of pressure and temperature in which the wires are located widen the complexity of the discussion, given their effects on kinetics and chemistry of the environment and materials. According to modern knowledge, the temperatures in the annulus should range between 20 and 80 °C, where the variations are a function of the temperature difference between the fluid running in the bore and the seawater surrounding the pipe. Pressure is essentially depth dependent; thus, segments of the pipelines operating at deeper wells may experience more severe hydrostatic pressures. Hence, the following chapters shed light on crucial issues regarding the flooding and permeation of fluids towards the annulus, the interactions between liquid and gaseous phase interactions, and the specific hydrochemistry of carbon dioxide (CHEMISTRY BLOG, 2018; CLEMENTS, 2008; CLEMENTS; ETHRIDGE, 2003; DÉSAMAIS; TARAVEL-CONDAT, 2009; DUGSTAD et al., 2015; FERGESTAD; LØTVEIT, 2014; KE et al., 2017; NEŠIĆ, 2007; NOV, 2015; ROGOWSKA et al., 2016; ROPITAL et al., 2000; RUBIN et al., 2012; UNDERWOOD, 2002).

2.3.1.   Breaches of the outer polymer sheath

The outer polymer sheath is a constitutive layer of the unbounded flexible pipe designed to prevent direct contact between seawater and the structural wires. The failure of this layer is one of the leading threats to unbounded flexible pipes, because it enables conditions for considerable corrosion on the structural layers of the pipe. Breaches can be associated with many causative factors, including blockage of the venting system, impact damage, abrasion, non-conformities during installation and operation. According to 4SUBSEA (2013), avoiding damages to the outer sheath could mitigate the corrosion process of the structural layers of the pipe. However, it seems very unlikely that industry will manage to eradicate them in the short-term. Keeping that in mind, the understanding of the corrosion mechanisms and variables affecting the environment are essential to improve prediction and capabilities of the technology

(4SUBSEA, 2013; ERIKSEN; ENGELBRETH, 2014; FERGESTAD; LØTVEIT, 2014; JOEL, 2009).

2.3.2. Permeation of fluids into the annulus

Although the internal and outer polymer sheaths of the annulus are designed to prevent the direct contact to the internal fluid and surrounding seawater, modern flexible pipes remain susceptible to ingress of water and gases through permeation processes into the annulus. The polymer layers exhibit a certain level of permeability towards water, carbon dioxide, methane and hydrogen sulphide (see Figure 18). The fluid permeation can be unidirectional or bidirectional, i.e. between the bore and the annulus or between the annulus and the seawater in the surroundings (BORGES, 2017).

Figure 18: Schematic illustration of the permeation of gases from the bore into the annulus region.
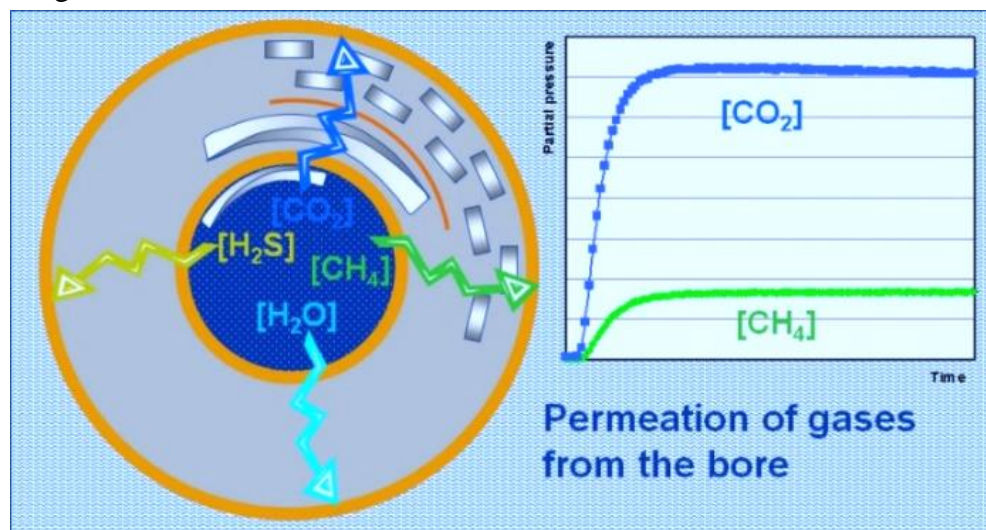
Source: AUTHOR.

The understanding of the transport mechanisms of the fluids into the annulus and the consequent damage to the structural layers of the pipe is still very far from satisfactory, as thermodynamic and kinetic aspects are yet poorly understood. For example, the permeation rate is usually interpreted as a kinetic variable; however, studies exploring the effect of low flow rates on the risk of sulphide stress corrosion cracking in H_2S-containing environments identified that the restricted permeation rates could influence the steady state concentration of this aggressive species in the simulated annulus conditions. These studies point out that the permeation rates tend to be low compared to consumption by the corrosion of the large surface

of steel confined in the annulus (DÉSAMAIS; TARAVEL-CONDAT, 2009; HAAHR et al., 2016). Other types of uncertainties lie on the fact that the annulus presents open spaces in a non-uniform fashion respective to the specific layered geometry of the pipe and non-uniform presence of fluids. As a result, the transport of species by permeation mechanisms can be difficult to predict.

Nonetheless, despite a large number of unanswered questions, the academic community dedicates massive efforts to overcome uncertainties. In particular, of the factors ruling the transport properties and mechanisms through polymer membranes at harsh environments (DE ALMEIDA, 2012; LIN; FREEMAN, 2004; NAITO et al., 1993; PATIL et al., 2006). Klopffer and Flaconneche (2001) divide the transport mechanism of a homogeneous non-porous polymer membrane at a given temperature in five stages. The stages are given in Figure 19 and described as follows: i) diffusion through the limit layer at the upstream side; ii) absorption of the gas by the polymer; iii) diffusion of the gas inside the polymer membrane; iv) desorption of the gas at the lower partial pressure side; v) diffusion through the limit layer at the downstream side.

Figure 19: Five stages of the transport mechanism of a homogeneous non-porous polymer membrane at a given temperature.
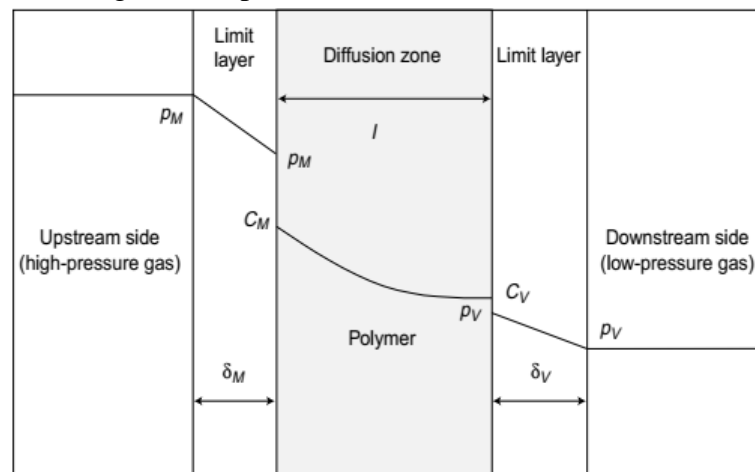
Source: (KLOPFFER; FLACONNECHE, 2001).

MOLDI™ is a model presented in the works of Benjelloun-Dabaghi et al. (2002) and of Taravel-Condat; Guichard; Martin (2003). It was designed to predict the diffusion of gases through layers of flexible pipe versus time. Fick and Henry's laws are used in the calculus of the concentrations and pressure versus time. The authors concluded that reasonable predictions of flow rate and pressure build-up are achieved for pressures of the annulus below 50 atmospheres.

2.3.3. Henry's law of solubility

The earliest studies on the solubility of carbon dioxide in water date from the beginning of the 19 century, where the work of William Henry (1803) constitutes the building block for the law of solubility, also known as Henry's law of solubility (equation 16). According to Henry (1803), the amount of dissolved gas is proportional to its partial pressure of a chemical specie (pP) and to an equilibrium constant (K_H), which is named as Henry's constant. More precisely, the effect of pressure on the solubility is given along these lines:

> […] that, under equal circumstances of temperature, water takes up, in all cases, the same volume of condensed gas as of gas under ordinary pressure. But, as the spaces occupied by every gas are inversely as the compressing force, it follows, that water takes up, of gas additional atmospheres, a quantity which, ordinarily compressed, would be equal to twice, thrice, etc. the volume absorbed under the common pressure of the atmosphere.[…] (HENRY, 1803, p.41).

$$\text{Solubility } = K'_H \cdot pP \qquad\qquad (16)$$

Henry (1803) also observed that the quantity of carbon dioxide dissolved in the solution tends to decrease with the increase of temperature. Such tendency is related to the effect of temperature on the equilibrium constant K_H. Methods to obtain accurate values of K_H are outside the scope of this work but can be obtained in the literature as a function of temperature (van 't Hoff equation) or the Gibbs free-energy (MAJER; SEDLBAUER; BERGIN, 2008; SANDER, 2015).

Though modern knowledge agrees with Henry's law of solubility at low to moderate pressures, the relationship proposed by Henry is constrained by simplifications. For example, Henry's constant neglects the effect of pressure and assume that activity equals the concentration. Therefore, although Henry's law was developed to describe the effect of temperature and gas pressure on the solubility of the gaseous species in water, his work is restricted to circumstances where liquid phase non-idealities can be neglected. Outside this domain, modern studies usually focus on the description of systems by means of modelling and correlations from empirical data.

Figure 20 and Figure 21 show, respectively, the effects of temperature and pressure in the solubility of CO_2 in water (AQION, 2018; CARROLL; SLUPSKY; MATHER, 1991; HANGX, 2005; OLI STUDIO, 2016).

Figure 20: Effect of temperature on the solubility of carbon dioxide in water.
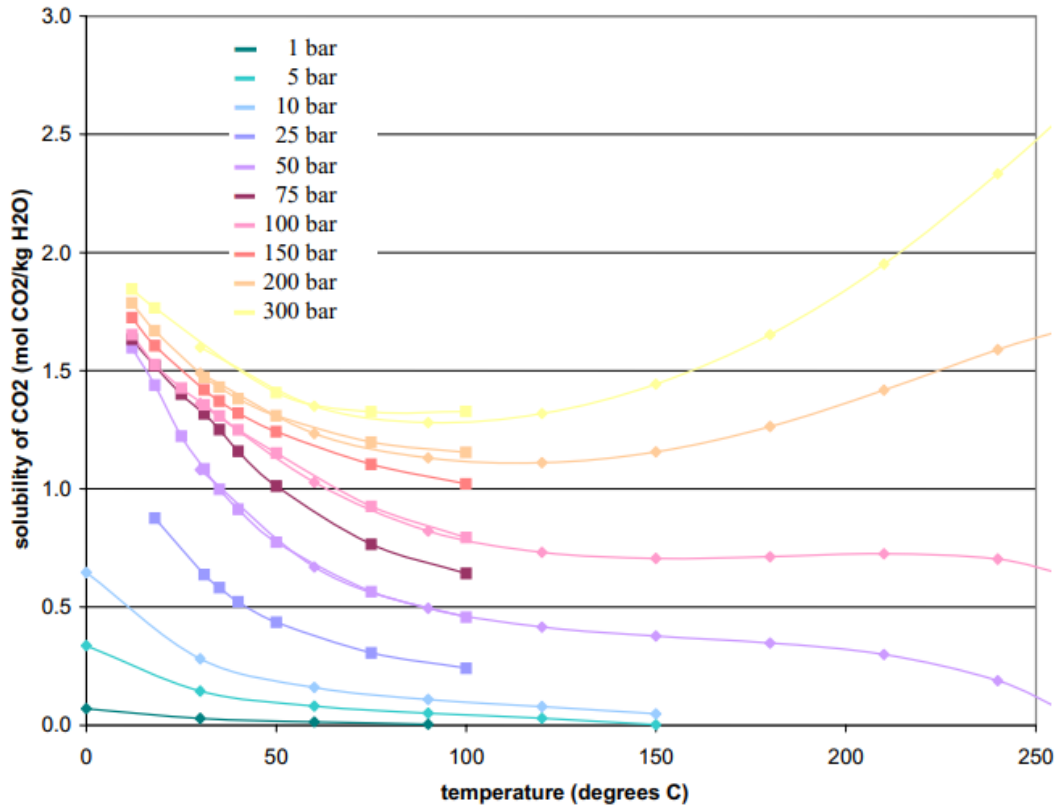
Source: (HANGX, 2005).

Figure 21: Effect of pressure on the solubility of carbon dioxide in water.
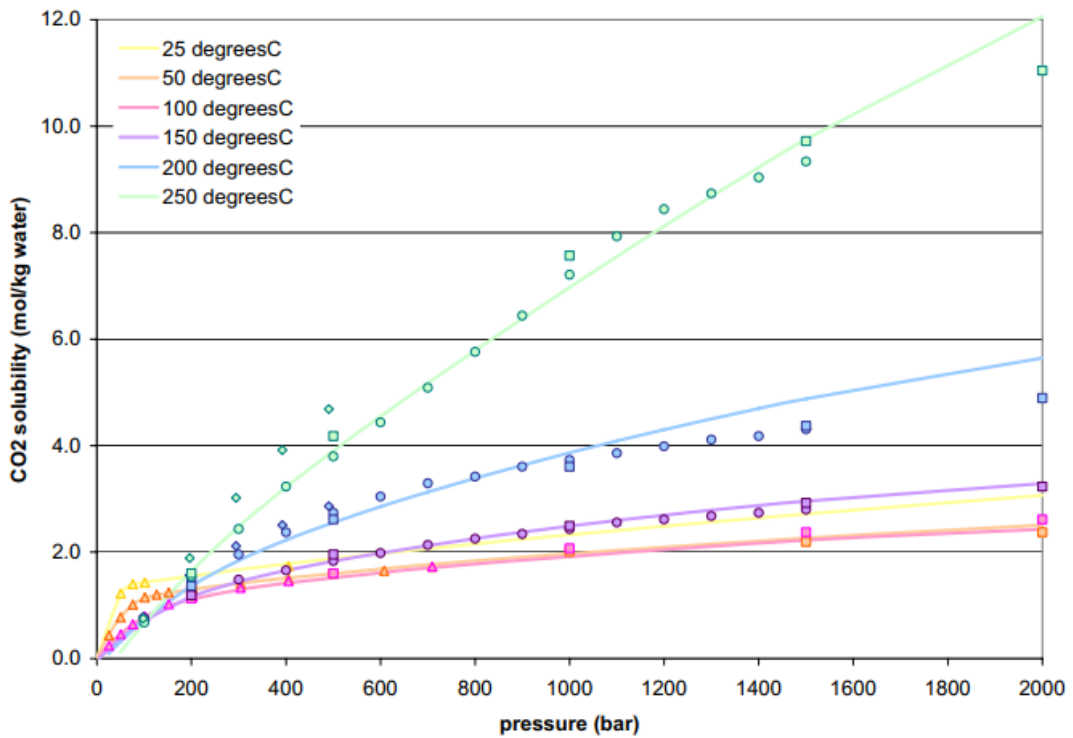
Source: (HANGX, 2005).

2.3.4. H₂O/CO₂ systems

Carbon dioxide is a linear and non-polar chemical compound consisting of one atom of carbon and two atoms of oxygen. The intermolecular forces of attraction are weak; thus, carbon dioxide is gaseous under normal atmospheric conditions. Figure 22 shows the phase stability diagram including solid, liquid, gaseous and supercritical states of the carbon dioxide.

Figure 22: Phase diagram for carbon dioxide.
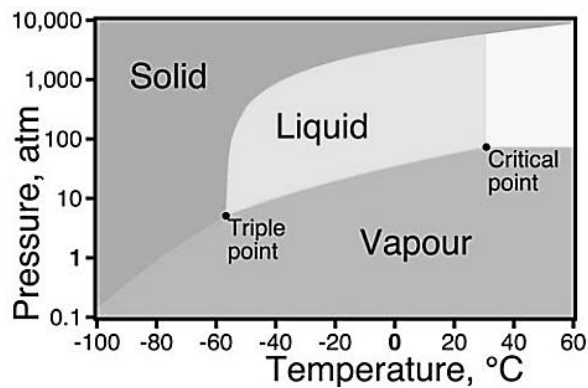
Source: (CHEMISTRY BLOG, 2018).

The term "system", broadly considered in this work, characterises the electrolyte of interest and all relevant interactions. More precisely, the system consists of the fluid confined in the annulus, mainly composed of salt water and carbon dioxide. Everything external to the system is called "neighbourhood". All interactions between the system and neighbourhood are defined by the boundary conditions, also known as boundaries of the system. These boundaries act as the backbone of the study, connecting the theory to the reality experienced by the component (MORAN; SHAPIRO, 2002). Table 2 shows the possible thermodynamic systems and boundaries conditions available for the study of CO_2 annulus corrosion, where the main difference lies in the interactions of matter and energy with the surrounding neighbourhood.

Table 2: Systems and boundary conditions.

Thermodynamic system	Exchange of Energy	Exchange of Matter
Open system H_2O/CO_2	Yes	Yes
Closed system H_2O/CO_2	Yes	No
Isolated system	No	No

Source: Adapted from (AQION, 2018).

The open system H_2O/CO_2 allows the exchange of energy and matter, meaning that the natural processes of materials returning towards lower states of energy are free to exist. Also, this system is not bound by finite amounts of matter, so the sum of all chemical species may not be constant. On the other hand, closed system H_2O/CO_2 is characterised by containing finite and well-defined amounts of matter in the system, as the exchange of mass with the neighbourhood is forbidden. In practice, this means that the growth of the concentration of one species is limited to the total concentration of anothers because the mass balance must remain constant. Isolated systems are not explored here because they seem unrealistic for the purpose of this work, given their complete isolation from the neighbourhood regarding energy and matter.

2.3.5. Hydrochemistry

Hydrochemistry is the branch of science that studies the chemical composition of natural waters and the laws governing its changes. Understanding the particular hydrochemistry of water/carbon dioxide systems is essential to obtain indications of the aggressiveness and permeation properties of the environment, since CO_2-corrosion is a synergic process involving chemical, electrochemical and mass transport reactions (BARKER et al., 2018; CARROLL; SLUPSKY; MATHER, 1991; DE ALMEIDA, 2012; DÉSAMAIS; TARAVEL-CONDAT, 2009; HAAHR et al., 2016; NEŠIĆ, 2007; SANTOS et al., 2013; TARAVEL-CONDAT; GUICHARD; MARTIN, 2003).

In open systems composed of water and carbon dioxide, the interactions begin with the hydration of carbon dioxide (equation 17), followed by the formation of carbonic acid (equation 18). At this point, the carbonic acid dissociates twice (equation 19 and equation 20), releasing hydrogen (H^+), bicarbonate (HCO_3^-) and carbonate (CO_3^{-2}) in the water. The self-ionization of water (equation 21) also takes place in the full description of the chemical reactions.

$$CO_{2(g)} \Leftrightarrow CO_{2(aq)} \tag{17}$$

$$CO_{2(aq)} + H_2O \overset{KH}{\Leftrightarrow} H_2CO_3 \tag{18}$$

$$H_2CO_{3(aq)} \overset{K1}{\Leftrightarrow} H^+ + HCO_3^- \tag{19}$$

$$HCO_3^- \overset{K2}{\Leftrightarrow} H^+ + CO_3^{2-} \tag{20}$$

$$H_2O \overset{Kw}{\Leftrightarrow} H^+ + OH^- \tag{21}$$

The full characterisation of open H_2O/CO_2-systems requires the quantification of 6 chemical species ($CO_{2(aq)}$, H_2CO_3, HCO_3^-, CO_3^{-2}, H^+ and OH^-) and four equilibrium constants (K_H, K_1, K_2, K_w), totalling ten variables. However, all equilibrium constants can be obtained from specific pressure-temperature tables available in the literature (MAJER; SEDLBAUER; BERGIN, 2008; SANDER, 2015). With this simplification, the required number of equations would drop to six. The remaining equations needed, can be obtained by employing the mass-action law and performing mass and charge balances. In which, assuming ideally diluted solutions the system is specified from equation 22 to 27. Note that the carbonate ion in equation 27 is multiplied by a factor of 2 because of the divalent charge (AQION, 2018; MOHAMED et al., 2011; OLI STUDIO, 2016).

Mass-action law: $\qquad K_H = [H_2CO_3]/pCO_2$ $\qquad\qquad\qquad\qquad$ (22)

Mass-action law: $\qquad K_1 = [H^+][HCO_3^-]/[H_2CO_3]$ $\qquad\qquad$ (23)

Mass-action law: $\qquad K_2 = [H^+][CO_3^{-2}]/[HCO_3^-]$ $\qquad\qquad$ (24)

Mass-action law: $\qquad K_w = [H^+][OH^-]$ $\qquad\qquad\qquad\qquad$ (25)

Mass balance: $\qquad\quad DIC = [H_2CO_3] + [HCO_3^-] + [CO_3^{2-}]$ $\qquad$ (26)

Charge balance: $\qquad [H^+] = [HCO_3^-] + 2[CO_3^{2-}] + [OH^-]$ $\qquad$ (27)

The same set of equations is also used for the characterisation of closed H_2O/CO_2-systems. However, closed systems present the additional limitation of finite amounts of matter, which is represented by the constant value of dissolved inorganic carbon (DIC). As a result, the formation of carbonic acid is not only a function of equation 22 but also restricted by the total DIC available in the system. Although the differences between open and closed carbonate systems are well understood, this subject is poorly addressed in the literature. Hence, such differences are contained within the scope of this work, meaning that further details are provided in the section of results and discussion.

2.4. CORROSION OF UNBOUNDED FLEXIBLE PIPES

Figure 23 shows a list of some variables that may affect the corrosion of unbounded flexible pipes. It is assumed that the process is complex and multidisciplinary, involving the hydrochemistry of seawater, operating conditions, aspects of design and assembly of the pipes

and corrosion mechanisms. Also, despite the focus on occluded CO_2-corrosion of flexible pipes dedicated to this work, the literature review also includes the effect of depth and bulk corrosion given the possibility of the structural layers of the pipe remain directly in contact to seawater as a result of unrepaired damages in the outer layer of the flexibles.

Figure 23: Examples of variables that can affect the corrosion process of unbounded flexible pipes.

Source: AUTHOR.

2.4.1. Effect of depth on the corrosion of subsea structures

Though the water surrounding the pipe should not be in direct contact to the structural layers of the flexible pipes under normal conditions, ruptures and failures of the outer sheath are common, exposing the structural layers of the pipe to corrosion. It is known that many variables are a function of depth, including the hydrostatic pressure, the temperature and the chemical composition of seawater. Recognising this information is essential to understand the effects of depth on the corrosion of subsea structures.

A study of a steel piling submersed in seawater, described in Davis (2000), is used as basis to demonstrate the effect of depth. It is reasonable to assume that unrepaired damages to the structural layers of unbounded flexible pipes may undergo comparable trends of corrosion

rates. Accordingly, Figure 24 shows a sketch of the corrosion rates obtained from the steel piling, where a total of five zones are revealed.

Figure 24: Corrosion rate of a steel piling in seawater.
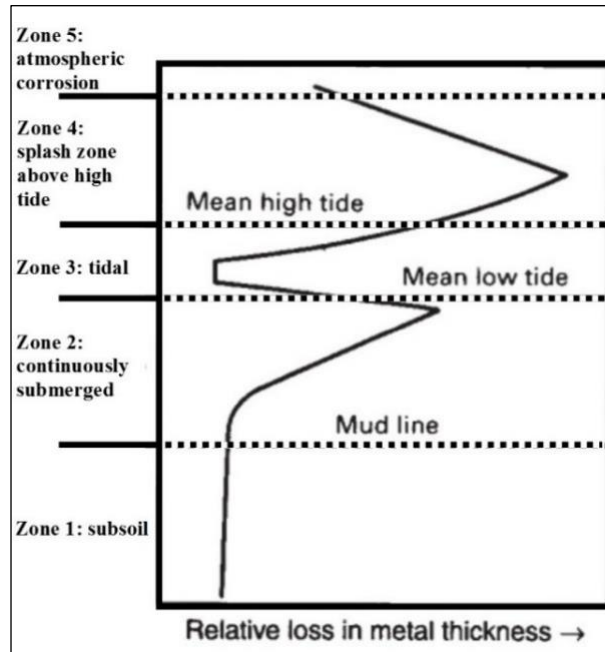
Source: Adapted from (DAVIS, 2000).

The discussion begins at the deepest portion of the structure, zone 1, where the steel lies submerged in the ocean mud. The mud often contains large quantities of organic material in decomposition that produces a reductive atmosphere, containing low concentrations of oxygen. This scenario implies in a reduction on the corrosion rates by constraining the cathodic reactions (DAVIS, 2000). Equation 28 and equation 29 show typical examples of cathodic reactions for aerated and de-aerated water respectively (GENTIL, 2011).

Aerated water: $\quad\quad H_2O_{(l)} + 1/2O_{2(g)} + 2e \rightarrow 2OH^-_{(aq)}$ $\quad\quad\quad$ (28)

De-aerated water: $\quad H^+ + e^- \leftrightarrow {}^1/_2\, H_{2(g)}$ $\quad\quad\quad\quad\quad\quad$ (29)
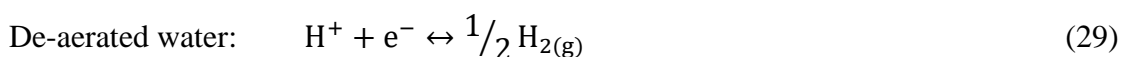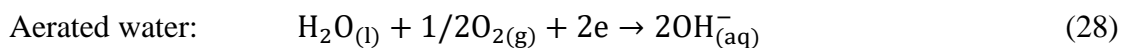
Zone two describes the portion where the metal is continuously submerged in the saline aqueous environment. Throughout this section, the salinity of the water can be considered approximately constant, around 35,000 ppm. However, as observed in Figure 25, the amount of dissolved oxygen decreases with depth. Consequently, the corrosion rates also decrease with depth due to the reduction of the concentration of oxygen (DAVIS, 2000; SCRIPPS INSTITUTION OF OCEANOGRAPHY, 2013). Figure 26 shows the effect of a rupture of the

outer sheath that took place on an unbounded flexible riser operating in 630 metres below sea level, in a position that could be compared to a deep portion of zone two. According to de Negreiro (2016), the flooding of the annulus have led to:

i) Partial corrosion on the inner and outer surface of the wires, with mild loss of thickness;

ii) Similar deteriorations of the first and second layer of tensile wires;

iii) Localised corrosion;

iv) Stronger corrosion near the gaps between the steel and anti-wear tapes;

v) The corrosion found near the breach of the outer layer was visually more intense than a zone 5 metre distant.

Figure 25: Annual average of the dissolved oxygen per depth. a) 0 metres. b) 1000 metres. c) 2000 metres.
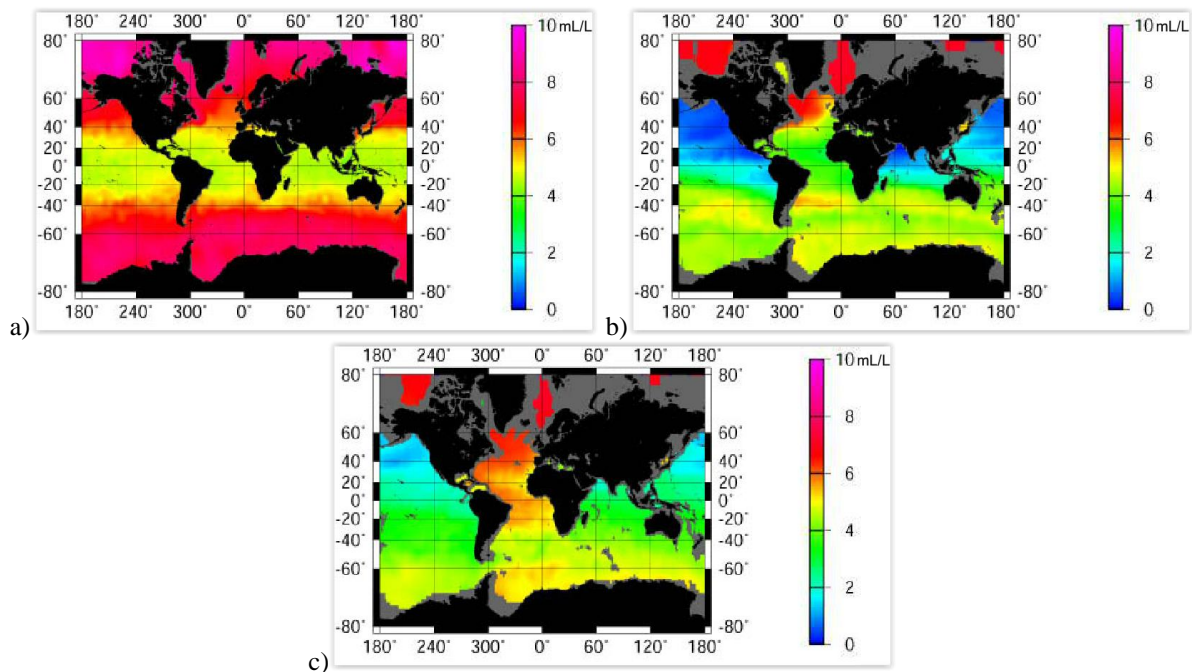
Source: (SCRIPPS INSTITUTION OF OCEANOGRAPHY, 2013).

Figure 26: Images of the inner tensile layer of an unbonded flexible pipe. a) Shows the corroded wires without the presence of the anti-wear tape and b) shows the anti-wear tape.
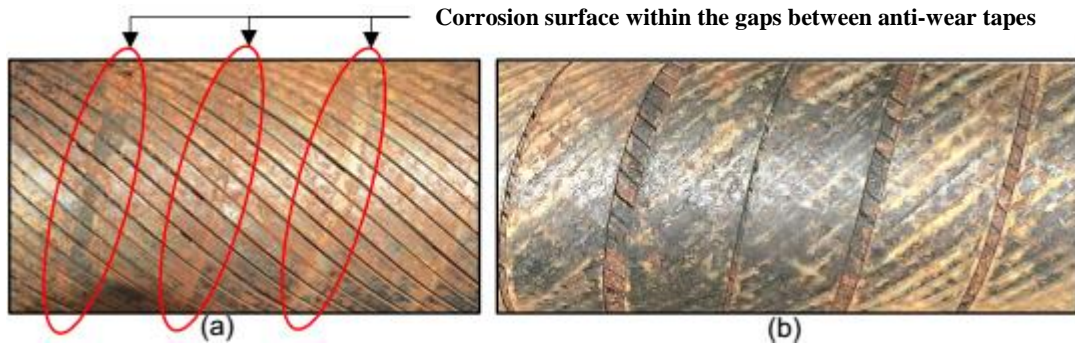
Source: (DE NEGREIROS, 2016).

Zone three refers to the portion affected by the tides zone. This zone is favourable to the biological species that may protect the steel against the seawater, so the corrosion rates tend to reduce. As the depth decrease, a section of the pilling remains alternately submerged in seawater. Consequently, corrosion rates tend to increase again because of the availability of oxygen (DAVIS, 2000).

Zone four refers to the splash zone. This section presented the higher corrosion rates found in the steel pilling because of the increased local salinity and high availability of oxygen. The splashing of water leaves droplets, rich in chloride, on the surface of the steel. After evaporation, the local salinity of the surface can increase considerably (DAVIS, 2000).

Zone five describes the portion of the pilling damaged by the atmospheric corrosion. Since aqueous corrosion is generally more aggressive than atmospheric corrosion, the corrosion rates tend to decrease gradually as the incidence of droplets in the structure decrease (DAVIS, 2000).

2.4.2. Bulk CO_2-corrosion

Bulk CO_2-corrosion is defined as the corrosive process occurring in environments rich in carbon dioxide, in the presence of considerable volumes of water. A peculiarity of CO_2-corrosion is that a substantial number of parameters may significantly influence it, and the interactions between variables can be reasonably complex. Therefore, despite a large number of works available in the literature, the phenomenon is still poorly understood. Hence, the following chapters provide brief introductions to some subjects deemed pertinent to this work (CROLET; THEVENOT; NEŠIĆ, 1998; DUGSTAD et al., 2015, 2018; FANG; BROWN; NEŠIĆ, 2013; HAN et al., 2007; LIU et al., 2016; LOPEZ et al., 2003; LÓPEZ; PÉREZ;

SIMISON, 2003; NEŠIĆ, 2007; SCHMITT; HÖRSTEMEIER, 2006; SUHOR et al., 2012; SUN, 2006; SUN; NEŠIĆ, 2008; TANUPABRUNGSUN et al., 2012; ZENG; LILLARD; CONG, 2016).

2.4.2.1. Mechanisms of CO$_2$-corrosion

Two possible charge-transfer mechanisms can be linked to the cathodic reactions. One is the direct reduction mechanism that is attributed to the reduction of the adsorbed carbonic acid molecule occurring at the metal surface, described from equation 29 to 32. The other potential mechanism is the so-called "buffering effect", in what the dominant cathodic reaction is the reduction of hydrogen ions, whereas the dissociation of the carbonic acid provides additional hydrogen ions. The buffer effect offers an alternative pathway to the reduction of carbonic acid (equation 31), given by the combination of the dissociation reaction (equation 19) and the reduction of hydrogen (equation 29) (ALMEIDA et al., 2017; HERNANDEZ; MUÑOZ; GENESCA, 2012; KAHYARIAN; BROWN; NEŠIĆ, 2018; NEŠIĆ, 2007; THU; BROWN; NEŠIĆ, 2015).

A) Direct carbonic acid reduction mechanism:

$$H^+ + e^- \leftrightarrow {}^1\!/_2\, H_{2(g)} \tag{29}$$

$$H_2O_{(l)} + e^- \leftrightarrow OH^-_{(aq)} + {}^1\!/_2\, H_{2(g)} \tag{30}$$

$$H_2CO_{3(aq)} + e^- \leftrightarrow HCO^-_{3(aq)} + {}^1\!/_2\, H_{2(g)} \tag{31}$$

$$HCO_{3(aq)} + e^- \leftrightarrow CO^-_{3(aq)} + {}^1\!/_2\, H_{2(g)} \tag{32}$$

B) Buffering effect:

$$H_2CO_{3(aq)} \leftrightarrow H^+ + HCO_3^- \tag{19}$$

$$H^+ + e^- \leftrightarrow {}^1\!/_2\, H_{2(g)} \tag{29}$$

$$H_2CO_{3(aq)} + e^- \leftrightarrow HCO^-_{3(aq)} + {}^1\!/_2\, H_{2(g)} \tag{31}$$

Recent bulk CO$_2$-corrosion studies performed with controlled pH express the dominance of the buffering effect (KAHYARIAN; BROWN; NEŠIĆ, 2018; THU; BROWN; NEŠIĆ, 2015). However, despite the many years of research, the exact cathodic mechanisms are still being debated. For instance, Hernandez; Muñoz; Genesca (2012) used a rotating

electrode setup to perform electrochemical measurements in the API 5L X70 steel rods submerged in 3% NaCl solution saturated with oxygen-free CO_2 gas, at the pH of saturation of pH3.9, and temperature of 20 °C. The authors observed the presence of a diffusion-controlled process. Nevertheless, there seems to be a consensus in the literature that the carbon dioxide enhances the cathodic reaction, intensifying the corrosion rates (ALMEIDA et al., 2017; HERNANDEZ; MUÑOZ; GENESCA, 2012; NEŠIĆ, 2007; THU; BROWN; NEŠIĆ, 2015).

Concerning the anodic reaction, the dissolution of iron is understood as a multi-step mechanism, dependent on the electrode potential and pH (EL MILIGY; GEANA; LORENZ, 1975; THU; BROWN; NEŠIĆ, 2015). According to El Miligy; Geana; Lorenz (1975), the iron oxidation is subjected to four mechanisms associated with different corrosion behaviours after conducting potential sweeps in oxygen-free weak acid aqueous solutions (see Figure 27). The transition and pre-passivation peak potentials were shown to be pH dependent. The apparent Tafel slopes characterise each electrochemical behaviour.

Figure 27: Anodic polarisation curve of iron with the scan rate of 6.6 mV/s and rotating disk electrode at 69 rps in 0.5 M Na_2SO_4 solution at pH5 and 25 °C.
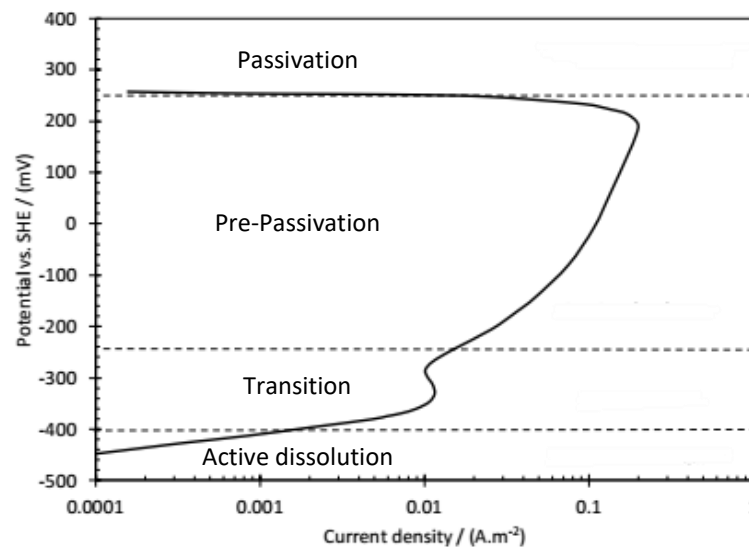
Source: Adapted from (EL MILIGY; GEANA; LORENZ, 1975; KAHYARIAN; BROWN; NEŠIĆ, 2018).

Different mechanisms are proposed for the iron dissolution (equation 33), one for pH bellow 4, and one for pH above 5. The intermediate pH range remains as a transition from one mechanism to another (ALMEIDA et al., 2017; HERNANDEZ; MUÑOZ; GENESCA, 2012; NEŠIĆ, 2007; THU; BROWN; NEŠIĆ, 2015). In strong acids, the mechanism in aqueous CO_2 solutions is described by equation 34 to 36 (NEŠIĆ, 2007). Equations 37 to 42 explain the mechanism for pH above pH5. Because H_2CO_3 and dissolved CO_2 are carbonic species

independent on pH, and since the concentration of CO_2 is dominant, it can be assumed the ligand $Fe_L = Fe-CO_2$ is formed as an adsorbed species at the electrode surface (NEŠIĆ, 2007).

$$Fe_{(s)} \rightarrow Fe^{2+} + 2e^- \tag{33}$$

C) Iron dissolution when the pH is below 4:

$$Fe_{(s)} + H_2O \leftrightarrow FeOH + H^+ + e^- \tag{34}$$

$$FeOH \rightarrow FeOH^+ + e^- \tag{35}$$

$$FeOH^+ + H^+ \leftrightarrow Fe^{2+} + H_2O \tag{36}$$

D) Iron dissolution when the pH is above 5:

$$Fe_{(s)} + CO_{2(aq)} \leftrightarrow Fe_L \tag{37}$$

$$Fe_L + H_2O \leftrightarrow Fe_LOH_{(ad)} + H^+ + e^- \tag{38}$$

$$Fe_LOH_{(ad)} \rightarrow Fe_LOH^+_{(ad)} + e^- \tag{39}$$

$$Fe_LOH^+_{(ad)} + H_2O \leftrightarrow Fe_L(OH)_{2(ad)} + H^+ \tag{40}$$

$$Fe_L(OH)_{2ad} \leftrightarrow Fe_L(OH)_{2(s)} \tag{41}$$

$$Fe_LOH_{2(s)} + 2H^+ \leftrightarrow Fe^{2+} + CO_{2(aq)} + 2H_2O_{(l)} \tag{42}$$
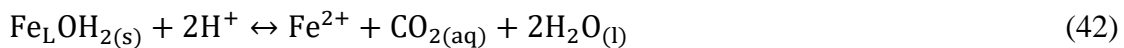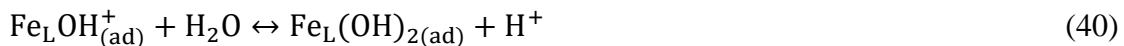
Kahyarian; Brown; Nešić, (2018) studied the mechanisms behind the CO_2-corrosion of an API 5L X65 mild steel. The methodology consisted of changing the pH, temperature and the pCO_2 at a high flow velocity setup. The authors concluded the following: i) the direct reduction of carbonic acid was negligible; ii) CO_2 played an effect on the limiting cathodic current, through affecting the CO_2 hydration reaction and carbonic acid dissociation; iii) the iron dissolution reaction was directly affected by the presence of carbon dioxide or its related carbonate species; and iv) the buffering ability of dissolved CO_2 and H_2CO_3 increased rate of iron dissolution in a CO_2 aqueous atmosphere.

2.4.2.2. Effect of pH, pressure and temperature

The pH of carbonate water solutions is a function of the combination of pressure, temperature, composition, and the availability of carbon dioxide. The acidity of H_2O/CO_2 solutions increases with pressure (Figure 28) and decreases with temperature because such

combination provides lower solubilities of carbonic acid (AQION, 2018; HANGX, 2005; HENRY, 1803; OLI STUDIO, 2016).

Figure 28: Effect of increasing pressure on the pH of the water/CO_2 solution at 25 °C.
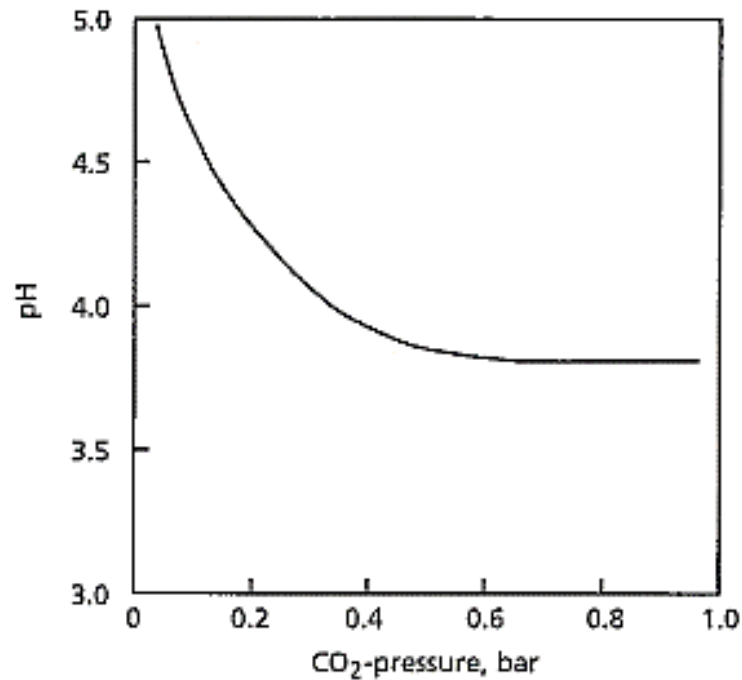
Source: (SCHÜTZE; ISECKE; BENDER, 2011).

The intensity of the corrosion is a consequence of the atmospheric parameters. For instance, it is known that acid brines tend to corrode faster than neutral or basic brines (see Figure 29). The reason behind that is the fact that the acidity tends to intensify the cathodic reactions. On the other hand, neutral or basic brines encourage low corrosion rates through the inverse behaviour and favouring the formation of protective scales (ALMEIDA et al., 2017; BARKER et al., 2018; HERNANDEZ; MUÑOZ; GENESCA, 2012; NEŠIĆ, 2007; SUN, 2006; THU; BROWN; NEŠIĆ, 2015).

Figure 29: The effect of pH in the absence of iron carbonate scales on measured and predicted corrosion rates. Test conditions: 20 °C, pCO_2 = 1 atm, 1 m/s, c_{Fe}^{2+} < 2 ppm.
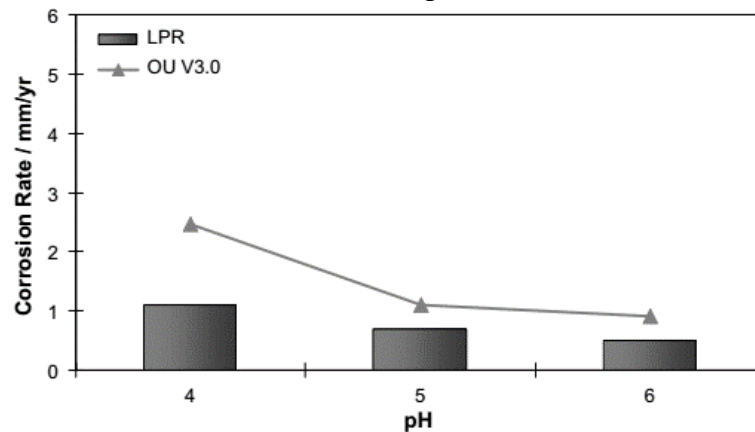
Source: (NEŠIĆ, 2007).

Moreover, though low temperatures tend to increase acidity and the solubility of CO_2, the temperature can also accelerate chemical and electrochemical processes. As a result, the morphology of the surface, nature and characteristics of the corrosion remains dependent of this variable. As such, various forms of corrosion, such as stress corrosion cracking, pitting or crevices, may result from specific combinations of temperature with pressure, microstructure, flow velocity, iron and oxygen contents. In the particular case of bulk CO_2-corrosion, the corrosion rates increase progressively until temperatures close to 70 and 90 °C. Beyond this range, the corrosion rates reduce because of the formation of thicker layers of stable corrosion scales. In the low-temperature range (0 to 20 °C) the mass transfer coefficient can diminish. Figure 30 demonstrates the effect of the temperature and the partial pressure of CO_2 on the corrosion of an API X65 steel (BARKER et al., 2018; HAN et al., 2007; KERMANI; MORSHED, 2003; LÓPEZ; PÉREZ; SIMISON, 2003; MITZITHRA; PAUL, 2016; NEŠIĆ; POSTLETHWAITE; OLSEN, 1996; SCHMITT; HÖRSTEMEIER, 2006; SUN, 2006).

Figure 30: a) Effect of temperature on the corrosion of an API X65 steel at pH4 - LSV in 0.1M NaCl solution with no CO$_2$. b) Effect of pCO$_2$ on the corrosion of an API X65 steel at pH4 - LSV in 0.1M NaCl solution at 30 °C.

a)

b)
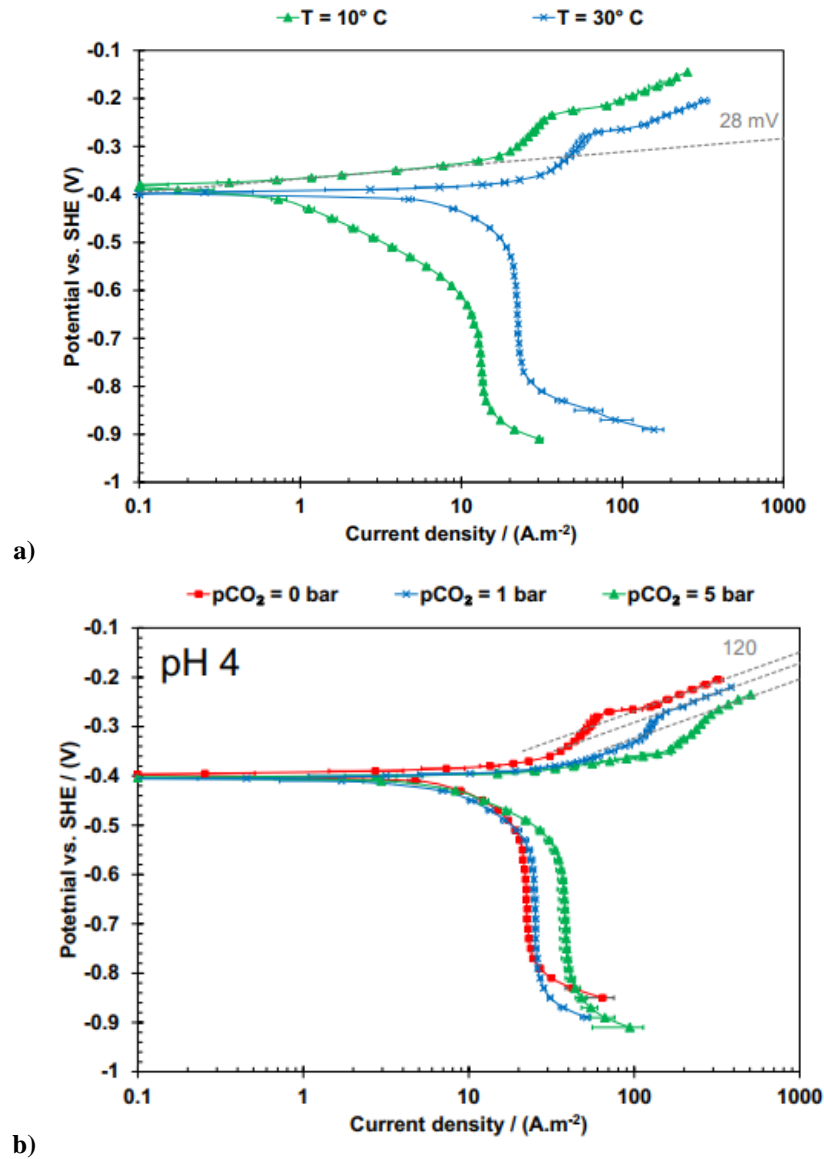
Source: (KAHYARIAN; BROWN; NEŠIĆ, 2018).

2.4.2.3. Effect of iron

Dugstad et al. (2015, 2018) studied the effect of iron in brine/CO$_2$ systems. The authors observed a decrease in the corrosion rates along with an increase in the pH. Models designed for bulk corrosion confirm that adding iron to water shall increase the pH. Data of the pH in CO$_2$ environments concerning the saturation level with iron obtained from the models employed in the literature are shown in Table 3.

Table 3: pH of water saturated with CO_2 and the effect of iron on the pH.

	SOLUTION	CO_2 [%]	P [atm]	TEMPERATURE [°C]	pH NON-SAT. SOLUTION	pH IRON SAT. SOLUTION
NORSOK M506	3.5%wt. NaCl	100	1	20	3.8	-
NORSOK M506	DISTILLED WATER	100	1	20	3.9	5.3
CORMED	3.5%wt. NaCl	100	1	20	3.8	5.2

Source: Adapted from (ROPITAL et al., 2000) and (STANDARDS NORWAY, 2005).

2.4.2.4. Scale and corrosion products

Corrosion products can form after the oxidation of iron and reaction with the carbonates. Many authors (BENJELLOUN-DABAGHI et al., 2002; CLEMENTS, 2008; CLEMENTS; ETHRIDGE, 2003; ERIKSEN; ENGELBRETH, 2014; HERNANDEZ; MUÑOZ; GENESCA, 2012; LIU et al., 2017; ROPITAL et al., 2000; RUBIN et al., 2012) report the formation of a type of iron carbonate known as Siderite ($FeCO_3$). The scale of $FeCO_3$ is built from precipitation mechanisms as soon as the concentrations of Fe^{2+} and CO_3^{-2} ions exceed the solubility limit. The formation of siderite is believed to occur via one-stage reaction between the iron ions and the carbonate ions (equation 43), even though reactions involving the iron ions and the bicarbonate have also been proposed (BARKER et al., 2018; DUGSTAD et al., 2018; HERNANDEZ; MUÑOZ; GENESCA, 2012; SK et al., 2017). Depending on the situation, $FeCO_3$ can cover a reasonable portion of the steel surface and provide an effective barrier for the diffusion of species (BARKER et al., 2018; BRONDEL et al., 1994; SUN, 2006; SUN; NEŠIĆ, 2008).

According to literature, the precipitation of $FeCO_3$ involves the steps of nucleation and growth, connected to the level of supersaturation (BARKER et al., 2018; SUN; NEŠIĆ, 2008). "Nucleation rate is said to rise exponentially with saturation value, whilst particle growth increases in a linear fashion (BARKER et al., 2018, p.316)". The crystal nucleation and growth can be divided into four behaviours based on the concentration of the reagents (Figure 31): i) dissolution, occurring in the undersaturation domain; ii) metastable/seeded, which happens in the supersaturation domain but the growth will only happen in the seed crystals; iii) heterogeneous nucleation/growth, involving the nucleation of foreign particles, followed by crystal growth; iv) homogeneous nucleation/growth, characterized by high supersaturation and

spontaneous nucleation and growth of crystal particles (BARKER et al., 2018; YANG, 2012). According to Sk et al. (2017), the growth of crystalline $FeCO_3$ is carried by equation 44.

Figure 31: Crystal growth.

Source: AUTHOR.

$$Fe^{2+}_{(aq)} + CO_3^{-2} \leftrightarrow FeCO_{3(s)} \tag{43}$$

$$Fe_{(s)} + CO_{3(aq)}^{-2} \leftrightarrow FeCO_{3(crystalline)} + 2e^{-} \tag{44}$$
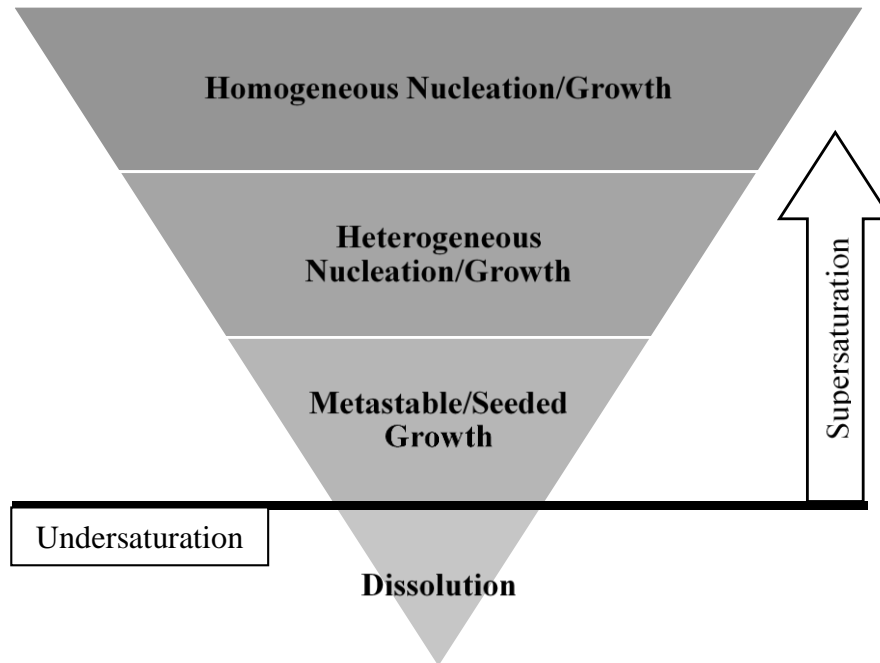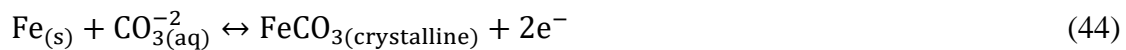
Different layers, composed of iron oxide, magnetite or Fe_3C, can result from CO_2-corrosion of carbon steel (MITZITHRA; PAUL, 2016; MORA-MENDOZA; TURGOOSE, 2002; TANUPABRUNGSUN et al., 2012). Nevertheless, many authors still claim the dominance of $FeCO_3$. Tanupabrungsun et al. (2012) constructed Pourbaix diagrams for CO_2-corrosion of mild steel at various temperatures (see Figure 32). The authors concluded that $FeCO_3$ and $Fe_2(OH)_2CO_3$ were dominant at short-term experiments but, in more extended tests, the $Fe_2(OH)_2CO_3$ transforms into $FeCO_3$.

Figure 32: Pourbaix diagrams for Fe-CO$_2$-H$_2$O systems at various temperatures (symbols: • - bulk pH, ° - surface pH). a) 25 °C. b) 80 °C. c) 120 °C. d) 150 °C.
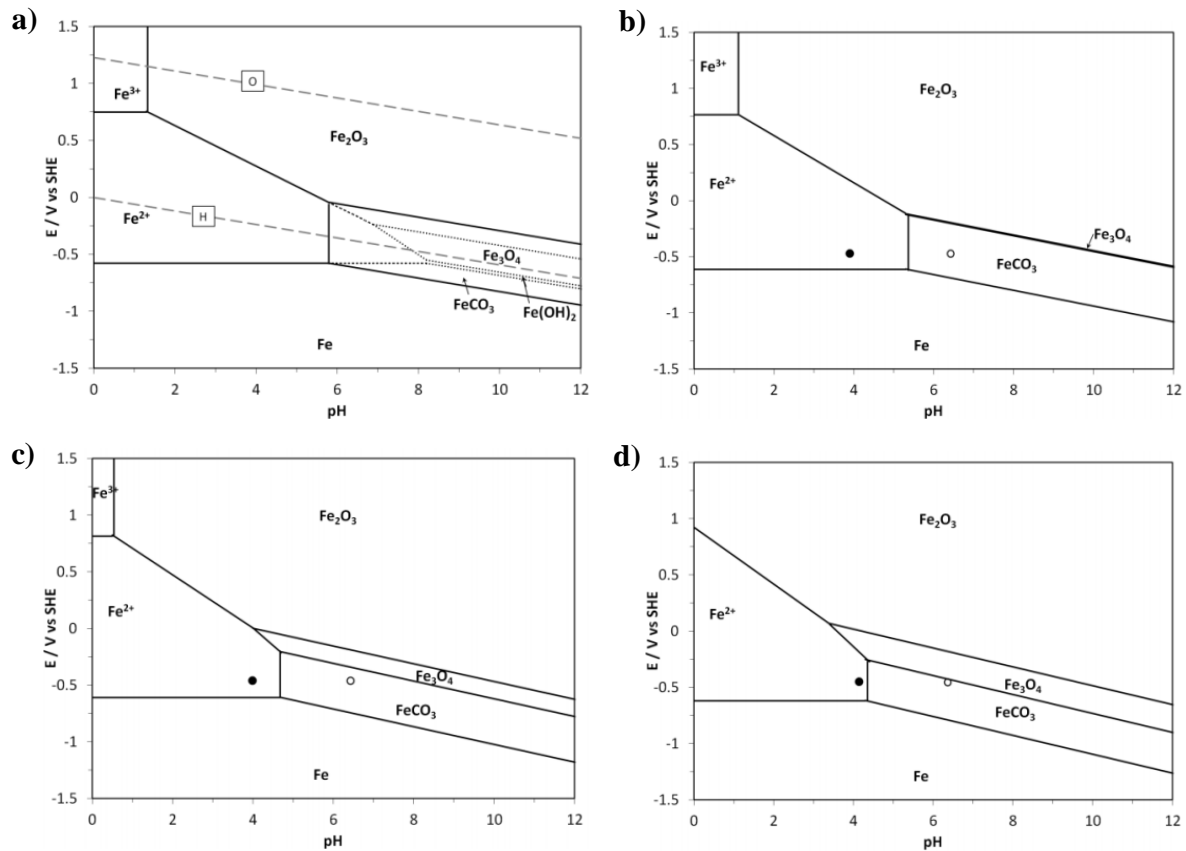
Source: (TANUPABRUNGSUN et al., 2012).

2.4.2.5. Effect of oxygen

In field applications, the structural layers of the pipe may experience corrosion with certain amounts of oxygen, in unrepaired failures of the outer sheath for example. Oxygen acts as a noxious chemical species that increases the corrosion rates, through enhancing the rate of the cathodic reactions and, also, due to chemical destabilisation of the corrosion protective scales that are stable in anaerobic conditions (LÓPEZ; PÉREZ; SIMISON, 2003).

2.4.2.6. Effect of calcium

Dugstad et al. (2015, 2018) studied how the calcium ions present in seawater may affect the formation of FeCO$_3$. The authors observed that calcium ions react to the dissolved carbonates and form calcium carbonates (CaCO$_3$). The kinetics of CaCO$_3$ formation is faster than the formation of FeCO$_3$. Therefore, a considerable portion of carbonates can be consumed

when calcium ions are present, making the formation of $FeCO_3$ more difficult. As a result, the level of protection offered by $FeCO_3$ can be compromised (BARKER et al., 2018).

2.4.2.7. Effect of the water flow velocity

Unrepaired failures expose the structural layer of the pipe to non-stagnant electrolytes, that is to fluids colliding with the steel at given flow velocities. The impingement of the fluid increases the corrosion rates by continuous erosion and dragging of the existing protective films or through enhancing mass-transfer corrosion mechanisms near the surface of the steel. Beyond erosion–corrosion, the flow velocity of the seawater can also trigger localised corrosion mechanisms related to the mechanical destabilisation of passive scales (LÓPEZ; PÉREZ; SIMISON, 2003).

2.4.2.8. Effect of the microstructure and chemical composition of the steel

The chemical composition and the microstructure of steels are known factors affecting the CO_2-corrosion. However, the accurate definition of their effective influence remains under development, since conflicting results are found in the literature (BARKER et al., 2018; KERMANI; MORSHED, 2003; LOPEZ et al., 2003; LÓPEZ; PÉREZ; SIMISON, 2003). Despite the uncertainties, some aspects are worth mentioning, as follows:

i) Though it was not clearly determined the quantitative influence of the chemical composition, heat treatment and microstructure, these factors clearly impact the corrosion rates.

ii) A large number of recent studies indicate that ferritic-pearlitic microstructure has better corrosion resistance than martensitic or martensitic-bainitic microstructures.

iii) Microstructure and chemical composition interact with the stability, adherence and distribution of carbides in the matrix.

iv) Additions of Cr, Mo, Cu, S and Ni to the composition of the carbon steel may reduce the corrosion rates and corrosion tendency.

2.4.3. Annulus corrosion

Over the last decade, the study of the CO_2-corrosion in unbounded flexible pipes has gone through large developments as new cases of failure have been reported. Despite the efforts of industry and academic community to understand the corrosion mechanisms, many uncertainties remain, including those connected to the broad range of possible environmental scenarios experienced by the flexible pipe concerning the annulus. Also, the annulus corrosion of the structural wires is challenging because it not only requires knowledge of the common aspects of bulk corrosion but also from the peculiarities of testing the materials in occluded spaces. Many well-established electrochemical corrosion techniques become challenging to employ, thanks to geometrical and chemical constraints (ERIKSEN; ENGELBRETH, 2014; HERNANDEZ; MUÑOZ; GENESCA, 2012; LIU et al., 2017).

Previous studies shed light on the effect of the degree of occlusion on the corrosion rate, i.e. the free volume (or volume of water) to steel surface area (V/S) present in the annulus. According to the literature, degrees of occlusion ranging from 0.03 to 0.1 ml/cm² exist in flexible pipes. The work to date shows that the corrosion rate decreases as V/S is reduced (see Figure 33). The typical values for CO_2-corrosion rates for such degree of occlusions lie below 0.01 mm/y. Besides the direct impact, the confinement can be a crucial factor due to its influence on other variables such as pH, precipitation rate, stability of corrosion products and etc. (4SUBSEA, 2013; CLEMENTS, 2008; CLEMENTS; ETHRIDGE, 2003; DUGSTAD et al., 2015; ROGOWSKA et al., 2016; ROPITAL et al., 2000; RUBIN et al., 2012; UNDERWOOD, 2002).

Figure 33: Corrosion rate as a function of the V/S ratio.
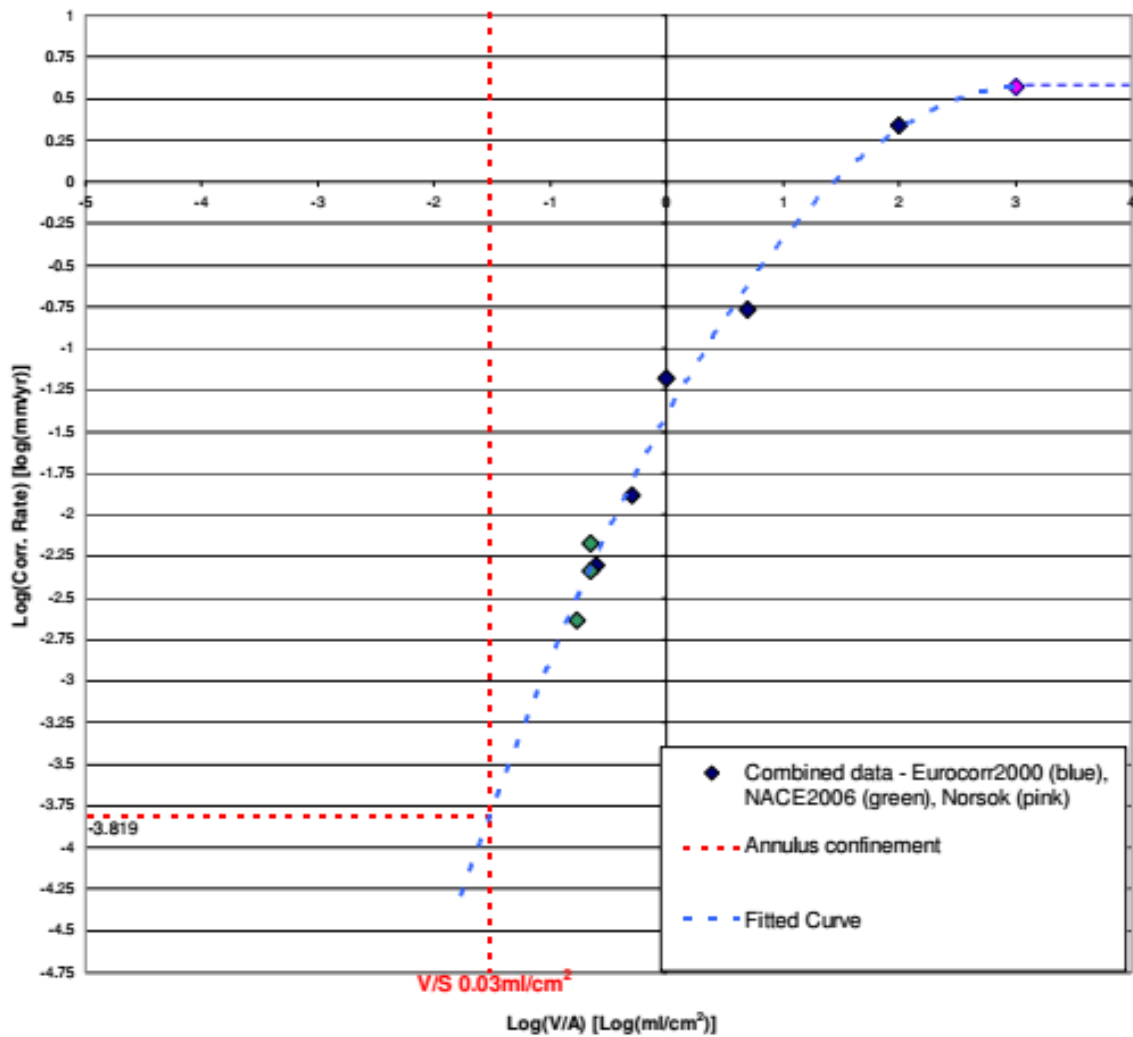
Source: (CLEMENTS, 2008).

Ke et al. (2017) studied the combination of confinement and pressure on the evolution of pH at ambient temperature. The authors observed an increase in pH to a peak before stabilising (see Figure 34). This behaviour was attributed to the rise in concentrations of iron ions and bicarbonate. The works of Dugstad et al. (2015, 2018) seem in line with this statement as they show an increase in pH when the concentration of iron ions in the solution was artificially raised.

Figure 34: Long-term evolution of pH measured in a confined test cell at ambient temperature, under 1 to 45 bar (44,4 atm) of CO_2.
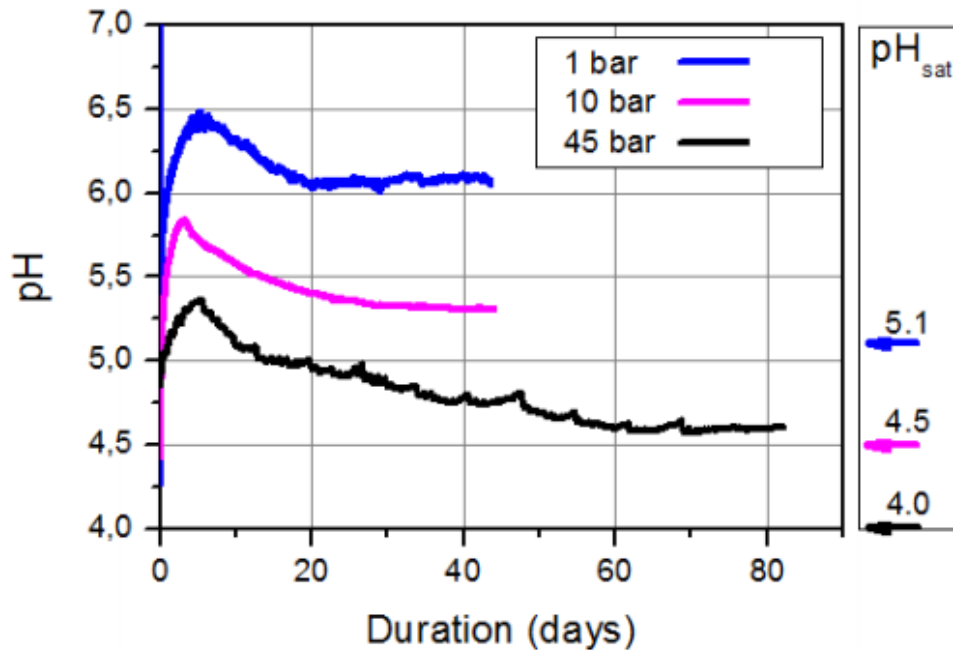
Source: (KE et al., 2017).

When the concentrations of iron ions exceed the solubility limit, mineral forms of iron carbonate can form, by precipitation mechanisms, adhering on the surface of the structural layers of the pipe. Once the precipitation rate exceeds the corrosion rate, the scale formed on the surface of the steel is considered as protective (NEŠIĆ, 2007; SUN, 2006; SUN; NEŠIĆ, 2008). Sun and Nešić (2018) deduced equation 45 that describes the rate of precipitation (PR_{FeCO3}) in mol/m³s when all of the ferrous ions end up on the steel surface. It can be observed that PR_{FeCO3} is a function of the concentrations of iron (c_{Fe}) and carbonate (c_{CO32-}), of the supersaturation level of $FeCO_3$ (SS_{FeCO3}, see equation 46), of the temperature (T), of the degree of occlusion (V/S), of the solubility limit (K_{sp}, see equation 47), of the kinetic constant (K_r, see equation 48) and of the constants "C3", "C4" and "R", described in the literature (KE et al., 2017; NEŠIĆ, 2007; SUN, 2006; SUN; NEŠIĆ, 2008). It can be noticed that the precipitation rate of $FeCO_3$ increases when the degree of occlusion is reduced. Besides that, the atmospheric conditions can also affect the precipitation rate of $FeCO_3$ directly through an impact on the solubility limits of chemical species in the solution (AQION, 2018; BARKER et al., 2018; HANGX, 2005; HENRY, 1803; OLI STUDIO, 2016).

$$PR_{FeCO_3} = K_r \frac{K_{sp}}{V/S}(SS_{FeCO_3} - 1) \tag{45}$$

$$SS_{FeCO_3} = \frac{c_{Fe^{2+}} \times c_{CO_3^{2-}}}{K_{sp}} \tag{46}$$

$$logK_{sp} = -59.3498 - 0.041377T - \frac{2.1963}{T} + 24.5724 \log(T) + 2.518I^{0.5} - 0.657I \tag{47}$$

$$K_r = e^{C3 - \frac{C4}{RT}} \tag{48}$$

Since the protective precipitates tend to adhere on the surface of the steel, it becomes interesting to explore the effect of the coverage of the surface by the action of a protective scale, such as $FeCO_3$. Remita (2008) modelled the impact of the coverage aspect (θ) on the surface of steel in brines at 1 atm of carbon dioxide. The authors concluded that a considerable reduction of the corrosion rate and pH should occur when more insulating scales cover the surface; see Figure 35 and Figure 36. Furthermore, it is reasonable to assume that the magnitude of θ could grow over time, as continuous layers of precipitates accumulate on the surface of the steel. The effect of time was also covered in the work of Clements (2008), where the author observes a reduction of the corrosion rate with time (see Figure 37).

Figure 35: Corrosion rate as a function of the V/S ratio for different θ at $pCO_2 = 1$ atm and 20 °C.
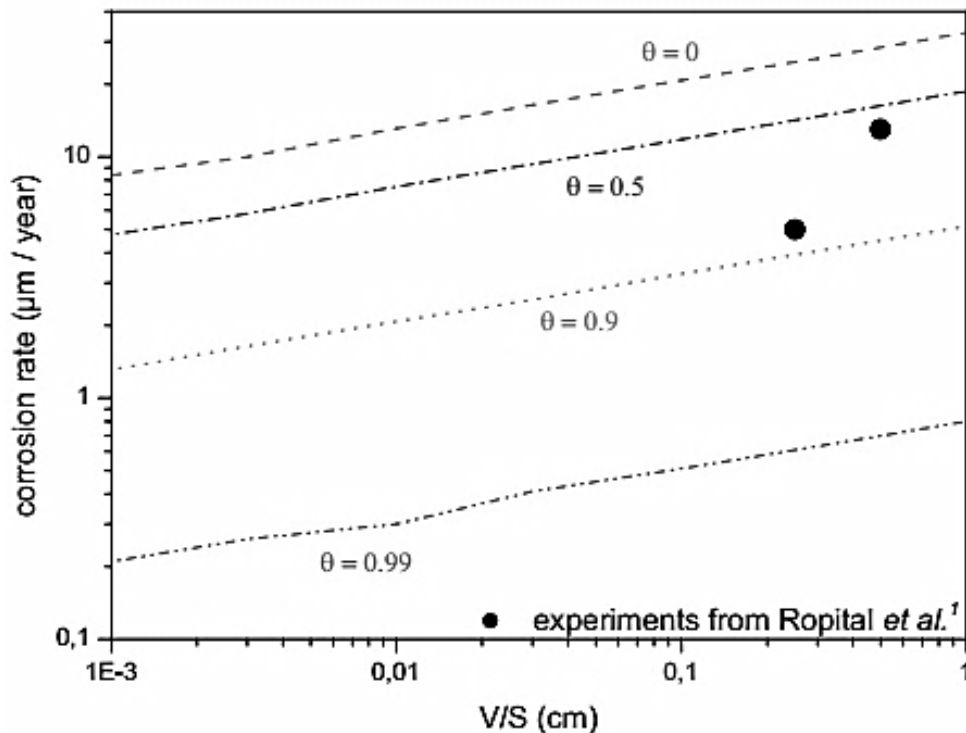
Source: (REMITA et al., 2008) and (ROPITAL et al., 2000).

Figure 36: pH as a function of the V/S ratio for different θ; at pCO_2 = 1 atm and 20 °C.
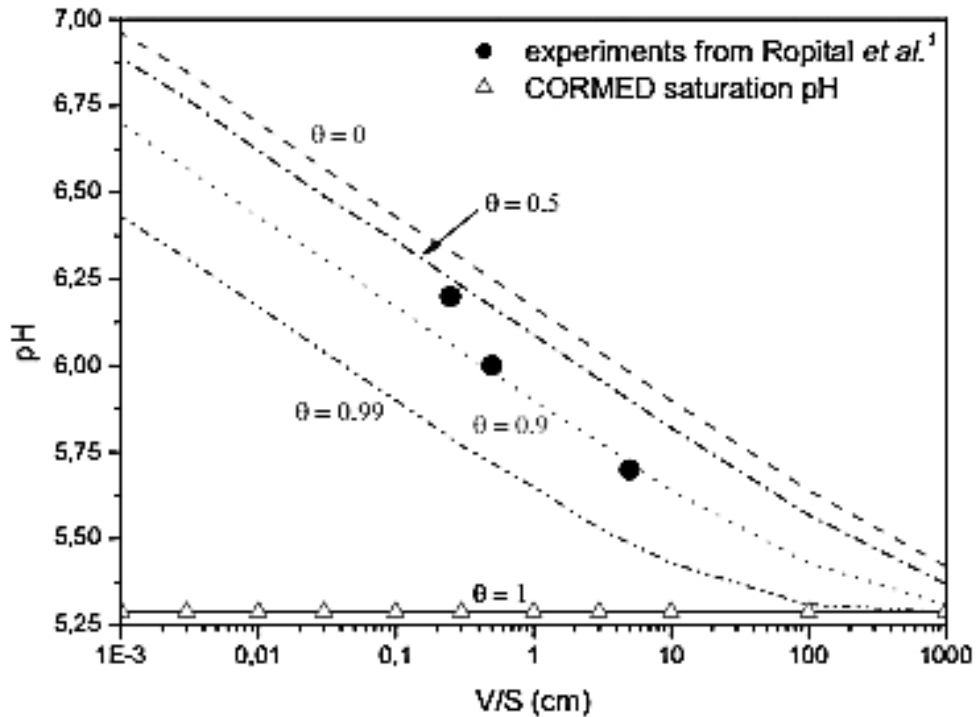
Source: (REMITA et al., 2008) and (ROPITAL et al., 2000).

Figure 37: Annulus corrosion rate from weight loss measurements of specimens in CO_2 saturated deionised water at 50 °C.
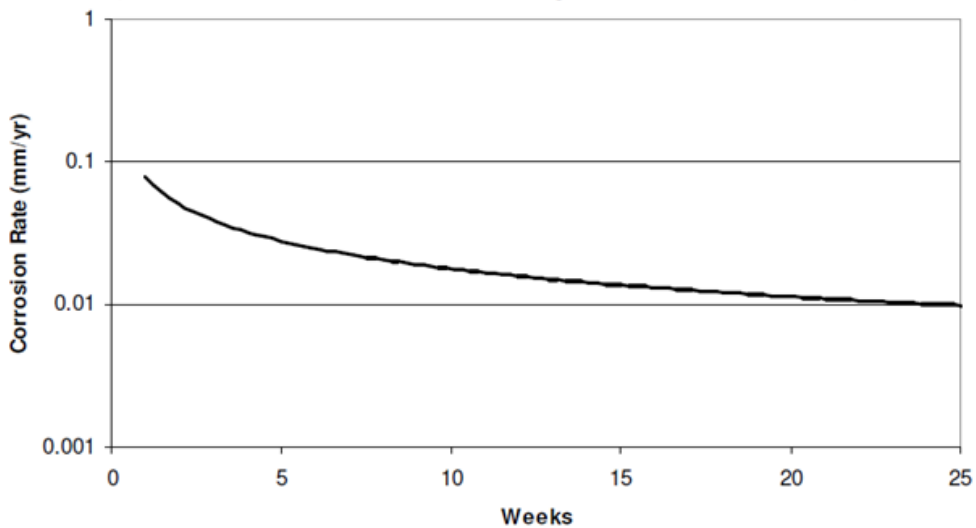
Source: (CLEMENTS, 2008).

Despite the factors intimately tied to the degree of occlusion, a massive effort was dedicated over the last decades to explore CO_2-corrosion in terms of mechanisms, morphology and corrosion products (ALMEIDA et al., 2017; BARKER et al., 2018; CROLET; THEVENOT; NEŠIĆ, 1998; HAN et al., 2007; MORA-MENDOZA; TURGOOSE, 2002; SCHMITT; HÖRSTEMEIER, 2006; SUHOR et al., 2012; SUN, 2006; SUN; NEŠIĆ, 2008;

TANUPABRUNGSUN et al., 2012), temperature and environmental aspects, (ALMEIDA et al., 2017; BARKER et al., 2018; MITZITHRA; PAUL, 2016; ROSLI et al., 2016) microstructure and chemical composition of the steel, (BARKER et al., 2018; LIU et al., 2016; LOPEZ et al., 2003; LÓPEZ; PÉREZ; SIMISON, 2003) properties and characteristics of the electrolyte (BARKER et al., 2018; DUGSTAD et al., 2015, 2018; FANG; BROWN; NEŠIĆ, 2013; ZENG; LILLARD; CONG, 2016). However, little information was found concerning the effect of CO_2 flow rates. Many studies do not state the flow rates or the surface area of steel, making it difficult to compare data regarding the relative flow rates.

As the flow rate of carbon dioxide into the annulus is primarily controlled by the permeability of the polymer sheath containing the bore fluid, and that permeability will vary depending on the polymer structure and its thickness, it seems that flow rate is a variable worth exploring. Most standard corrosion tests would employ relatively high flow rates in order to obtain saturated solutions from the beginning of a test, which contrasts with the relatively slow establishment of the annulus conditions evolving in service through diffusion of molecules through the inner polymer sheath (DÉSAMAIS; TARAVEL-CONDAT, 2009; HAAHR et al., 2016; KE et al., 2017).

Moreover, in the event of a breach of the outer sheath, seawater ingress the annulus at hydrostatic pressure and temperature respective to the depth of the failure. A recent failure of a flexible pipe operating as a CO_2 injection line in Brazil confirms the existence of different forms of corrosion other than uniform corrosion. This particular failure brought the attention of the oil and gas community to the possible deterioration of tensile wires by stress-corrosion cracking (SCC), in pipes operating with high concentrations of carbon dioxide (CHETWYND, 2017). The mechanisms of SCC in flexibles remains under investigation, but according to Schmitt and Hörstemeier (2006), the susceptibility of high strength carbon steel to SCC in CO_2 wet environments increases with the partial pressure of carbon dioxide, temperatures and applied mechanical loads.

The work of Borges (2017) reveals the possibility of localised CO_2-corrosion in the tensile wires on a real-scale test. The occurrence of pits in CO_2-containing environments is associated by Han et al. (2007) with moderate iron carbonate supersaturation, which seems in line with the results shown by Borges (2017).

The phenomenon of pitting in wet CO_2 divides into two stages: initiation and growth. The initiation is related to a chemical removal or mechanical breakdown of a protective scale of $FeCO_3$ (HAN et al., 2007). Brondel et al. (1994) link the occurrence of pitting and crevice with the contact of the surface of the steel with carbonic acid. Mitzithra and Paul (2016) studied

low-temperature CO_2-corrosion of an API 5L X65 carbon steel (quenched and tempered). The authors observed initiation of pits caused by the preferential dissolution of ferrite (see Figure 38). The layers of cementite (Fe_3C) left on the surface of the steel acted as cathodic sites, enabling the formation of a localised galvanic pair. The growth stage of pits in CO_2-containing waters was connected to a localised galvanic mechanism between a cathode and an anode (HAN et al., 2007; MITZITHRA; PAUL, 2016).

Figure 38: Localised corrosion on a specimen in CO_2-saturated brine at 10 °C.
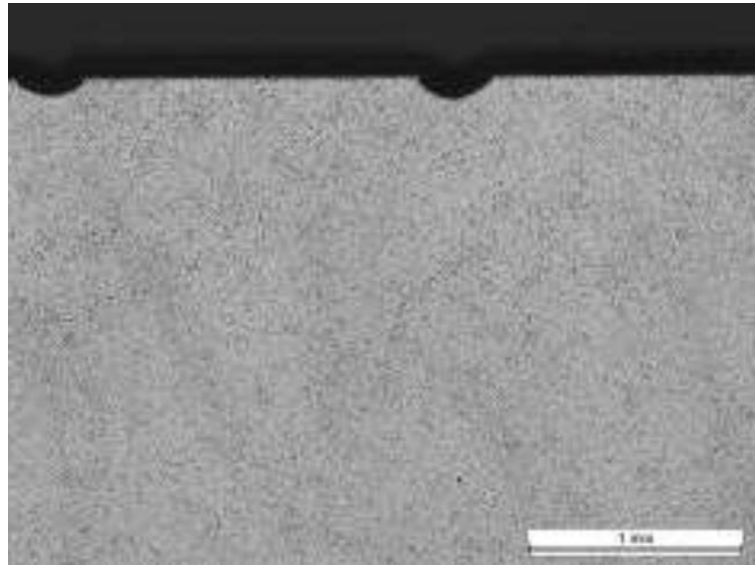
Source: (MITZITHRA; PAUL, 2016).

3.   MATERIALS AND METHODS

3.1.   ORGANISATIONAL CHART

Figure 39 shows an organisational chart presenting the methodology of the work, divided into three categories: general simulations, laboratory experiments and exploration of environmental aspects. The laboratory experiments were conducted according to the results provided by the general simulations. The software packages were not only used to reproduce and enhance the quality of the experimental results but also to search for more critical corrosion patterns and to reduce the gaps of knowledge linked to the environmental conditions of the water solution.

Figure 39: Organisational chart.
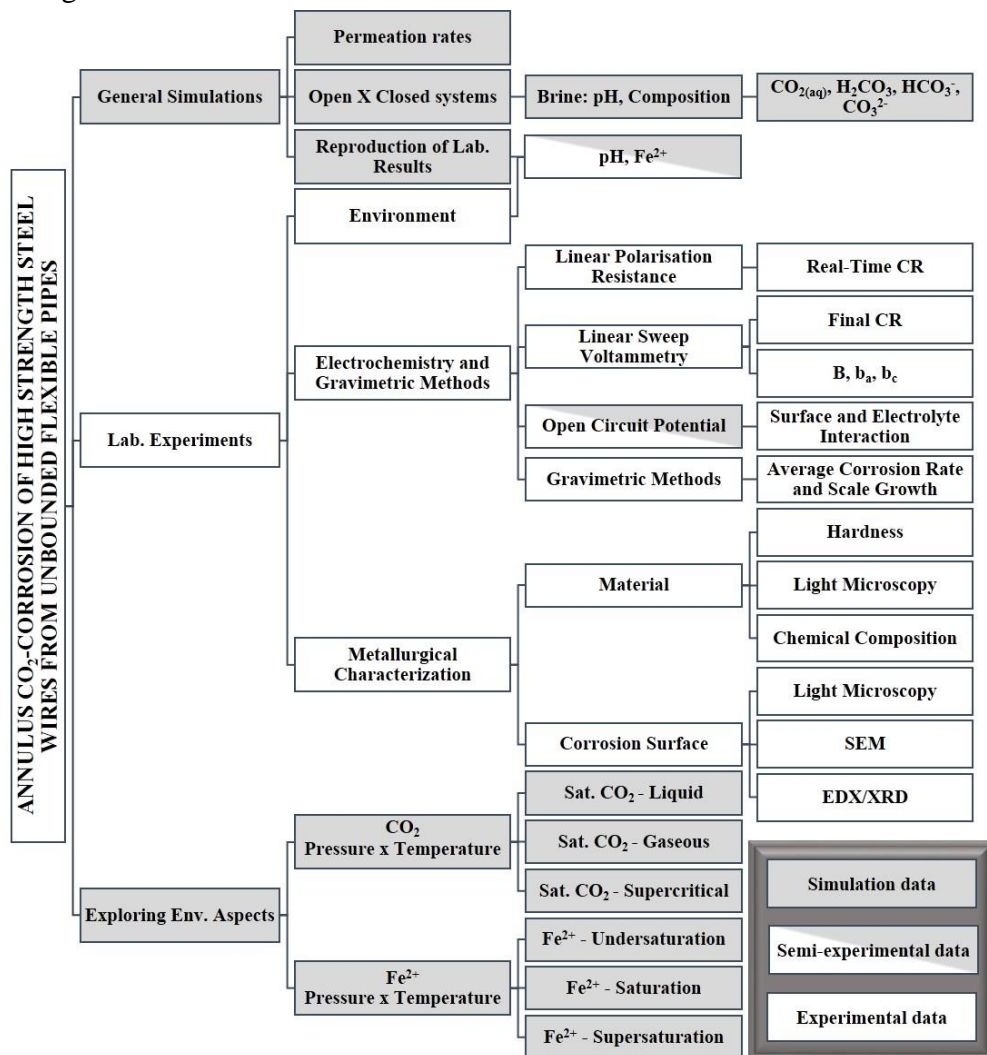
Source: AUTHOR.

3.2.   GENERAL SIMULATIONS

3.2.1.   Carbon dioxide flow rate calculations

The flow rate of CO_2 per surface of the steel (FR/SS) was selected as a controlled parameter used to reproduce the process of permeation happening in the annulus. The term flow rate is used throughout this work to represent the flow rate per square centimetres of steel. The value employed in the reproduction of the annulus CO_2-corrosion derived from the outcome of software developed to predict the annulus environment. An additional experiment conducted with a flow rate augmented by a factor of 100 times was performed to study the influence of the parameter FR/SS on the corrosion process. The software employed models the pipe structure, service conditions and calculates the flux and partial pressure of the gases in the annulus. It is recognised that substantial efforts are currently being dedicated to improving the precision of the models available designed to the assessment of the permeation rates of gases entering the annulus. However, it should be highlighted that the software used here consisted of the best tool available at the given moment. Further details regarding the name of the software and polymer grades employed are kept confidential.

Five input conditions representative of extreme CO_2 service were simulated. The parameters ranged as follows: pressures in the bore ranging from 300 to 800 bar (296,077 to 789.5 atm); temperatures ranging from 60 to 80 °C; surfaces per length of 330 cm^2/cm_{length} and 531 cm^2/cm_{length}; and three different polymer grades, which are relevant to the structures employed in the field. Information about the exact type of polymer grade employed was suppressed, due to confidentiality constraints.

3.2.2.   Commercial software packages

The state and the characteristics of 3.5%wt. NaCl solution was simulated with the help of two commercial models: OLI Studio™ and Aqion™. Both software packages are suited to simulate equilibrium reactions, ion exchanges, surface complexes, solid solutions and gases. They were used in a complementary manner, as different databanks and modelling strategies are employed.

OLI Studio™ can work with two databanks: Aqueous Phase (AQ) and Mixed Solvent Electrolyte (MSE). AQ was selected, as it is well suited to the environment examined in the experiments; the validity ranges are displayed in Table 4.

Table 4: Validity range of the software OLI Studio™.

Databank/model:	Aq (Aqueous Phase)
Chemicals:	Aqueous electrolytes ($x_{H2O} > 0.65$)
Ionic strength (mol/mol):	$0 < I < 30$
Pressure range (atm):	0 to 1480
Temperature range (°C):	-50 to ~300

Source: (OLI STUDIO, 2016).

Aqion™ is a model inspired by the geochemical model PHREEQC. The environment is modelled by the common activity model, which is calculated either by equation 49 (also known as Davies equation) or by equation 50 (also known as WATEQ Debye-Hückel equation). The term "$\gamma_\pm$" are activity coefficients, "IS" is the ionic strength, "z_j" is the valence of ion "j", "a_j^0" and "b_j" are ion-specific parameters. "C1" and "C2" are variables depending on temperature. The validity range of the models is defined by the ionic strength, limited to values below 1M.

$$\log\gamma_\pm = -C1z_j^2\left(\frac{\sqrt{IS}}{1+\sqrt{IS}} - 0.3IS\right), \ IS \leq 0.5M \tag{49}$$

$$\log\gamma_\pm = -C1z_j^2\left(\frac{\sqrt{IS}}{1+C2a_j^0\sqrt{IS}}\right) + IS \cdot b_j, \ IS < 1M \tag{50}$$

3.2.3. Boundaries and assumptions for the reproduction of the experimental results

It is assumed the possibility of two main boundary conditions: open and closed carbonate systems. As detailed in the literature review, the difference between them lies in the fact that closed carbonate system does not allow the exchange of matter with the neighbourhood, whereas open carbonate system does. Figure 40 shows a sketch, presenting the main assumptions of the system (annulus) and its neighbourhood. Simulations of titrations are used to highlight the differences between boundaries. The simulation of the titration involves modelling additions of NaOH or HCl into the solution, in order to alter the pH and the composition. The chemical species of interest were: hydrogen ions, carbonic acid, bicarbonate and carbonate. It is assumed that carbon dioxide undergoes slight hydration (~ 0.26 %) to H_2CO_3, and that usual analytical methods do not clearly distinguish between the dissolved carbon dioxide and the carbonic acid. Hence, these chemicals are represented as one component, described by the term "$CO_{2(aq)}$". Such a convention is used and supported elsewhere (AQION, 2018; KORDAČ; LINEK, 2008; OLI STUDIO, 2016).

Figure 40: Main interactions between the system and the neighbourhood. a) Open carbonate system and b) Closed carbonate system.

Source: AUTHOR.
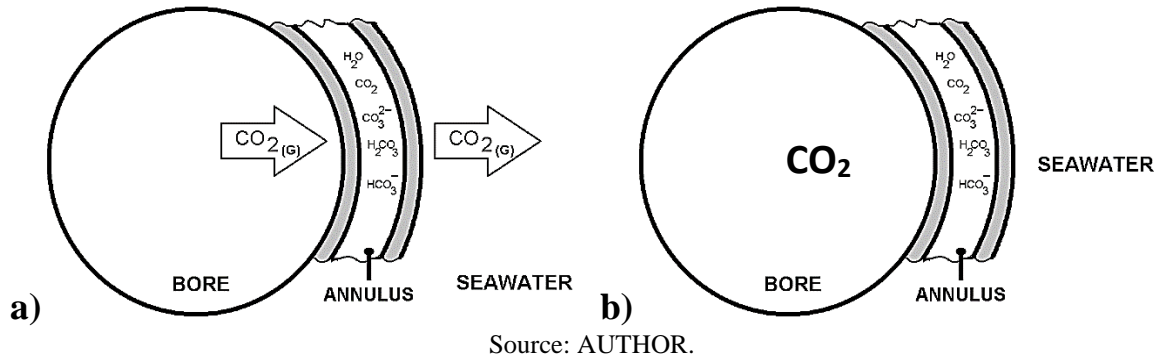
The data obtained in the laboratory were used for validation of the models and boundaries. Based on the experimental outcomes, the simulation assumed that under various atmospheric conditions the high strength steel tensile wires should corrode and release iron ions in the annulus. The concentration of iron can evolve towards the supersaturation domain, eventually causing pH variations and precipitation of corrosion products. Beyond this stage, the concentration of iron should return toward the saturation level or close. The formation of $FeCO_3$ as the protective scale has been presumed because many authors support its dominance in pure CO_2-corrosion. Nonetheless, a confirmation of such a scale was carried by X-ray diffraction (XRD) (BARKER et al., 2018; DUGSTAD et al., 2015, 2018; HERNANDEZ; MUÑOZ; GENESCA, 2012; KE et al., 2017; NEŠIĆ, 2007; RUBIN et al., 2012; SUN, 2006; TANUPABRUNGSUN et al., 2012).

3.3. LABORATORY EXPERIMENTS

3.3.1. Material

High strength steel tensile wires, taken from the first and second tensile layer of a water injection jumper, were used in this work. The alloy is of interest for service in deep wells, because it offers high strength to weight ratio. Thus, it is suited to supporting the high loads imposed in deep-water developments. The wires have nominal UTS higher than 1400 MPa. The main strengthening alloy element was carbon, at the content of 0.68% in weight. Further details regarding microstructure, hardness and chemical composition were suppressed due to confidentiality constraints.

3.3.2. Experimental matrix

Table 5 summarises the experimental conditions investigated. The tests were conducted at 30 ± 2 °C and atmospheric pressure, with a carefully controlled flow rate of CO_2. The simulation of flux due to permeation was the basis for the magnitude of the flow rate of CO_2 per surface of steel used in laboratory experiments. A flow rate of 0.0008 ml.min^{-1}.cm^{-2} was selected for the reproduction annulus corrosion (experiment N° 1). This flow rate is considered close to the values obtained by simulations of the permeation rates at critical CO_2 operating conditions, as well as being practically achievable in the laboratory.

The literature suggests that a higher flow rate could alter the state and time to establish steady-conditions. Therefore, one additional short-term experiment (experiment N° 2) was carried at the FR/SS of 0.0785 ml.min^{-1}.cm^{-2}. Such a magnitude was selected to ensure a significant difference in the variable being examined and to represent something closer to what would be used in a more typical corrosion experiment.

Table 5: Summary of the corrosion tests carried out in 3.5 %wt. NaCl solution. The matrix presents the following parameters: flow rate of CO_2 per unit surface of steel (FR/SS), degree of occlusion (V/S), pressure, type of gas, temperature and time.

N^o	FR/SS [ml/min/cm^2]	V/S [ml/cm^2]	Pressure [atm]	Gas type	Temp. [°C]	Time [Months]
1	0.0008	~0.2	1	CO_2	30 ± 2	4
2	0.0785	~0.2	1	CO_2	30 ± 2	2

3.3.3. Test details

The test vessel comprised of 500 ml cylindrical glassware, each containing simultaneously 52 high strength steel tensile wires and around 260 ml of brine. From the total of samples in each experiment, 2 samples are used for the electrochemical measurements (WE$_1$ and WE$_2$). The remaining material is used as steel coupons and for surface characterization.

The surface preparation for all samples involved submersion in Clarke`s reagent (3 cycles of 15 minutes each) at ambient temperature to remove surface oxides (AMERICAN SOCIETY FOR TESTING AND MATERIALS, 2003). The test solution was 3.5 %wt. NaCl, prepared by the addition of high-grade reagent to de-ionised water. Deaeration was performed prior to the introduction of water into the glass test vessel and the introduction of carbon dioxide. The oxygen concentration was reduced to values below 10 ppb using nitrogen purging

before transfer into the pre-purged vessel, in order to avoid preferential corrosion by dissolved oxygen. After deaeration and transfer of the test solution, CO_2 (99.995%) was introduced at the intended flow rate. At the end of the test, all samples were immediately dried, placed in a desiccator and filled with N_2 to avoid atmospheric corrosion.

3.3.4. Environment monitoring

Measurements of pH and iron in solution were monitored on a regular basis over the duration of the tests. A special modification to the setup of the glass test vessel allowed the measurement of pH and the sampling of iron ions in solution with minimal disturbance of the test environment (see Figure 41). Both the pH and iron measurements were performed forcing the passage of the solution contained in the lower part of the test cell through the same piping used for gas inlet. This procedure was performed to improve the representativeness of the analysed solution and to prevent the measurement of solutions stagnant in the pipe, which would not be representative of the test. Another advantage of the setup used in this work was that it is not necessary to keep the gauge used to measure pH permanently connected to the test cell. This allowed calibration before every measurement without the risk of disturbing the test environment.

The most significant changes in behaviour were expected to take place in the initial stages of the test. Hence, a higher frequency of sampling was performed at the beginning and was reduced throughout the experiment, as more stable conditions developed. Also, the volume of each aliquot removed for measurement of iron (2.5 ml) was minimised to prevent any significant change to the degree of occlusion. It is expected that the total change in the degree of occlusion, due to the aliquots would lie below 0.03 ml/cm². In the literature, the concentration of iron is frequently presented in mg/l, instead of mol/l, so the first unit is preferred in this work to describe the evolution of iron concentration. The latter unit (mol/l) is used for the other chemicals in the solution due to practicality concerning simulation.

Figure 41: a) Glass test vessel. b) Water sampling for iron ions.
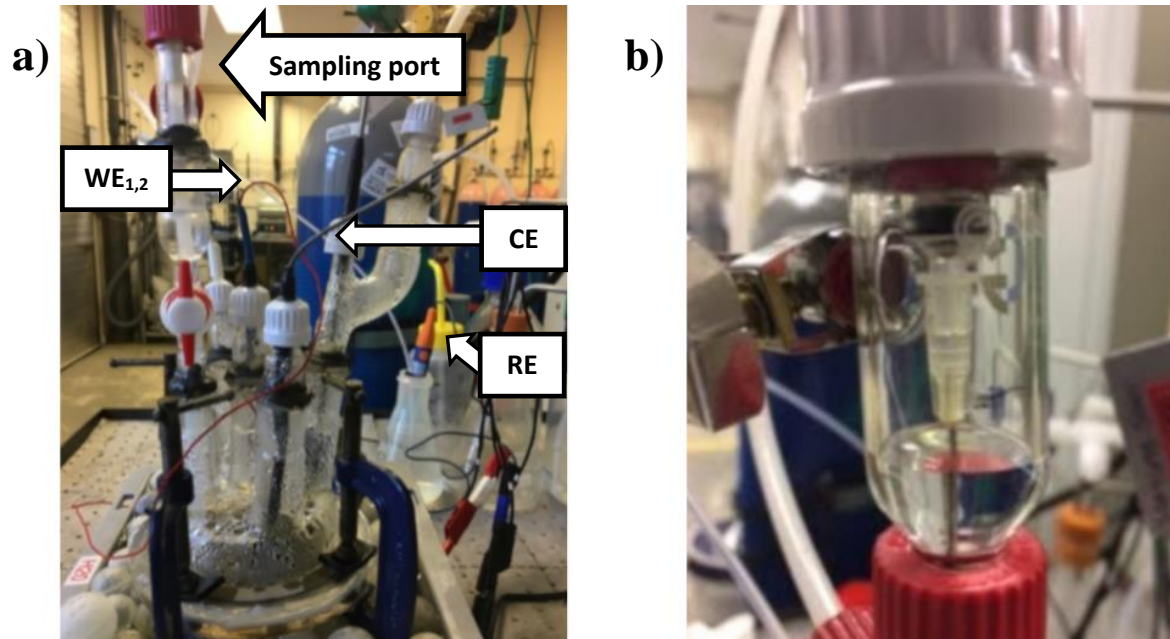
Source: AUTHOR.

3.3.5. Electrochemistry

The electrochemical analyses were conducted with a three-electrode electrochemical setup and an Ivium Vertex potentiostat/galvanostat. Each glass vessel contained two samples selected as working electrodes (WE_1 and WE_2), one platinised titanium counter electrode (CE), and one reference electrode of Ag/AgCl (RE), connected to the test solution by a commercial polymer salt bridge. Figure 41 and Figure 42 show the careful arrangement of the electrochemical specimens. The electrodes, thermocouple, the salt bridge and the coupons were all positioned vertically in the glass vessel. The CE and the salt bridge were placed between the working electrodes.

The areas of the working electrodes wire samples were measured with the software Image J and ranged from 0.808 to 0.903 cm². The remaining surface area was covered with a lacquer to prevent corrosion and electric contact from the other wires confined in the vessel. This step was critical for obtaining reliable electrochemical data.

Figure 42: Scheme of the electrode layout for an electrochemical test in the occluded environment. The detail shows the steel surface and the anti-corrosion lacquer used to define it.
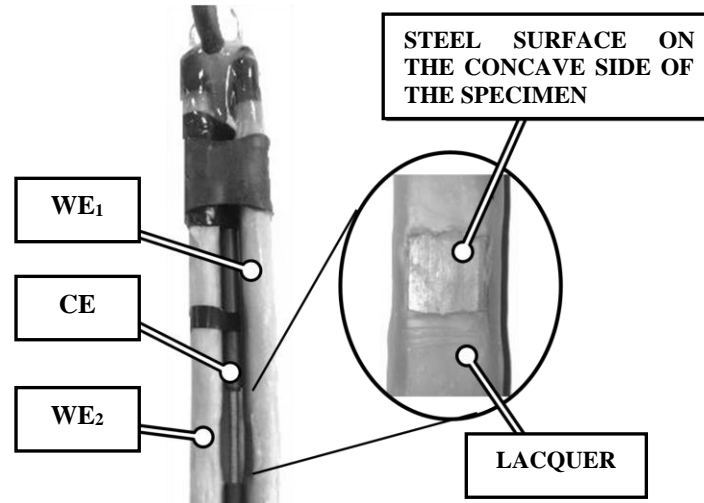
The electrochemical techniques employed in this work were open circuit potential (OCP), linear polarisation resistance (LPR) and linear sweep voltammetry (LSV).

LPR is a non-destructive technique designed for rapid real-time corrosion monitoring. The linear polarisation resistance analysis employed a range of -10 mV to +10 mV from OCP, at a scan rate of 1 mV/s. The corrosion rates were calculated using equations 51 to 54 according to ASTM G59-97. The term "j_{corr}" is the corrosion current density, "B" is the Stern-Geary factor, "Rp" is the polarisation resistance, "E" is the potential, "i" is the current density, "b_a" and "b_c" are anodic and cathodic Tafel slopes, "CR_{LPR}" is the corrosion rate given by LPR in mm/y, "EW" is equivalent weight of the steel, "ρ" is the density of the steel (AMERICAN SOCIETY FOR METALS INTERNATIONAL, 2003; AMERICAN SOCIETY FOR TESTING AND MATERIALS, 1989, 1997; DENZINE; READING, 1997; PEREZ, 2004; ROBERGE, 2000; WOLYNEC, 2003). As well as occurred with the environment monitoring, a higher frequency of testing was performed at the beginning and was reduced throughout the experiment, as more stable conditions developed. Nevertheless, it can be said that at least three LPR measurements/week were carried at each flow rate condition during most of the tests durations.

$$j_{corr} = \frac{B}{R_p} \tag{51}$$

$$R_p = \left(\frac{\partial \varepsilon}{\partial j}\right)_{j=0, \ dE/dt \to 0} \tag{52}$$

$$B = \frac{b_a b_c}{2.303(b_a + b_c)} \tag{53}$$

$$CR_{LPR} = 3.27 \times 10^{-3} \frac{j_{corr} \ EW}{\rho} \tag{54}$$

The primary cause of inaccuracies associated with LPR is the use of an incorrect Stern-Geary factor (B). In an effort to minimise the inaccuracies, B was obtained from the slopes (b_a and b_c) derived from the final linear sweep voltammetry (LSV) at the end of the four months test at a FR/SS of 0.0008 ml.min^{-1}.cm^{-2}. Rogowska et al. (2016) observed B varying from 20 to 27 mV, based on results of weight loss.

The linear sweep voltammetry consists of sweeping the potential of the working electrode at several hundred millivolts more than those applied to the LPR technique. The broader range of the sweep facilitates the determination of accurate slopes (b_a and b_c) and corrosion rates. The LSV destroys the surface of the sample, and thus the analyses were only performed at the end of each experiment. The potential sweep ranged from –300 to +300 mV with respect to the OCP. The sweep was conducted at a scan rate of 1 mV/s (AMERICAN SOCIETY FOR METALS INTERNATIONAL, 2003; AMERICAN SOCIETY FOR TESTING AND MATERIALS, 2014a, 2014c; DENZINE; READING, 1997; PEREZ, 2004; ROBERGE, 2000; WOLYNEC, 2003).

3.3.6. Weight change techniques

Weight loss and weight gain are frequent and reliable methods used to obtain average corrosion rates and scales growth respectively. The measurements were carried out based on procedures described in the literature and ASTM G1-03 (AMERICAN SOCIETY FOR TESTING AND MATERIALS, 2003; SUN, 2006). A total of 46 tensile wires (70 mm x 12 mm x 5 mm) were weighed per test condition. The remaining samples were used for surface examination and electrochemical tests. As recommended by ASTM G1-03, repeated cycles of submersion in Clarke`s reagent were made to remove the corrosion scale (AMERICAN SOCIETY FOR TESTING AND MATERIALS, 2003).

The average corrosion rate (ACR) was obtained by equation 55 (in mm/y), or by equation 56 (in mol/(m²h)). The average scale growth (ASG) was calculated by equation 57 (in

mol/(m²h)). Note that ASG does not comprehend the scale adhered in the glass vessel. Sun (2006) shows that the incertainties related to the adherence of scale in the test vessel decrease when V/S becomes smaller. The term "m_1" is the initial weight of the coupon (g); "m_2" is the weight of coupon after the end of the test (g); "m_3" is the weight of coupon after complete removal of the corrosion scale (g). "MW_{FeCO3}" is the molecular weight of iron carbonate (g/mol). "t" is the time (hours). "S" is the surface area of the steel (m²). "ρ" is the density of the steel (kg/m³).

$$ACR = \frac{m_1 - m_3}{MW_{Fe} \times t \times S} \times \frac{365 \times 24 \times MW_{Fe}}{\rho} \tag{55}$$

$$ACR = \frac{m_1 - m_3}{MW_{Fe} \times t \times S} \tag{56}$$

$$ASG = \frac{m_2 - m_3}{MW_{FeCO_3} \times t \times S} \tag{57}$$

The preferential formation of $FeCO_3$ was assumed in equation 57, grounded by its dominance in similar CO_2 environments, which is supported by many authors (BARKER et al., 2018; DUGSTAD et al., 2015, 2018; HERNANDEZ; MUÑOZ; GENESCA, 2012; KE et al., 2017; NEŠIĆ, 2007; RUBIN et al., 2012; SUN, 2006; TANUPABRUNGSUN et al., 2012). A clear identification of the corrosion scale was carried by X-ray diffraction (XRD), improving the level of certainty of the weight gain results.

3.3.7. Statistical analysis

The statistical treatment performed in this work involved the collection and careful scrutinisation of quantitative data of ACR and ASG to obtain statistically relevant data.

3.3.7.1. Sample size

A choice of sample size for estimation is calculated from equation 58. The minimum sample size achieved for each experiment was 46 specimens, with a confidence level of 95%, a standard deviation of 0.005 mm/y and a margin of error of 0.0015 mm/y. While the margin of error (e) could be chosen by experience, the standard deviation (Sd) was estimated by the calculus of Sd from the data of average corrosion rates available in the work of Rubin, A. et al. (2012). Their dense packed experiment, with a V/S of 0.17 ml/cm², was carried over 1464 hours

in artificial seawater, deaerated overnight and saturated with carbon dioxide aqueous solution at 23 °C. Information in the literature to allow an estimation of Sd for weight gain concerning ASG was not found, so the sample size used in this work concerns the average corrosion rates only.

$$n = \left(\frac{Z_{\alpha/2}.Sd}{e}\right)^2 \qquad (58)$$

3.3.7.2. Outliers

Given the considerable number of samples and the complexity of the tests, the statistical analyses considered the possibility of outliers, defined by the abnormal distances from others in a random sample of a population. The methods to exclude the samples from the analysis was the Inter Quartile Range (IQR) and the modified Thompson Tau Test.

3.3.7.3. Tolerance interval

The tolerance interval provides a range of values of average corrosion rates and average scale growth that likely covers a proportion of the population. In other words, the tolerance specifies a proportion of the population at a specified confidence level. The calculation was performed using the software Minitab 17, which calculates the tolerance using either the Normal or Nonparametric Methods. The normal tolerance method is employed when the data follow a normal distribution, whereas the nonparametric tolerance method is used when the probability distribution is non-normal. The non-normal method is advantageous when the data cannot be transformed into normal by applying transformations functions, such as box-cox or Johnson transformations. Further details and equations used by the statistical software can be found in the software Minitab 17 or in the literature (CHOU; POLANSKY; MASON, 1998; DE MIRANDA, 2005; KRISHNAMOORTHY; MATHEW, 2009; ODEH, 1978; OLDONI; RIBEIRO; WERNER, 2015)

3.3.8. Scaling tendency

The thickness of the scale layer should not be interpreted as a definite indication of the protectiveness of the corrosion product, once the density and adhesion shall also be accounted.

Accordingly, a non-dimensional parameter called scaling tendency (ST) can be used to characterise the kinetics of the formation of scales in CO_2-corrosion (BARKER et al., 2018). ST is calculated by the ratio between ASG and ACR using the same molar units, equation 59. If ST exceeds a given critical value, the corrosion scale can be assumed as protective; otherwise, an unprotective film is likely to form. Figure 43 shows a guideline for the critical scaling tendencies as a function of microstructure and chemical composition of the steel (VAN HUNNIK; POTS; HENDRIKSEN, 1996). The plot does not comprehend the carbon content of the HSS used in this work. However, if the general trend is kept unaffected, it is reasonable to assume that the critical ST would tend to decrease to values below 90% by further increase of the carbon content.

$$ST = \frac{ASG}{ACR} \tag{59}$$

Figure 43: Critical scaling tendencies at which protective corrosion scale begins to form in CO_2-corrosion.
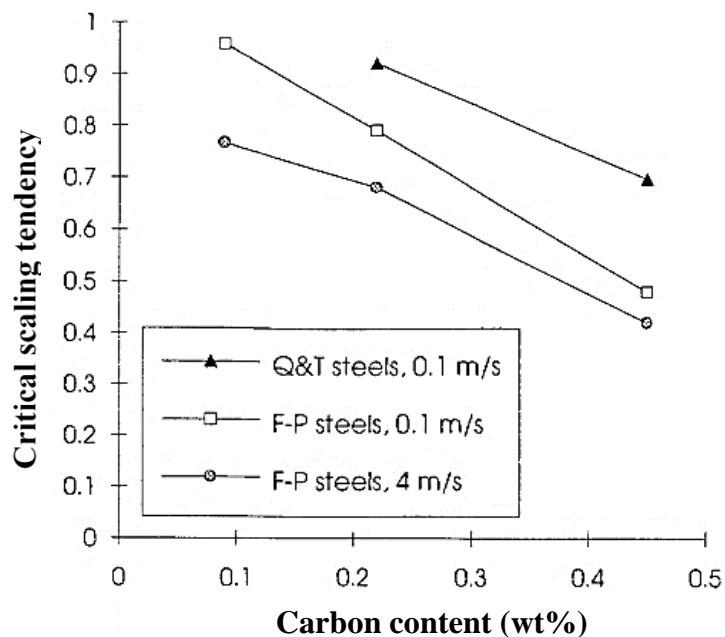
Source: Adapted from (VAN HUNNIK; POTS; HENDRIKSEN, 1996).

3.3.9. Characterisation of the corrosion surface

The corrosion surface of the HSS tensile wires was studied with light and scanning electron microscopy (SEM). A definitive characterisation of the corrosion product was obtained by X-ray diffraction (XRD) analysis.

3.4.   EFFECT OF THE ATMOSPHERIC VARIABLES

3.4.1. The effects of the atmospheric variables on CO_2-containing brines

Pressure and temperature in H_2O/CO_2 environments have been extensively explored over the years. Nevertheless, this subject remains vital to considerations regarding the initial states and compositions of the electrolytes confined in the annulus of unbounded flexible risers. Hence, hydrochemistry models were used to simulate the impact of the atmospheric variables on the properties and composition of a 3.5%wt. NaCl brine. A wide range of pressures and temperatures was proposed to cover liquid, gaseous and supercritical states of carbon dioxide (see Table 6). It is plausible that the tensile wires could be in contact to cold seawater in case of unrepaired failures at large depths, so the lowest temperature considered was 5 °C (SCRIPPS INSTITUTION OF OCEANOGRAPHY, 2013).

Table 6: Range of the variables considered to the simulation.

Pressure range (atm)	1– 90
Temperature range (°C)	5 – 90
Aqueous Solution composition	3.5%wt. NaCl
Aqueous Solution Volume @ 1 atm (L)	1.0
Aqueous Solution (mol)	55.9644
Gas phase/Mole fraction (%)	CO_2/100

3.4.2. Annulus environment – concentration of iron

The state and composition of the electrolyte are critical factors for the occluded CO_2-corrosion. Thus, simulations were carried to investigate a 3.5%wt. NaCl brine saturated with carbon dioxide and containing different amounts of iron. Table 7 shows the range of pressure and temperatures investigated. In each environmental combination, the concentration of iron in the solution was varied, covering the undersaturation, the saturation and the supersaturation domains of iron. The findings from this work and the literature were used as a criterion for the magnitudes and the likely consequences.

Hence, this section aims at searching for more critical corrosion patterns and on providing guidelines for further experimental annulus testing. It does not provide a holistic view of the corrosion process, as the flexible risers technology is young and unknown factors may exist. However, at this stage, it was impractical to consider a more extensive number of variables because additional and laborious laboratory investigations would be required.

Table 7: Matrix for the electrolyte simulation.

		Pressure [atm]			
		1	45	70	90
Temperature [°C]	5	✓	✓	✓	
	30	✓	✓	✓	
	60	✓	✓	✓	✓
	90	✓	✓	✓	✓

Phase - CO_2
Liquid
Gas
Supercritical

4.   RESULTS AND DISCUSSION

4.1.   CARBON DIOXIDE FLOW RATES

An analysis of the permeation of carbon dioxide in the typical polymer grades relevant to the structures employed in the field was carried to obtain a representative range of flow rates to be used in laboratory experiments. Table 8 shows the results of the permeation analyses, the flow rate per square cm of steel is presented for the different bore conditions.

Table 8: Results of the CO_2 permeation analyses.

No.	Press.	Temp.		Polymer Type	Surface per length	Permeation rate per surface of the steel
	bar/atm	Int.[°C]	Ext.[°C]	Inner sheath	cm^2/cm_{length}	$ml/min/cm^2$
1	800/790	80	10	A	531	0.00043
2	800/790	80	10	A	330	0.00034
3	800/790	80	10	B	531	0.00010
4	800/790	80	10	C	531	0.00376
5	300/296	60	5	C	531	0.00065

Based on the results, a wide range of flow rates could be employed in the laboratory experiments, given that the lowest permeation rate was 0.00010 $ml.min^{-1}.cm^{-2}$ (analysis N°. 3) and the highest was 0.00376 $ml.min^{-1}.cm^{-2}$ (analysis N°. 4). Comparing analysis N°. 3 and N°. 4, the simulation indicates that there is a significant difference between the permeation rates obtained for different polymers with the same bore conditions. Therefore, the analyses highlight the importance that the inner sheath plays in controlling carbon dioxide permeation into the annulus. Also, pressure, temperature and geometry of the pipe affected the permeation, where the combination of higher pressures and temperatures increased the carbon dioxide flow rate into the annulus as shown by a comparison between analysis N°. 4 and N°. 5.

4.2.   PROPERTIES OF THE OCCLUDED ELECTROLYTES

4.2.1.   Experimental evolutions of the occluded electrolyte

The concentration of iron ions was monitored regularly throughout the tests. Figure 44 shows the evolution of iron concentration (solid line) and pH (dotted line) over time, alongside the simulated saturation of iron in 3.5%wt. NaCl brine (horizontal dashed line). The achieved

simulated solubility limit of Fe^{2+} was 186 mg/l (3.34 mM), at 1 atmosphere of CO_2 and 30±2 °C. This value is close to values found in the literature (ROGOWSKA et al., 2016).

Figure 44: Concentration of iron ions in the solution over time. The saturation with iron ions was simulated under the environmental conditions tested in the laboratory. Test conditions: V/S of 0.2 ml/cm², 3.5%wt. NaCl brine, FR/SS of 0.0008 ml.min^{-1}.cm^{-2}, 1 atm of CO_2 and 30±2 °C.
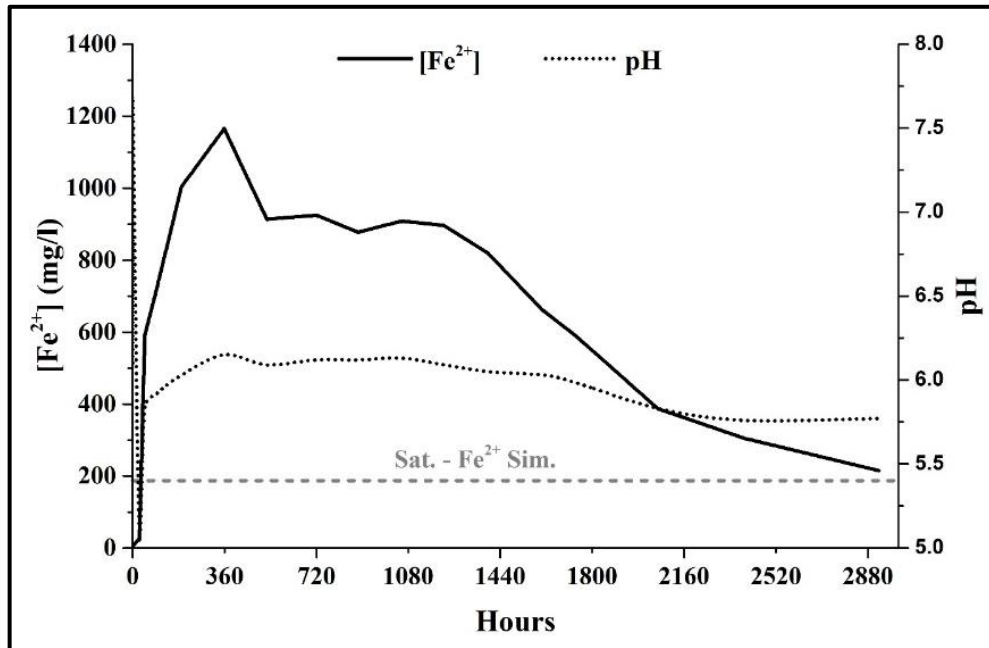
Source: AUTHOR.

The plot shows that the occluded environment is reasonably sensitive to the release of iron ions caused by the corrosive processes. Apart from the initial measurements (after nitrogen purging), no value below the calculated saturation of iron was measured. The solution remained supersaturated with iron for the test duration, revealing the slow kinetics of precipitation. Only at the end of the test does the iron concentration approach the steady-state at the saturation level predicted by simulation. The maximum concentration of iron measured was 1165.2 mg/l, observed after 359 hours, being around six times larger than the simulated saturation of iron in the 3.5%wt. NaCl brine. Such concentration with iron is comparable to the data presented in the literature (DUGSTAD et al., 2015, 2018; ROGOWSKA et al., 2016). The evolution of the pH shows small variations, but on the whole remained close to pH6 for most of the test period. The maximum value of pH6.15 was reached after 359 hours. The trends in pH mirrored the timescales for the evolution in dissolved iron.

The pH of water in 1 atmosphere of CO_2 is usually close to pH3.8. However, this was not observed. The pH remained more basic due to the presence of iron and carbonates in the

solution and the electrochemical corrosion process. Figure 45 shows the correlation between the concentration of iron and pH. The plot shows an increase in the pH as the concentration of iron increase, the trend is shown by the black arrow. The pH follows the concentration of iron as a direct consequence of the concentration of carbonates within the solution (DUGSTAD et al., 2015, 2018; KE et al., 2017; ROGOWSKA et al., 2016). According to Ke, et al. (2017) the pH of the solution changes with the reduction of H^+ (equation 29) and the release of iron ions and bicarbonate (see equation 60). Works in the literature suggest that the reduction of hydrogen is the dominant cathodic reaction in a mechanism called buffering effect, driving the hydrogen ions into gaseous $H_{2(g)}$, which can bubble out of the solution (ALMEIDA et al., 2017; THU; BROWN; NEŠIĆ, 2015). The release of electrons due to the dissolution of iron, therefore, disturbs the balance of the solution, removing hydrogen ions from solution and increasing the relative quantity of carbonates.

$$H^+ + e^- \leftrightarrow {}^1\!/\!_2\, H_{2(g)} \tag{29}$$

$$Fe + 2H_2CO_3 \rightarrow Fe^{2+} + 2HCO_3^- + H_2 \tag{60}$$
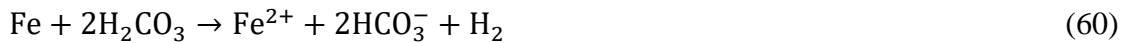
Figure 45: pH as a function of the iron concentration in the solution. Test conditions: V/S of 0.2 ml/cm², 3.5%wt. NaCl brine, FR/SS of 0.0008 ml.min^{-1}.cm^{-2}, 1 atm of CO_2 and 30±2 °C.
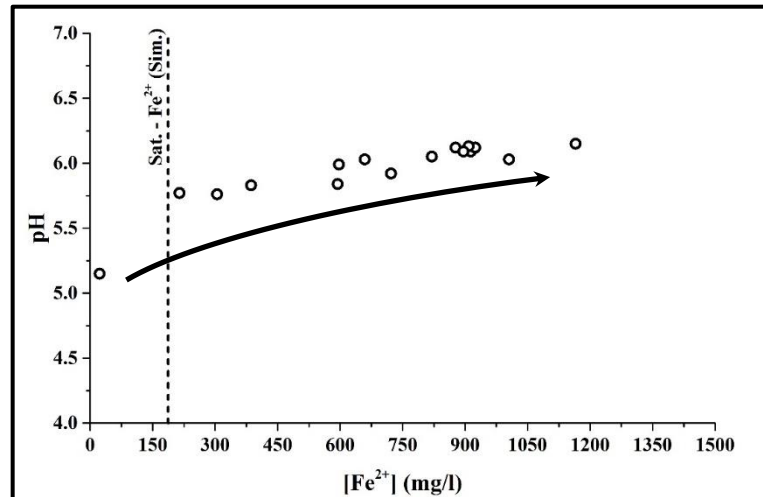
Source: AUTHOR.

4.2.2. Simulations of the occluded electrolyte

Understanding the differences between the available boundaries of H_2O/CO_2 systems is a fundamental step before the simulation of the occluded environment. The incorrect selection

of the interactions between the system and the neighbourhood yields misleading interpretations of the aggressiveness of the solution and formation of corrosion products. Thus, simulations of titration procedures were carried out to observe the main differences in the composition of brines concerning variations of pH. The procedure involves virtual additions of HCl and NaOH to cause variations in pH of a 3.5%wt. NaCl brine saturated with carbon dioxide. The pressure and the temperature of the solution were selected to match those used in the laboratory experiments. Furthermore, to observe the effect of the different boundaries on comparable scenarios, the initial DICs of the CO_2 saturated brines were kept identical for both scenarios.

Figure 46 shows the behaviour of an open aqueous carbonate system at atmospheric pressure. It can be observed that the DIC changes according to variations in the pH, but the concentration of carbonic acid remains constant. These trends result from the fact that open systems allow the exchange of matter with the neighbourhood, which is portrayed by the growth of the DIC (a mass balance). The growth of DIC results from the linear increase of the carbonates, while the concentration of carbonic acid remains constant as the solution becomes less acid. The content of carbonic acid remains unaltered because it is not a function of pH, only from pressure and temperature as predicted by Henry's law.

Figure 46: Simulation of a titration procedure for an open system composed of 3.5 %wt. NaCl solution saturated with carbon dioxide at 30 °C and 1 atmosphere. The shadow indicates a range of pH typical from a flooded annulus of unbounded flexible risers.
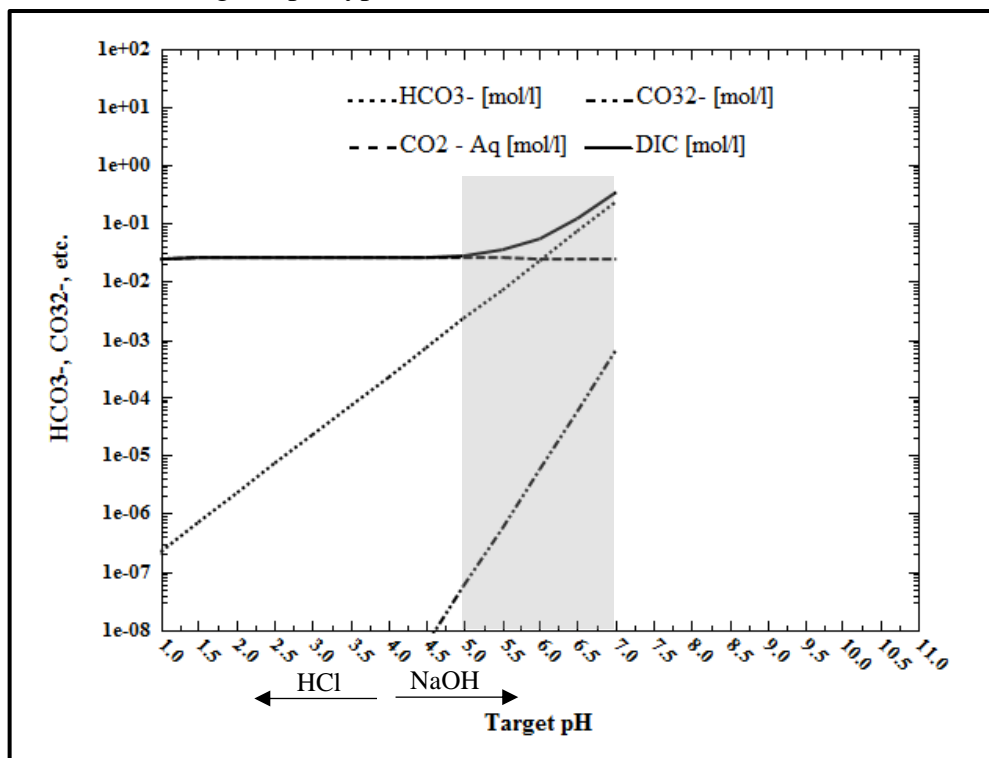
Source: AUTHOR.

The behaviour of the closed carbonate systems is shown in Figure 47. It contrasts to the open carbonate systems because the property remaining independent from the pH is the DIC, instead of the concentration of carbonic acid. Also, it can be observed that Henry's law does not sufficiently describe the concentration of carbonic acid at neutral and basic solutions because the constant DIC drives a decrease to the concentration of carbonic acid as the concentrations of carbonates grow. For the same reason, the carbonates cannot increase linearly, meaning that they tend to reach a maximum at given pH values and then drop to keep the mass balance constant.

Figure 47: Simulation of a titration procedure for a closed system composed of 3.5%wt. NaCl solution saturated with carbon dioxide at 30 °C and 1 atmosphere. The shadow indicates a range of pH typical from a flooded annulus of unbounded flexible risers.
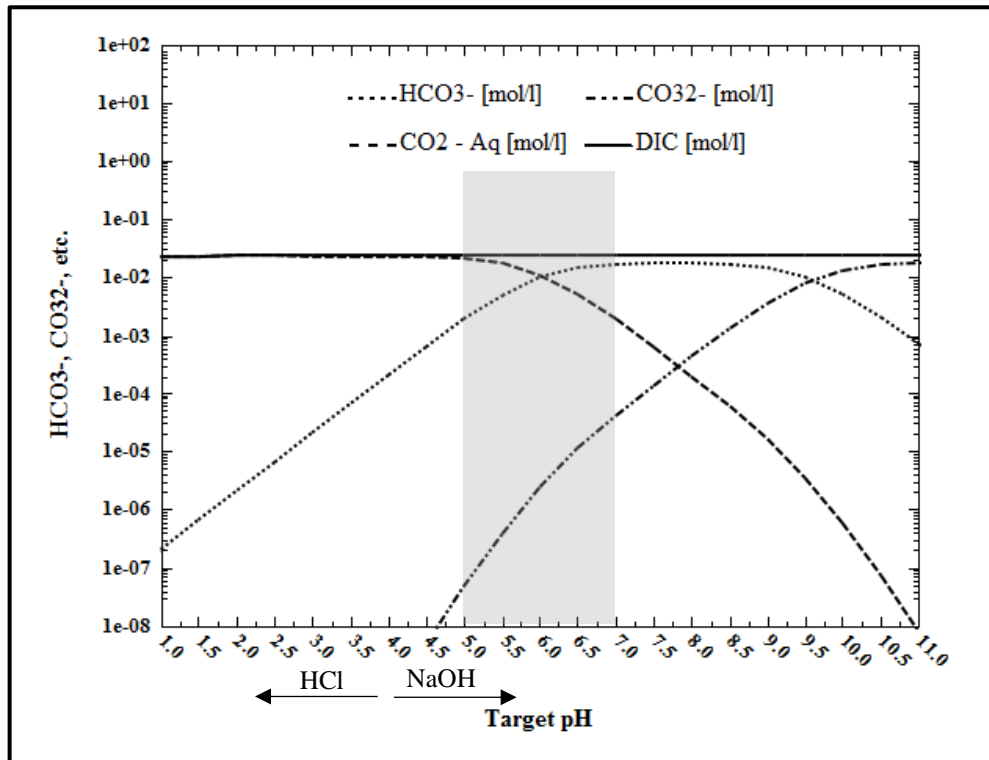
Source: AUTHOR.

Comparing both the simulations of the titrations, it is observed that the composition of the brine diverge on the interval of pH expected for the annulus environments - such contrast support that an analysis of the boundary of the specific carbonate system must be carried before further simulation. Following this statement, the relationship between pH and iron offers an opportunity to evaluate which thermodynamic boundary would suit better the laboratory experiments. Thus, Figure 48 shows simulations of the open and closed systems comparing the outcomes of the models to the experimental data obtained in the laboratory. Instead of showing

the data of the low flow rate experiment only, the pH and [Fe^{2+}] data from all laboratory experiments (N° 1 – low flow rate of CO_2; and N° 2 – high flow rate of CO_2) is shown. This was carried with the purpose of increasing the rigorosity and robustness of the analysis.

Figure 48: Comparison between open and closed carbonate systems.
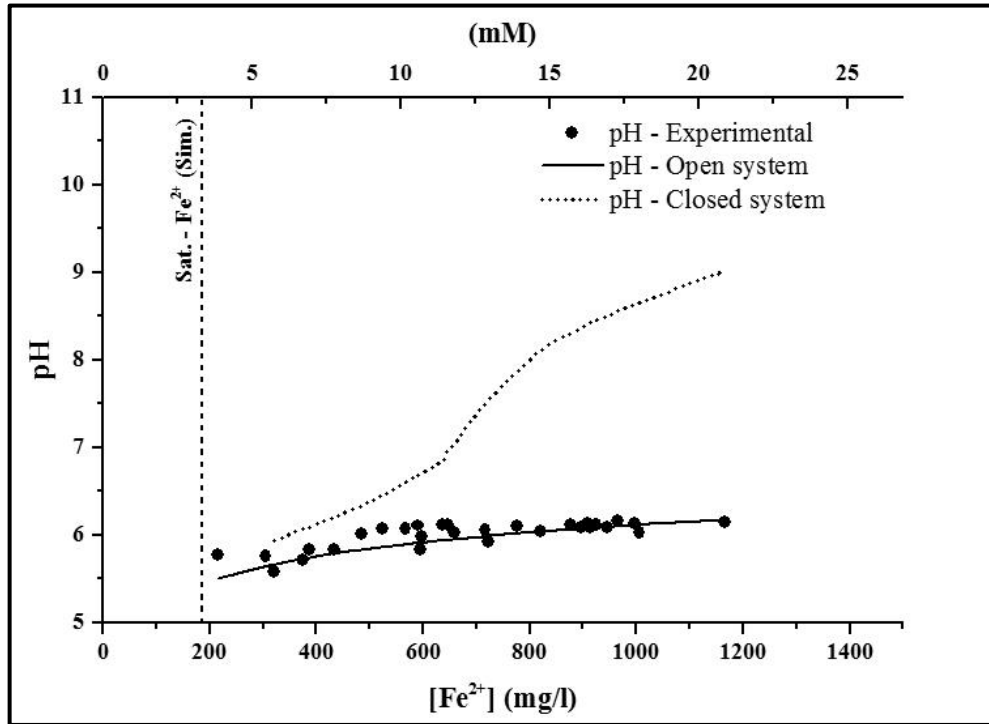
Source: AUTHOR.

The results show that the open carbonate system proves to be a better option for further simulations, as the simulated pH lies much closer to the experimental ones. Reflecting upon the underlying assumptions and interactions between the system and neighbourhood, it seems that open carbonate systems indeed agree better to the process of permeation of carbon dioxide into the annulus of flexibles and, also, to the experimental setup used in the laboratory, since the molecules of carbon dioxide may enter and depart the occluded environment.

Following the statement that the open carbonate system could be a better option for further simulations, a broader view of the effect of the iron on the solution is seen in Figure 49. The plot comprises the domains of undersaturation, saturation and supersaturation of brines with iron at 30 °C, and saturated with carbon dioxide in 1 atmosphere. The results show increasing values of pH, HCO_3^- and CO_3^{2-} and $FeCO_3$ as the concentration of dissolved iron increase. The concentration of carbonic acid remained constant and defined by the maximum solubility of carbon dioxide regarding the pressure and temperature, and so was not shown.

Figure 49: Simulation of the composition of the brine as a function of the concentration of Fe^{2+}. a) pH. b) HCO_3^-. c) CO_3^{2-}. d) $CO_{2(aq)}$. e) $FeCO_3$. The solution consists of 3.5%wt. NaCl brine saturated with carbon dioxide at 30 °C and 1 atmosphere.
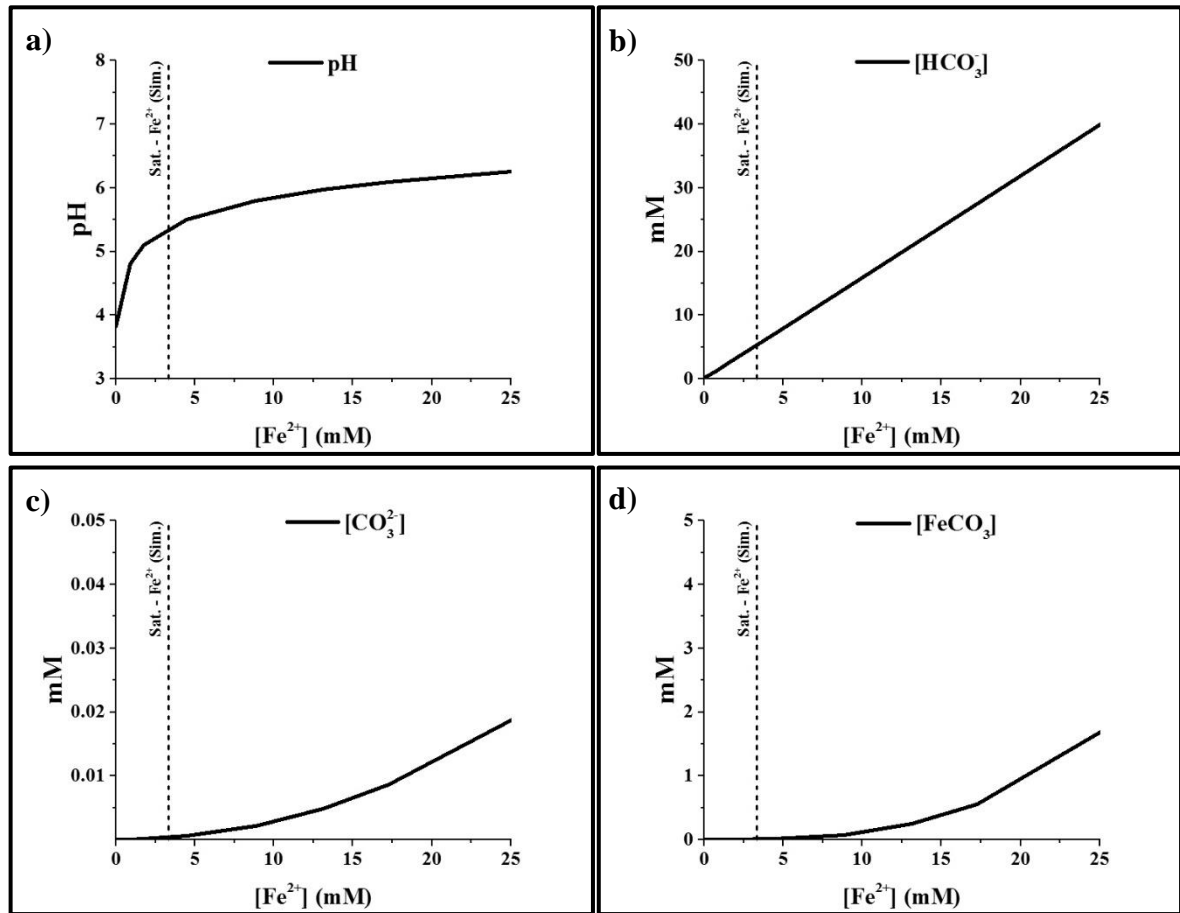
The experimental evolution of the pH was reproduced through simulation based on the experimental data of $[Fe^{2+}]$. Figure 50 reveals the good agreement between the experiment and simulation, presenting minor uncertainties. Nonetheless, it is reasonable to assume that the nature of the existing the uncertainty lies on the influence of factors such as the modelling strategies; the accuracy of the databanks; the accuracy range of the pH probe or small temperature differences that are inherent of the measurement steps.

Figure 50: Simulation and experimental evolution of pH at 3.5% NaCl brine at 30 °C, 1 atm of CO_2 and flow rate of 0.0008 $ml.min^{-1}.cm^{-2}$.
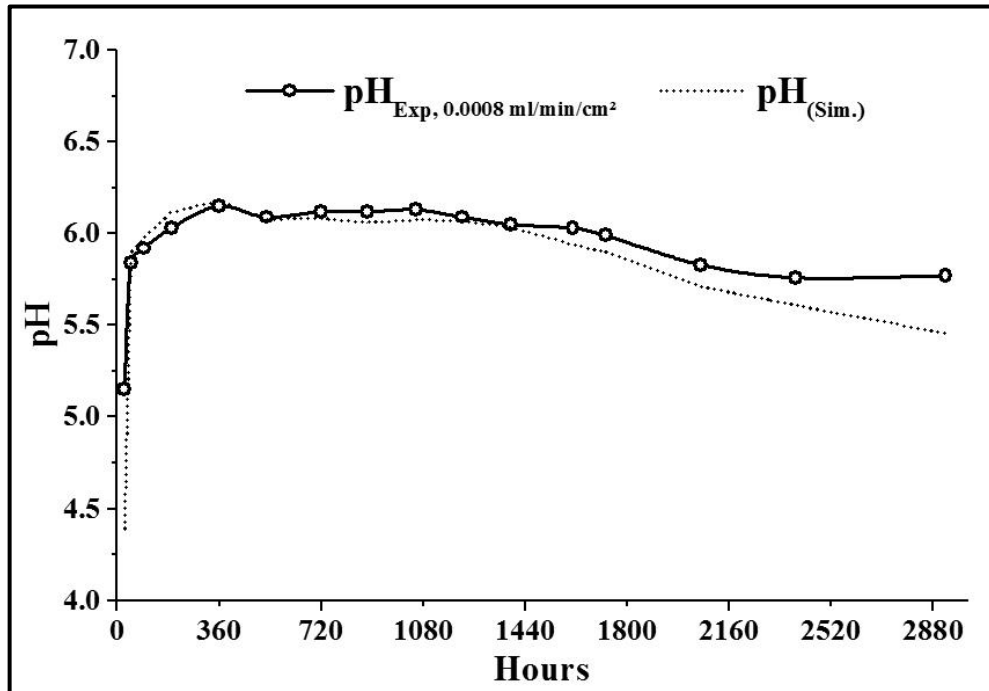
Source: AUTHOR.

4.3.   ELECTROCHEMICAL MONITORING

4.3.1.   Open circuit potential (OCP)

The open circuit potentials of the working electrodes were monitored over time. Figure 51 shows the evolution of the OCPs with time. It is seen an initial stage where the OCP of the working electrodes decreases over the first 500 hrs. Then, the OCP increase in a second stage, moving towards more noble values. In a third stage, the OCP drop off to a plateau of approximately -580mV, in the same period over which the pH and iron concentration stabilised, as shown in the previous sections. In other words, the evolution of OCP can be divided into three stages: I - an initial reduction over the first hours; II - a dwell at less noble values and a shift towards more noble values; III – steady state at nobler OCP.

Figure 51: Evolution of the OCPs of working electrodes in the aqueous CO_2 atmosphere at 30 °C and 1 atm, with a FR/SS of 0.0008 ml.min^{-1}.cm^{-2}.
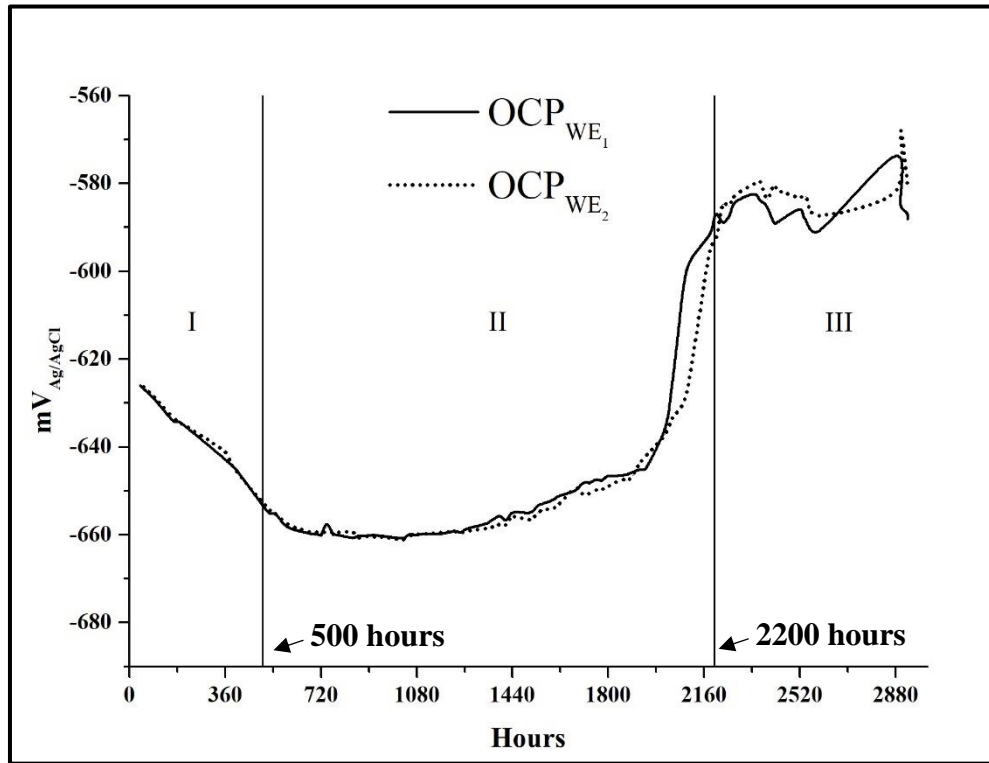
Source: AUTHOR.

Figure 52 shows the experimental moving average of the OCP as a function of time, alongside the evolution of iron and pH. To replicate the variations of OCP, equation 61 was used to fit the data. The fitting performed is experimental in nature and should not be taken as a direct application of Nernst equation, which is constrained to use in reversible systems. The terms "E'$_{I,II,III}$" are reduction potentials regarding the particular stages of the steel surface; "T" is the temperature; "n" is number of electrons exchanged; "R" is the gas constant; "F" is the Faraday's constant; and "[CO_3^{2-}]" is the concentration of carbonate. The E'$_{I,II,III}$ parameters can be understood as analogous to the standard electrode potentials (E^0), typically employed in the Nernst equation. The difference between these potentials would lie on the conditions of the system being studied in this work that are far from the standard case. E'$_{I,II,III}$ were obtained empirically, value that corresponds to the best fitting, and can be found in Table 9. Furthermore, it is assumed that equation 61 concerns the electro-crystallisation reaction (equation 44), involving the iron oxidation and the formation of $FeCO_3$ via one stage reaction with carbonate, which finds support in the literature (AZOULAY, 2013; BARKER et al., 2018; DUGSTAD et al., 2018; SK et al., 2017). Although [CO_3^{2-}] was not directly measured, the specific values could be inferred from the measured Fe^{2+} at the time of interest. All of the concentrations of carbonates assumed in Figure 52 are shown in Figure 53.

$$E = E'_{I,II,III} - \frac{2.303RT}{nF} \times \log[CO_3^{2-}] \tag{61}$$

$$Fe_{(s)} + CO_{3(aq)}^{-2} \leftrightarrow FeCO_{3(s)} + 2e^- \tag{44}$$

Figure 52: Evolution of the measured and analytical OCP, iron concentration and pH. The plot shows 3 zones, described by Roman numerals "I", "II" and "III". Test conditions: V/S of 0.2 ml/cm², 3.5%wt. NaCl brine, FR/SS of 0.0008 ml.min^{-1}.cm^{-2}, 1 atm of CO_2 and 30±2 °C.
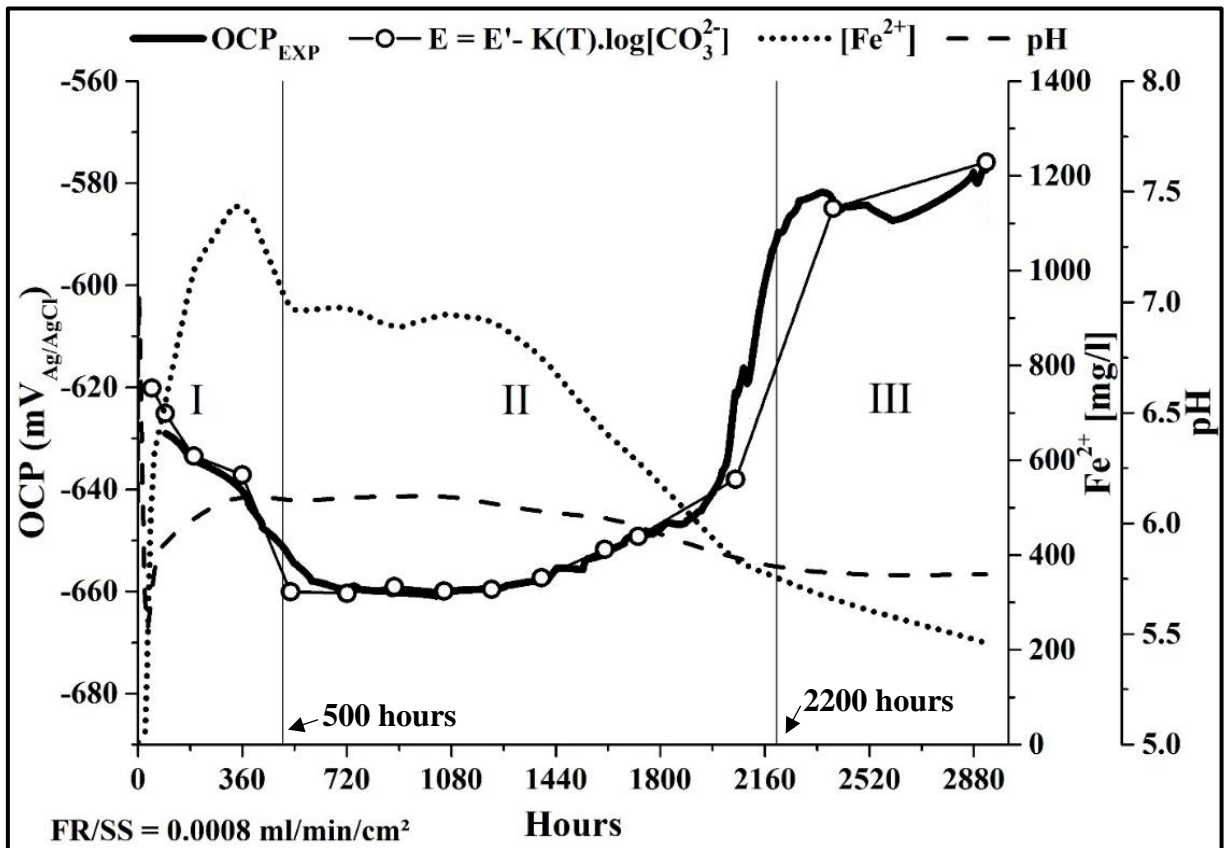
Source: AUTHOR.

Figure 53: Simulation of $[CO_3^{2-}]$ inferred from the measured Fe^{2+}. The modelled electrolyte consists of 3.5%wt. NaCl brine saturated with carbon dioxide at 30 °C and 1 atmosphere.
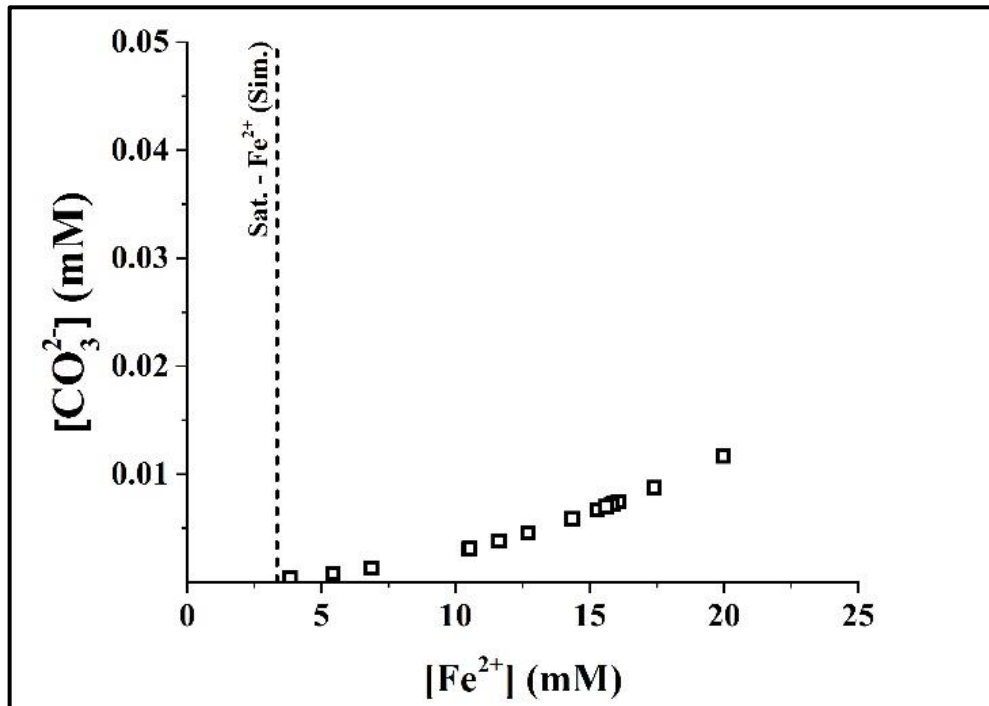
Source: AUTHOR.

Table 9: E'$_{I,II,III}$ constants respective to the three stages of OCP.

FR/SS [ml.min^{-1}.cm^{-2}]	E$_I$' [V$_{Ag/AgCl}$]	E$_{II}$' [V$_{Ag/AgCl}$]	E$_{III}$' [V$_{Ag/AgCl}$]
0.0008	-0.578	-0.607	-0.560

Comparing the experimental moving average OCP with the analytical value, it is observed that the first is well described by the latter at all stages. This observation supports the hypothesis that the change in the OCP is a function of iron dissolved in the solution, which in turn affects the carbonate balance of the system. The transitions of E' are not easily explained. However, the variations in pH or the adhesion of $FeCO_3$ in the surface could play important roles. In other words, the variations in pH may affect E'$_{I,II,III}$ through disturbing the electrochemical reactions. Thus, at the start, the pH of the solution is more acid so the E'$_I$ would be more positive, as also observed by the effect of pH in usual Evans diagrams. Similarly, as the pH increases the E'$_{II}$ should become more negative. The coverage of the surface with protective scales could also affect E' because the layers of corrosion product may change the oxidation tendency of the metal, perhaps explaining the later stage behaviour observed. Moreover, temperature variations could also affect the OCP by changing the slope of equation 61 and by disturbing the solubility of chemical species, including carbonates and carbonic acid.

This last relationship was not clear in this work because of the steady temperature control but may be significant for further testing in larger scales, whose temperatures could fluctuate more.

4.3.2. Linear polarisation resistance (LPR)

The LPR technique provides data of corrosion rate and polarization resistance. It is known that the corrosion rate data may carry inaccuracies associated with incorrect Stern-Geary factors (B). Consequently, the ideal discussion would be focused in the data of polarization resistance, since it is independent of B or corrosion rate. Yet, the literature often supresses the results of the polarisation resistance, favouring analysis on the corrosion rate. Then, to favour comparison with the literature, most of the results and discussion within this work, focus on the corrosion rate data with a clear description of variables used for the calculus of CR_{LPR}.

Figure 54 shows the corrosion rates and the polarisation resistance of the two working electrodes in the long-term, low flow rate test. The plot demonstrates two corrosion peaks separated by approximately one month. The variation of the peak corrosion rate for the two electrodes in the same system likely occurs due to specifics of the surface area of each. Surface imperfections and differences regarding roughness, residual stresses, or geometry of the surface are long known factors to cause uncertainties in corrosion tests. The studies of Ko et al. (2015) and Barker et al. (2018) support this statement. Ko et al. (2015) testified an immediate increase in current density upon application of an anodic potential in a rough surface mild steel, but an induction time before the current increased in a sample with a smoother surface. Barker et al. (2018) stated that the nucleation and growth of $FeCO_3$ crystals in rough surfaces are faster than in smooth samples. As mentioned in a previous section, the corrosion rates consider a B of 36.7 mV/dec, b_a of 0.218 V/dec and a b_c of 0.138 V/dec. However, if the b_a considered is equal to the value reported in the literature for the anodic dissolution of iron, that is ~ 28 mV/dec (KAHYARIAN; BROWN; NEŠIĆ, 2018), the B resultant would be 10.1 mV/dec. Accordingly, the corrosion rates shown in Figure 54 would decrease about 72% of the value shown in the plot, although the overall shape of the curve remains independent of the B.

Figure 54: Evolution of the LPR corrosion rate and polarisation resistance (Rp). Test conditions: V/S of 0.2 ml/cm², B of 36.7 mV/dec, 3.5%wt. NaCl brine, FR/SS of 0.0008 ml.min^{-1}.cm^{-2}, 1 atm of CO_2 and 30±2 °C.
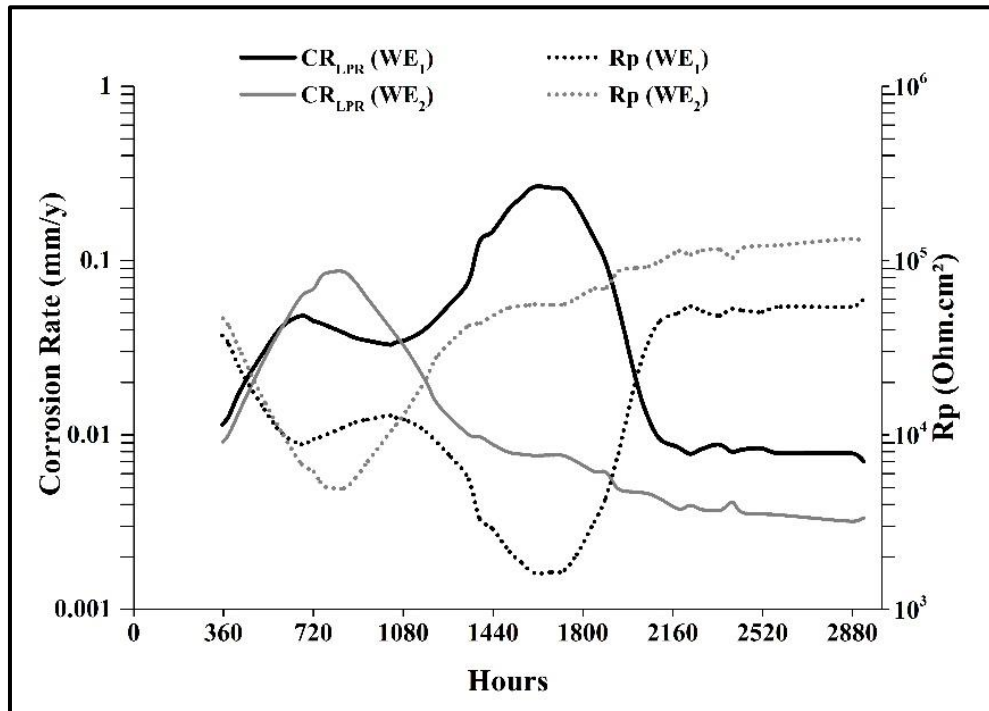
Source: AUTHOR.

The variations of the polarisation resistance reflect the changes on the interaction between the surface of the steel and electrolyte. The minimum Rp was 1612.3 Ohm.cm², whereas the maximum was 133239.6 Ohm.cm² after the plateau was established. The Rp changed significantly over time highlighting the evolution of the system during the experiment but remained close to the envelope reported in the work of Ropital et al. (2000) that ranged from 480 to 80300 Ohm.cm² after long-term experiments in confined environments at 20 °C and 1 atmosphere of carbon dioxide.

Figure 55 shows a summary plot of the average corrosion rates (CR_{LPR}) between the two working electrodes (WE_1 and WE_2), the average OCP, together with attributes of the electrolyte (pH and Fe^{2+}) throughout the experiments, for the low flow rate regime. The plot demonstrates the three different stages already highlighted in the OCP analysis, but this time also reflected upon the rise and fall of the corrosion rate. In the first stage, between 0 and ~500 hours, the corrosion rates increase with the growing oxidation tendency of the surface - as the open circuit potentials (OCP) become more negative. In turn, the oxidation reaction releases iron in the solution, increasing the super-saturation, that works as a driving force for the precipitation of iron carbonate. Hence, it is reasonable to expect an overall intensification on the precipitation rate during the first stage (BARKER et al., 2018; ROGOWSKA et al., 2016;

SUN, 2006). The second stage is shown in Figure 55 between ~500 and ~2200 hours. It represents the period of intense generation of iron ions (by corrosion) and intense consumption of iron ions (by precipitation). During this stage, the corrosion rate, the OCP, the pH and the composition of the solution are affected by the trade-off between driving forces. Once precipitation dominates, the concentration of Fe^{2+} drops and the OCP begins to shift towards more noble values in line with trends shown in the literature (BARKER et al., 2018; DUGSTAD et al., 2018; HAN et al., 2007; ROGOWSKA et al., 2016; TANUPABRUNGSUN et al., 2012). As a result, the corrosion process becomes less favourable, and the corrosion rates decrease over time. Moreover, the fall of the iron concentration will reduce the level of super-saturation, and so the associated growth of surface scales. In the third stage, observed after roughly 2200 hours, is characterised by low corrosion rates, stable OCP at the shift towards nobler values, stable pH and low concentration of iron ions in solution. These characteristics indicate that a near steady state has been reached.

Figure 55: Evolution of the LPR corrosion rate, OCP, pH and Fe^{2+}. Test conditions: V/S of 0.2 ml/cm², B of 36.7 mV/dec, 3.5%wt. NaCl brine, FR/SS of 0.0008 ml.min^{-1}.cm^{-2}, 1 atm of CO_2 and 30±2 °C.

Source: AUTHOR.

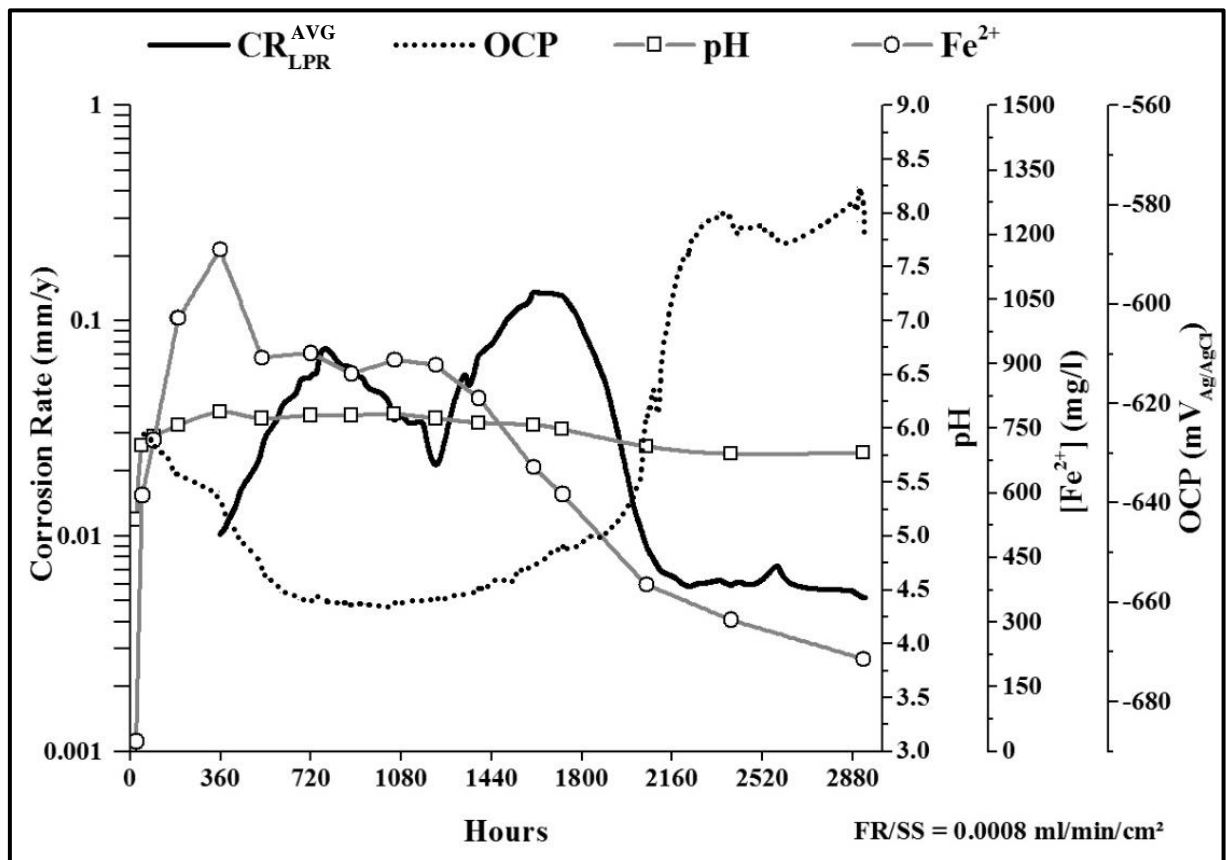Comparing the trends in corrosion rates with those reported in the literature, there are some differences to note. Clements (2008) shows corrosion rates that start at higher values, during the initial stages of the experiment and decay with time. It is likely that the difference between behaviours is the result of the different deaeration processes employed. Previous studies of the annulus corrosion process were carried out in solutions that were deaerated with carbon dioxide or that contained acid buffers. As a result, it is reasonable to assume that the concentrations of carbonic acid of these solutions were high from the beginning. Thus, such experiments begin with relatively aggressive environments and high initial corrosion rates that decrease over time as iron dissolves into the solution and as a protective scale forms. In the present case, deaeration was carried out with nitrogen, and the carbonic acid only begins to form, once the experiment has started, i.e. a less aggressive starting condition, closer to the reality of a flexible in service.

4.3.3. Linear sweep voltammetry (LSV)

The linear sweep voltammetry (LSV) is used to measure the absolute corrosion rates and properties of the surface of the steel. Figure 56 and Table 10 show the results of the LSV analysis. The results show mild corrosion rates and B that agrees with the literature (ROGOWSKA et al., 2016), though b_a seems larger than could be expected in case of active dissolution of iron in CO_2 containing environments. Kahyarian; Brown; Nešić (2018) performed corrosion tests in API X65 steel in CO_2-containing solution at 30 °C and observed that the b_a from the stage of active dissolution should range between 0.030 to 0.040 V/dec in respect to the pH. However, the stage before passivation, named pre-passivation, the apparent slope is around 0.120 V/dec. Therefore, the relatively large b_a point toward the build-up of a protective scale. From the works of Hernandez; Muñoz; Genesca, (2012) and Kahyarian; Brown; Nešić, (2018) it is possible to expect that the cathodic branch would show a mass-controlled mechanism. Despite that, the mass-controlled behaviour is not clear, and further work should be carried to understand such phenomenon. Nevertheless, Hernandez; Muñoz; Genesca, (2012) conducted LSV using a rotating electrode setup, observed b_c ranging from 0.120 to 0.153 V/dec, meaning that the data obtained in this work is consistent to the literature.

Figure 56: Plot of the linear sweep voltammetry at test end. Test conditions: 1 mV/s, V/S of 0.2 ml/cm², 3.5%wt. NaCl brine, FR/SS of 0.0008 ml.min^{-1}.cm^{-2}, 1 atm of CO_2 and 30±2 °C.
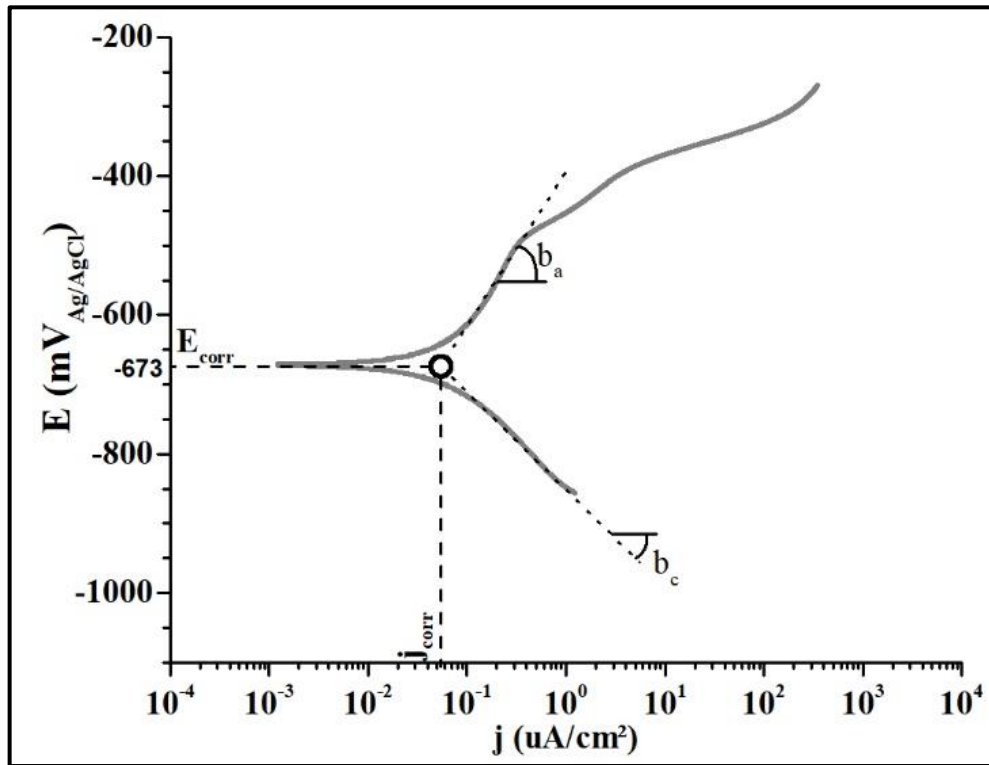
Source: AUTHOR.

Table 10: Results of the linear sweep voltammetry at test end. Test conditions: V/S of 0.2 ml/cm², 3.5%wt. NaCl brine, FR/SS of 0.0008 ml.min^{-1}.cm^{-2}, 1 atm of CO_2 and 30±2 °C.

FR/SS [ml/min/cm²]	E_{corr} [VAg/AgCl]	j_{corr} [A/cm²]	CR_{LSV} [mm/y]	b_a [V/dec]	b_c [V/dec]	B [mV/dec]	Time [months]
0.0008	-0.673	5.4E-08	0.0006	0.218	0.138	36.7	4

Figure 57 was adapted from the study of Remita et al. (2008), relevant to annulus environments. The plot compares the experimental CR_{LSV} to their predictions of the annulus. The model is of interest because it introduces the variable θ, which is related to the coverage of the surface by a protective scale (e.g. $FeCO_3$) or grease. According to the authors, a fully covered surface (θ = 1) implies that the thermodynamic equilibrium has been reached. When θ is equal to 0, the surface of the steel is active. Interestingly, their model seems to fit very well the CR_{LSV} when θ is equal to 0.99, which agrees to the growth of a protective scale and the achievement of the steady state that was mentioned in the previous sections.

Figure 57: Comparison of the corrosion rates obtained by LSV to results described in the literature at different degrees of occlusion.
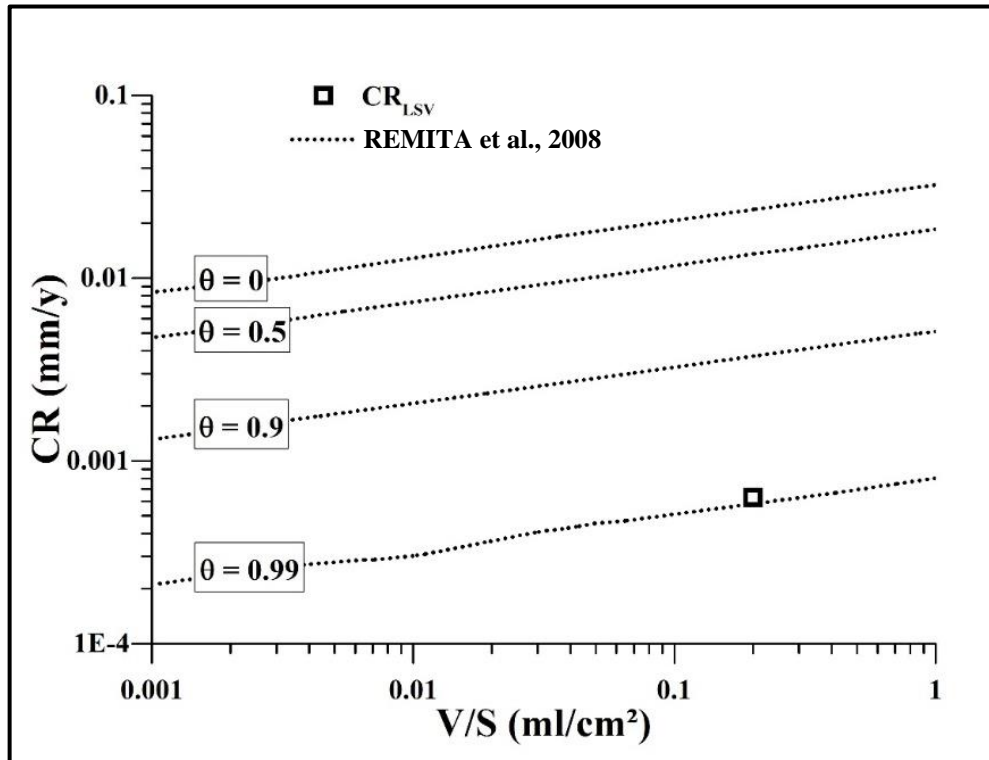
Source: AUTHOR and data extracted from (REMITA et al., 2008).

4.4.   WEIGHT CHANGE TECHNIQUES

4.4.1.   Average corrosion rates and average scale growth

Weight change methods provide average values of corrosion rate and scale growth respective to the total duration of the experiments. The average corrosion rate (ACR) was calculated using equation 55, and the average scale growth (ASG) using equation 57. For the tolerance interval, it is assumed that 90% of the population have the ACR or ASG falling within the bounds of the tolerance interval with 95% confidence. The tolerance interval was calculated using the normal tolerance method, as the data distribution was normal. Outliers were detected and excluded from the weight change analysis. The abnormal values were attributed to practical issues or the sharing of corrosion products from neighbour samples. The results of the weight change analyses are shown in Table 11, presenting the mean values, the tolerances, the data distribution and the number of identification of the respective samples considered as outliers.

$$ACR = \frac{m_1 - m_3}{MW_{Fe} \times t \times S} \times \frac{365 \times 24 \times MW_{Fe}}{\rho} \qquad (55)$$

$$ASG = \frac{m_2 - m_3}{MW_{FeCO_3} \times t \times S} \qquad (57)$$

Table 11: Average corrosion rate (ACR) and average scale growth (ASG) of high strength steel tensile wires in 3.5%wt. NaCl, at 1 atm of CO_2 and 30±2 °C.

Test	ACR [mm/y]	Distribution	Outliers [Id. N°]	ASG [mol/(m²h)]	Outliers [Id. N°]	Distribution
FR/SS=0.0008 ml.min^{-1}.cm^{-2} (4 Months, 0.2 ml/cm²)	$0.0177\,^{0.0331}_{0.0023}$	Normal	04, 08, 14	$2.67E^{-04}\,^{3.51E^{-04}}_{1.83E^{-04}}$	02, 04, 08	Normal

The ACR observed was 0.0177 mm/y (2.84E-04 mol/(m²h)). Thought this value is relatively small, it is almost an order of magnitude larger than the value provided by the linear voltammetry analysis. The reason behind such a difference is that the ACR is an average value, whereas CR_{LSV} is an absolute value respective to the end of the test, meaning that the values are not comparable.

Moreover, although it is common to find the use of gravimetric measures in the literature (CLEMENTS, 2008; CLEMENTS; ETHRIDGE, 2003; DUGSTAD et al., 2018; RUBIN et al., 2012; UNDERWOOD, 2002), its use should be restricted to applications where the corrosion rate does not change considerably in time, since the average values does not describe the trends nor absolute values. Therefore, a better use of the ACR and ASG results is a determination of the scaling tendency (ST). The ST is a non-dimentional parameter based on the ratio between the ASG and the ACR in the same unit. It characterises the kinetics and the protectiveness of corrosion scales formed on the surface of the steel. In the long term low flow rate experiment the ST obtained was 0.938, which is close to the unity, meaning that the scale growth remained as important as the corrosion process. Note that if the overall trend of the critical ST shown in Figure 43 is kept, it can be assumed that the ST above 93% would be relatively higher than the critical value. Thus, the scale adhered in the surface is understood as protective. Besides that, the establishment of a steady state with low corrosion rates, as shown in the previous sections, also agrees with such an interpretation.

To observe the results in a wider context with relevant literature in the field, Figure 58 shows the results of ACR and CR_{LSV} alongside others digitally extracted from works published in similar conditions (filtered to temperature ranges from 20 to 30 °C in atmospheric pressures

consisting of pure CO_2). The literature data involves several test durations and different techniques to obtain corrosion rate, including weight loss, LPR and LSV. The plot reveals that the range of results obtained in this work has some overlap with the literature data (DUGSTAD et al., 2015; ROPITAL et al., 2000; RUBIN et al., 2012; SUN, 2006). Also, despite the significant differences in the occlusion ratios, the corrosion rates found in the work of Dugstad et al. (2015) were close regarding magnitudes. This similarity is explained by the high degrees of supersaturation with iron, similar to occluded systems, that was artificially induced by the authors. Such a comparison shed light on the importance of iron concentration on the study of the annulus environment.

Figure 58: Comparison of the corrosion rates to results described in the literature at different degrees of occlusion.
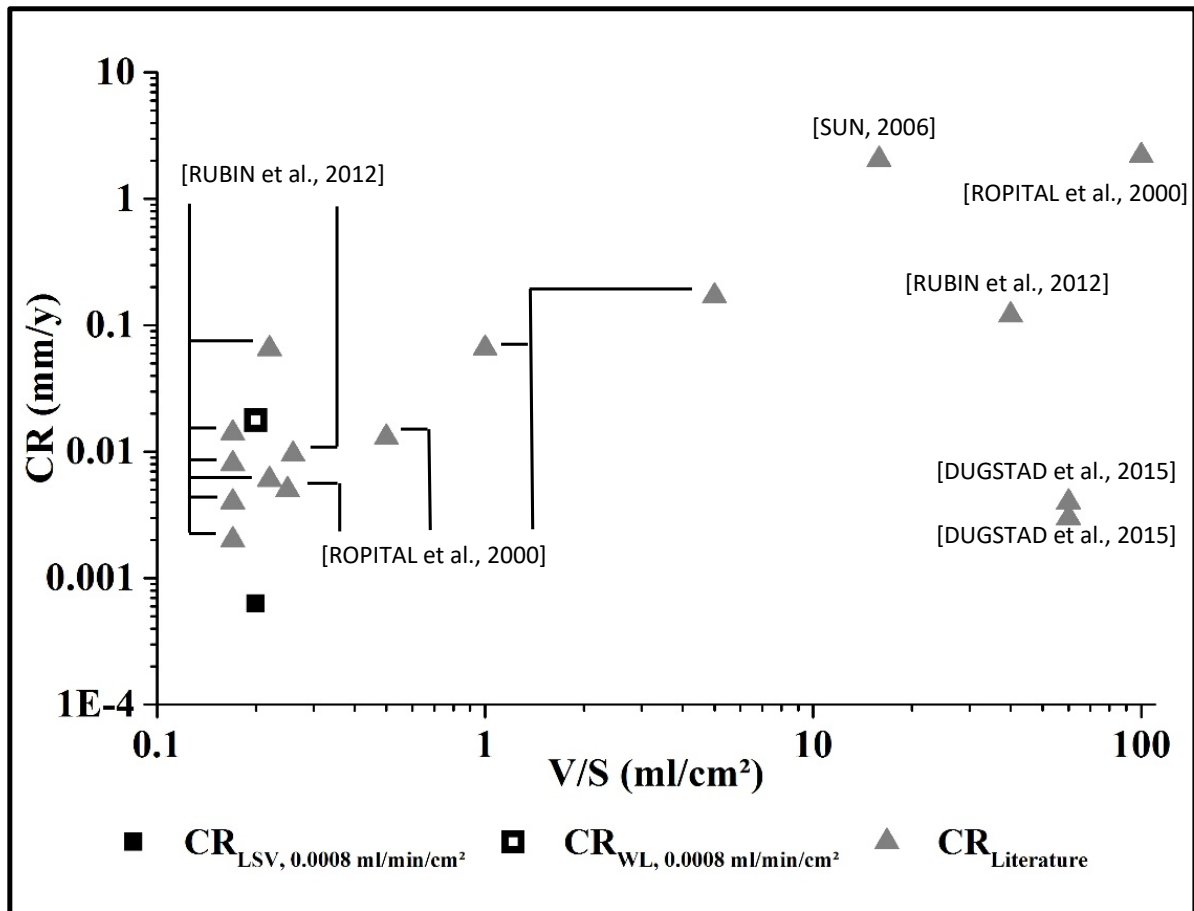
Source: AUTHOR and data extracted from (DUGSTAD et al., 2015; ROPITAL et al., 2000; RUBIN et al., 2012; SUN, 2006).

4.5. CORROSION SURFACE EXAMINATION

Figure 59 shows the most repeated surface appearances before and after the test. In many samples a uniform layer of scale was evident. Besides, no pitting or localised differences in corrosion that could not be linked to imperfections in the starting surface condition were identified. The experiment also produced a number of surfaces that displayed disruptions in the corrosion scales in the shape of bubbles, highlighted by the black arrows. It is understood that bubbles may form on the surface as a consequence of the hydrogen reduction reaction, or due to the high degree of occlusion that can induce mechanical trapping of CO_2 bubbles between neighbour samples.

Figure 59: Representative corrosion surface of the samples, demonstrating the specimens before and after the test. Test conditions: V/S of 0.2 ml/cm², 3.5%wt. NaCl brine, FR/SS of 0.0008 ml.min^{-1}.cm^{-2}, 1 atm of CO_2 and 30±2 °C.
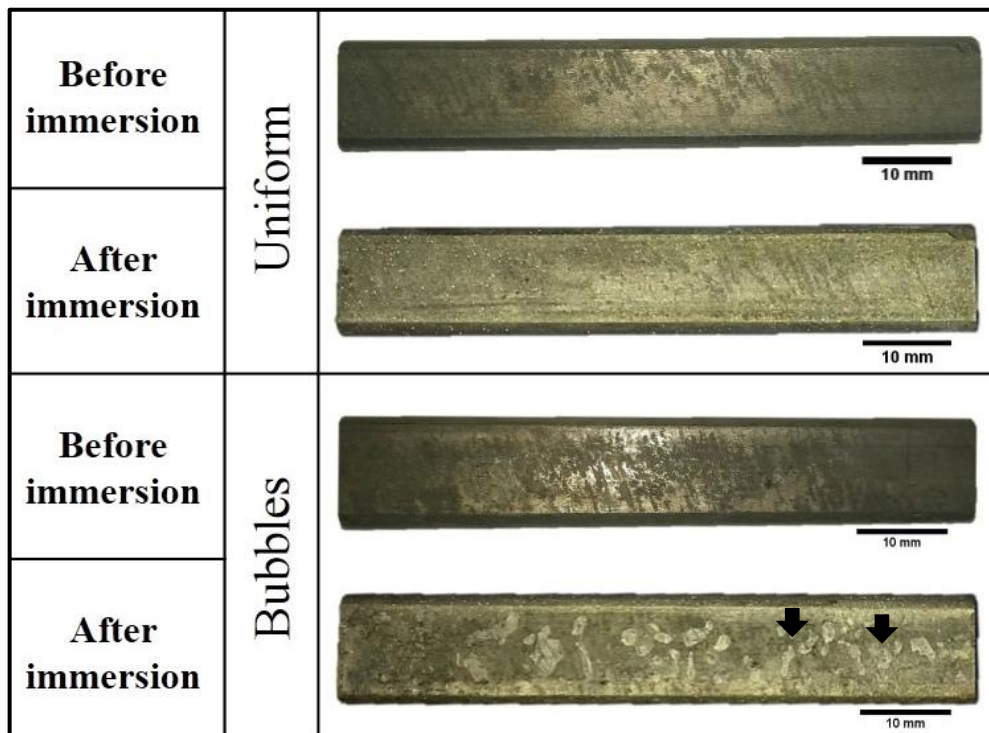
Source: AUTHOR.

The surfaces of the WE sample, whose potential was not swept by an LSV test, was observed before and after the four months in the solution (see Figure 60). The images taken by a light microscope immediately after the test vessel was opened show darkening of the surface with no apparent signs of localised corrosion. After a brief period in the open atmosphere, the dark corrosion products turned yellow.

Figure 60: Corrosion surface of the working electrodes before and after the test. Test conditions: V/S of 0.2 ml/cm², 3.5%wt. NaCl brine, FR/SS of 0.0008 ml.min^{-1}.cm^{-2}, 1 atm of CO_2 and 30±2 °C.
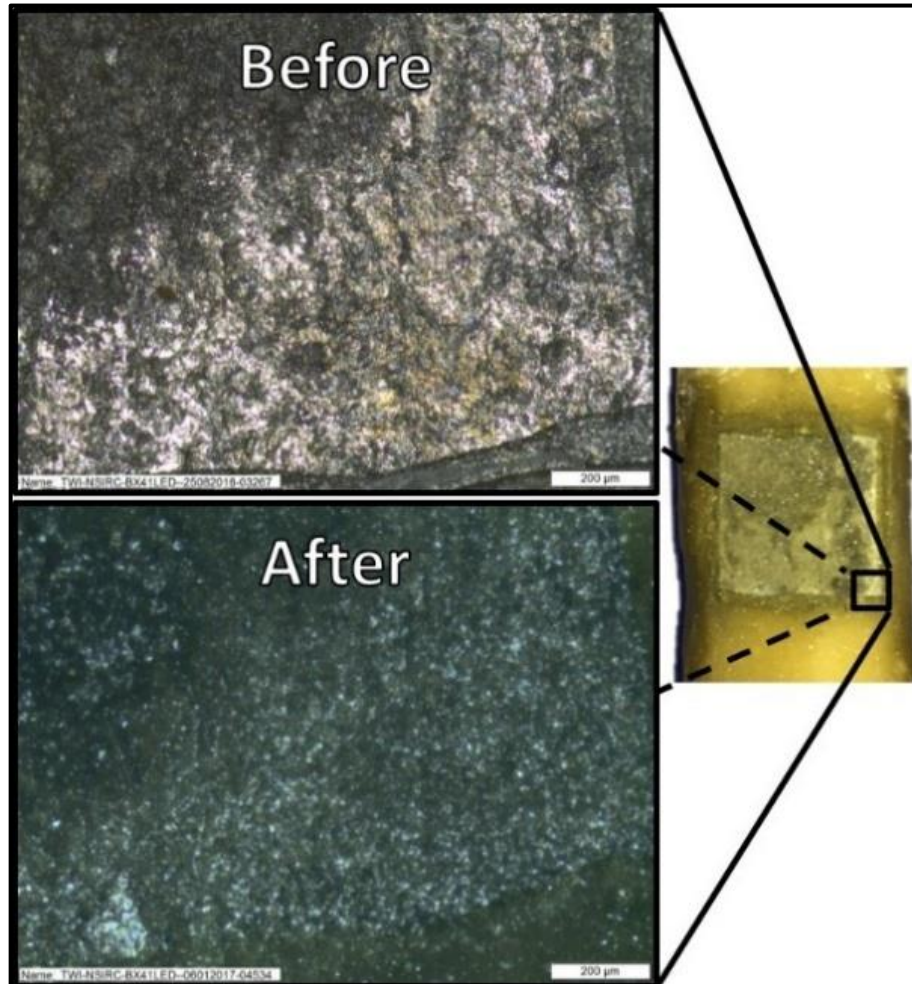
Source: AUTHOR.

Further investigations into the corrosion scales were carried out using SEM. Figure 61 shows the scale layer formed on the surface. The image reveals the presence of quite a uniform and dense scale on the surface of the samples, although the sample observed at low magnitude show a small zone of corrosion scales disrupted in the shape of bubbles. The dense coverage supports that the precipitation of corrosion products leads to the formation of an effective barrier that could reduce the rate of further corrosion once formed.

Figure 61: SEM images of corrosion scale formed after four months of testing. Top and bottom surfaces of the selected tensile wire are shown. Test conditions: 3.5%wt. NaCl, 1 atm of CO_2, FR/SS of 0.0008 ml.min^{-1}.cm^{-2} and 30±2 °C.
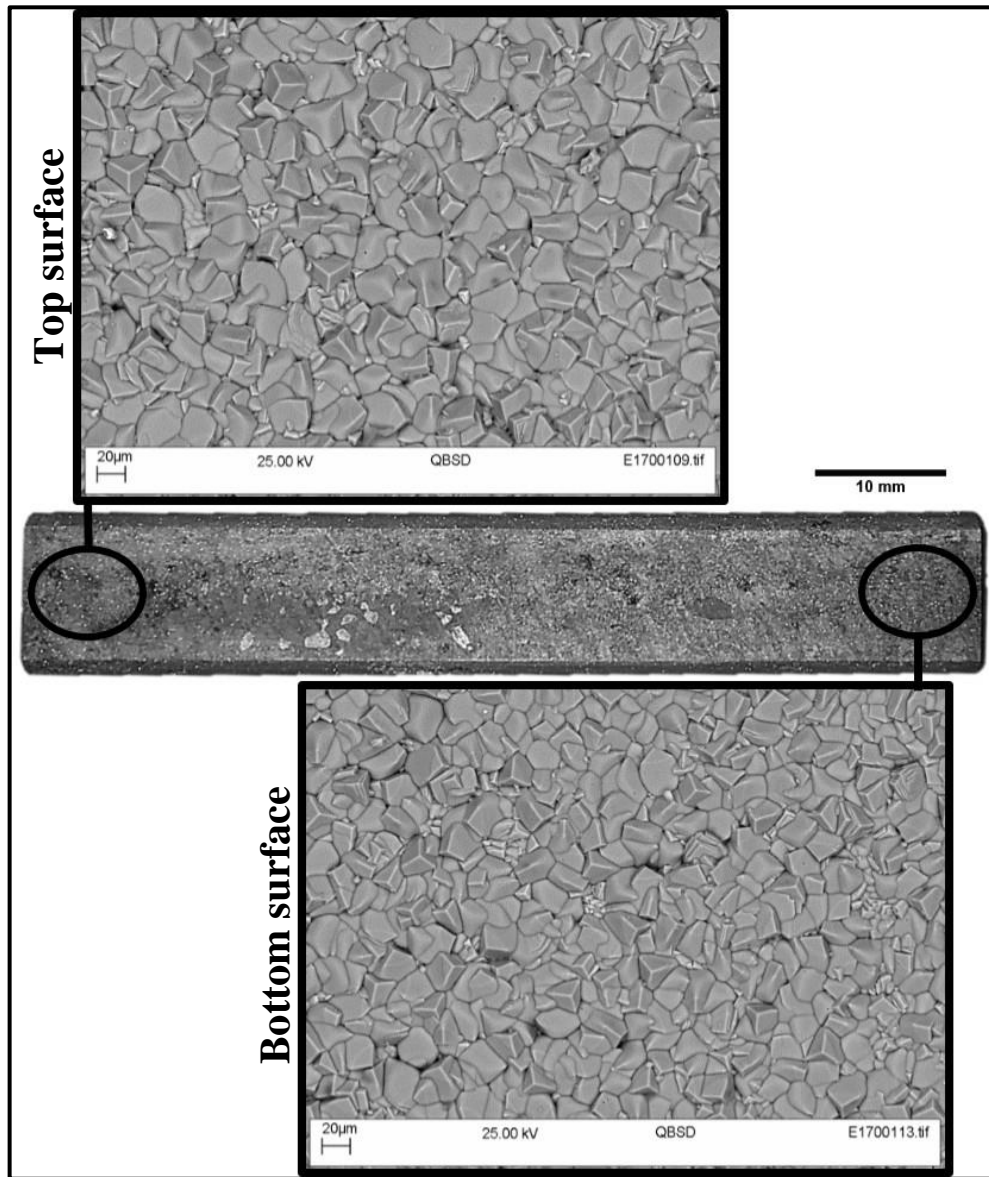
Source: AUTHOR.

A definitive characterisation of the corrosion scale is obtained by XRD analysis, shown in Figure 62, which demonstrates large peaks of $FeCO_3$. Note that such information also supports the usage of the term MW_{FeCO3} in equation 57, used to determine the average scale growth.

$$ASG = \frac{m_2 - m_3}{MW_{FeCO_3} \times t \times S} \tag{57}$$

Figure 62: XRD results confirming the presence of $FeCO_3$ on the surface of a sample after the test. Test conditions: 3.5%wt. NaCl, 1 atm of CO_2, FR/SS of 0.0008 ml.min^{-1}cm^{-2} and 30±2 °C.
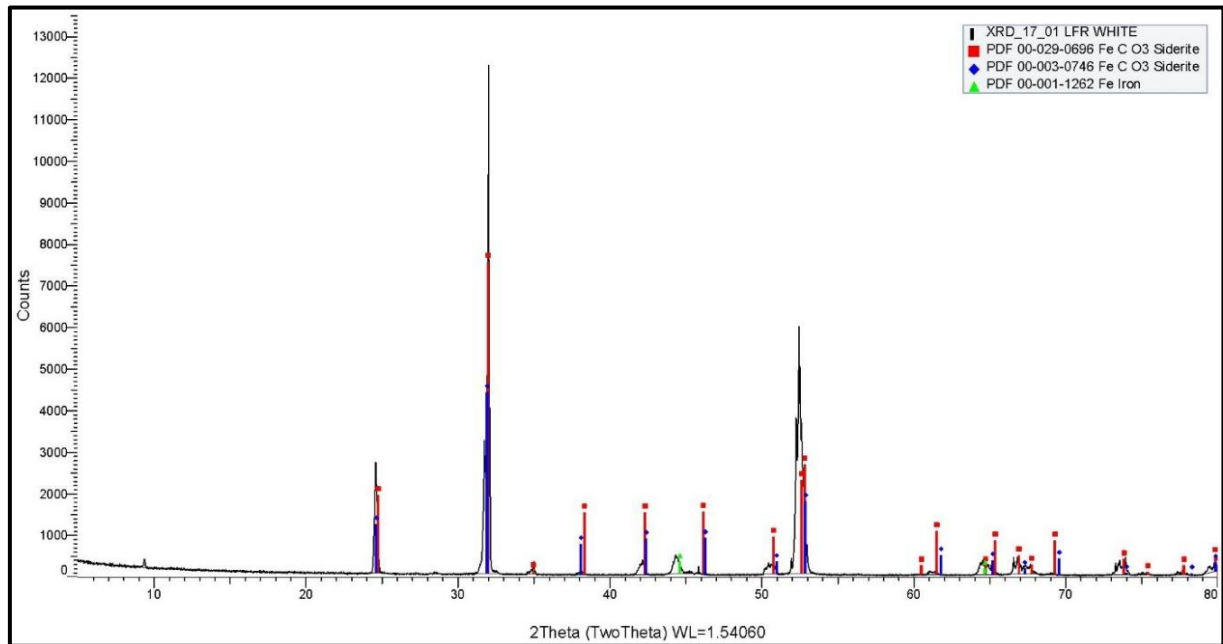
Source: AUTHOR.

4.6.   EFFECT OF THE FLOW RATE OF CO_2

Studies exploring the effect of flow rate on the risk of sulphide stress cracking in H_2S-containing environments identified that the restriction of flow rate could influence the steady state concentration of this aggressive species in the simulated annular conditions (DÉSAMAIS; TARAVEL-CONDAT, 2009; HAAHR et al., 2016). These assertions suggest that a restricted flux of CO_2 into a system may alter the steady state conditions and time that it takes for it to be established. This, in turn, may affect the corrosion rate of steel within it. Based on these considerations, an additional experiment was carried with a controlled high flow rate (two orders of magnitude larger) for two months, in order to study the influence of CO_2 flow rate on the corrosion of steel in annular environments. It is important to highlight that the high flow rate short-term experiment followed the same methodology and analyses as the others done in the low flow long-term experiment. The differences and similarities were explored regarding the evolution of iron and pH, the simulation characteristics, the electrochemical properties, the corrosion rates, the scale growth and the corrosion surface.

The evolution of the $[Fe^{2+}]$ from the experiments are compared in Figure 63. The results show similar maximum concentrations of iron in the solution; 1165.2 mg/l, for the test featuring the lower flow rate after 359 hours, and 996 mg/l for the test featuring the higher flow rate after 1363 hours in the brine. Despite the similar concentrations, a less rapid increase in the iron at the high flow rate experiment is seen.

Figure 63: Comparative of the concentration of iron ions in the solution over time. The saturation with iron ions was simulated under the environmental conditions tested in the laboratory. Test conditions: V/S of 0.2 ml/cm², 3.5%wt. NaCl brine, 1 atm of CO_2 and 30±2 °C.
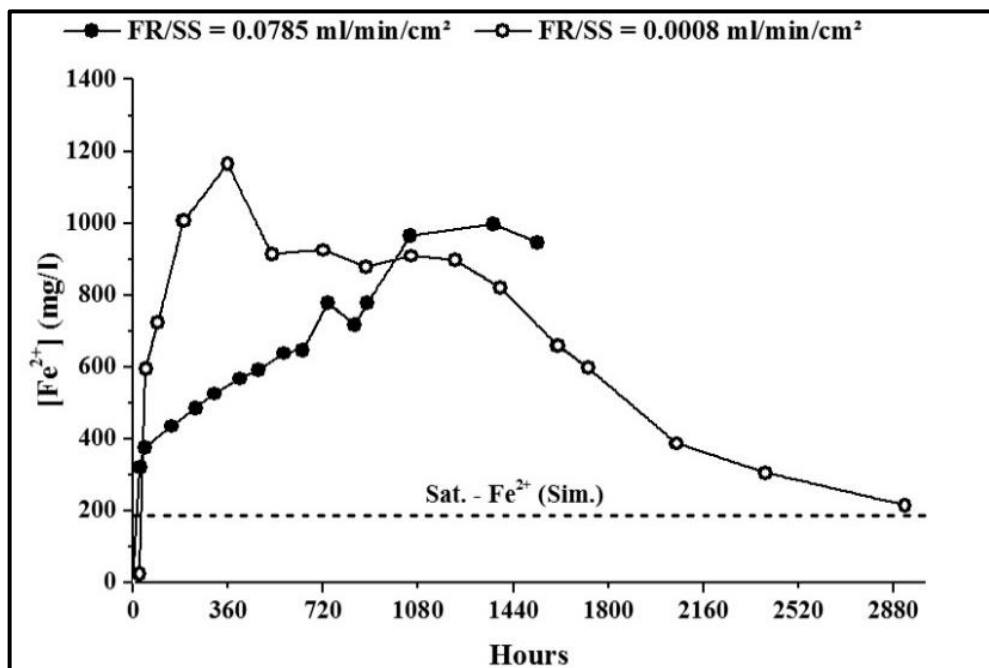
Source: AUTHOR.

Figure 64 shows the evolution of the pH over time for both flow rate regimes. Again, small variations of pH were observed, remaining close to pH6 throughout most of the test period. At 0.0008 ml.min^{-1}.cm^{-2} a maximum value of pH6.15 was reached after 359 hours. At FR/SS of 0.0785 ml.min^{-1}.cm^{-2}, a maximum value of pH6.16 was measured after 1051 hours. As well as occurred with the iron considerations, the results show that the effect of the FR/SS was small, once a flow rate 100 times larger does not significantly influence the maximum values, changing the time required to reach the maxima instead.

Figure 65 shows the simulation of the pH for the high flow rate experiment. A good agreement between the experiment and simulation can be observed. The presence of minor uncertainties should relate to the modelling strategies; the accuracy of the databanks; the accuracy range of the pH probe or the small variations in temperature.

Figure 64: pH values as a function of time and FR/SS of CO_2. Test conditions: V/S of 0.2 ml/cm², 3.5%wt. NaCl brine, at 1 atm of CO_2 and 30±2 °C.
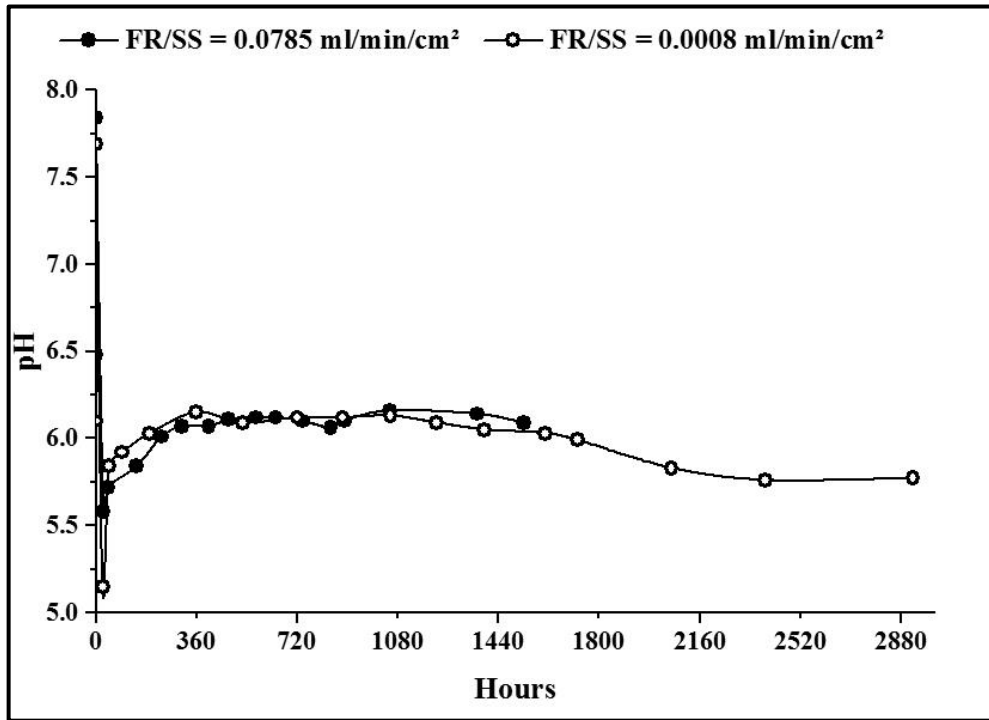
Source: AUTHOR.

Figure 65: Simulation and experimental evolution of pH at 3.5% NaCl brine at 30 °C, 1 atm of CO_2 and flow rate of 0.0785 ml.min^{-1}.cm^{-2}.
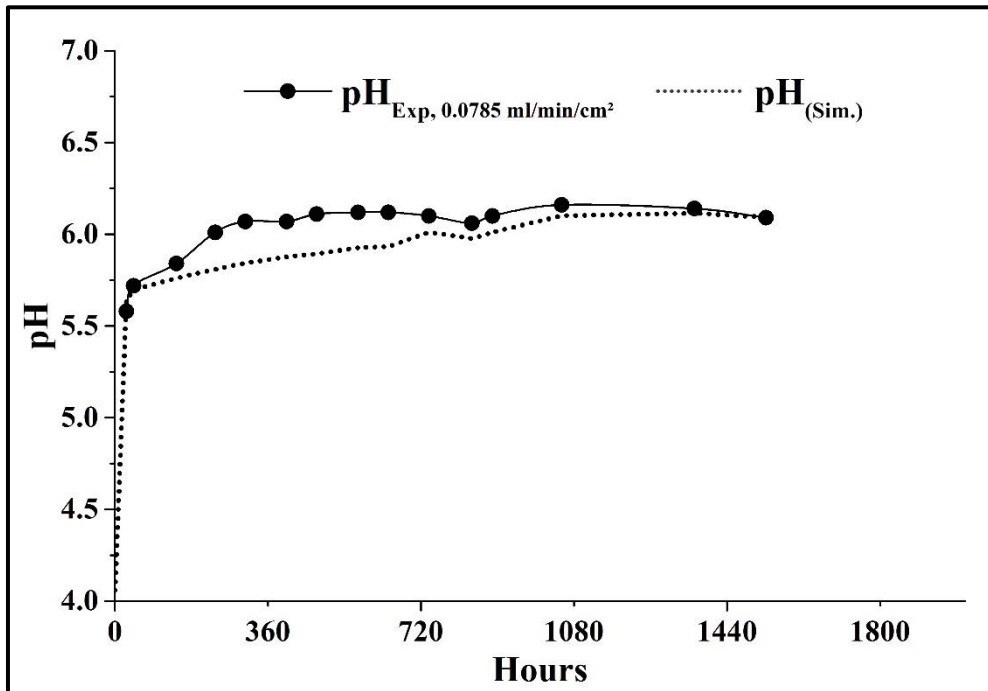
Source: AUTHOR.

Figure 66 shows the OCP of the working electrodes monitored over time for the high flow rate experiment. The trends are essentially similar to those seen for the low flow rate experiment; although the experiment seems to show only two out of the three stages mentioned in the previous sections. Hence, the steady state may not have been achieved in the high flow rate experiment because of the shorter duration of the experiment.

Figure 66: Evolution of the open circuit potentials of working electrodes submerged in the 3.5%wt. NaCl brine, at 1 atm of CO_2 and 30 ± 2 °C, with a FR/SS of 0.0785 ml.min^{-1}.cm^{-2}.
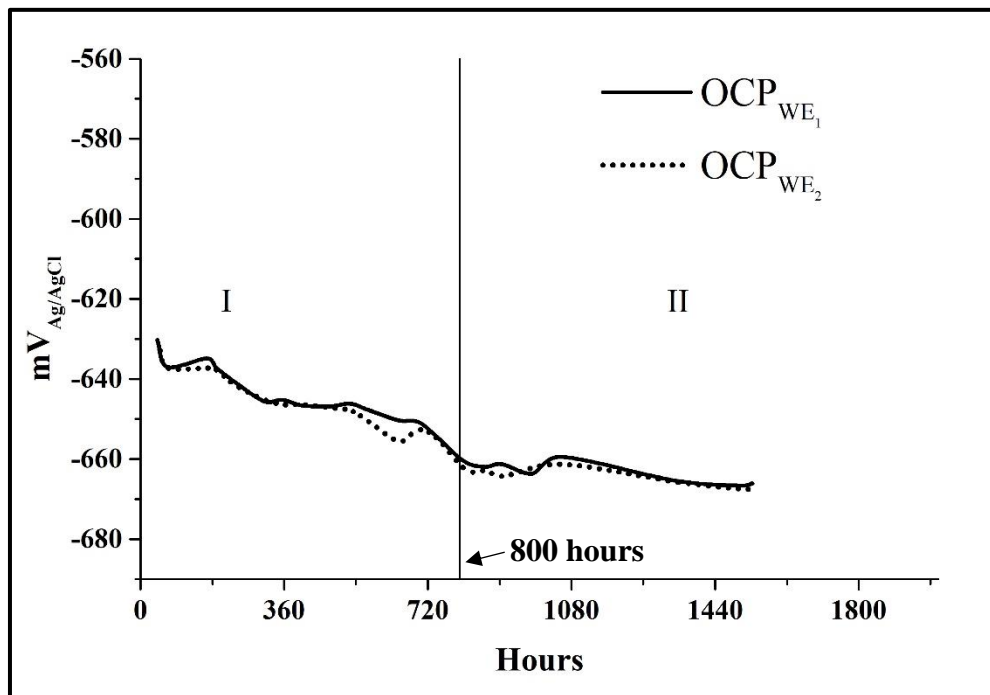
Source: AUTHOR.

Figure 67 shows the experimental moving average and the analytical OCP, the iron concentration and the pH as a function of time for the high flow rate experiment. Once more, the measured OCP is well described by the fitting at all stages, reassuring the correlation discussed in the previous chapters between the OCP, dissolved iron in the solution and the balance of carbonates in the system.

Figure 67: Evolution of the average open circuit potentials, fitting OCP curves, iron in solution and pH. The plot shows two stages, described by Roman numerals "I" and "II". Test conditions: V/S of 0.2 ml/cm², 3.5%wt. NaCl brine, FR/SS of 0.0785 ml.min^{-1}.cm^{-2}, 1 atm of CO_2 and 30±2 °C.
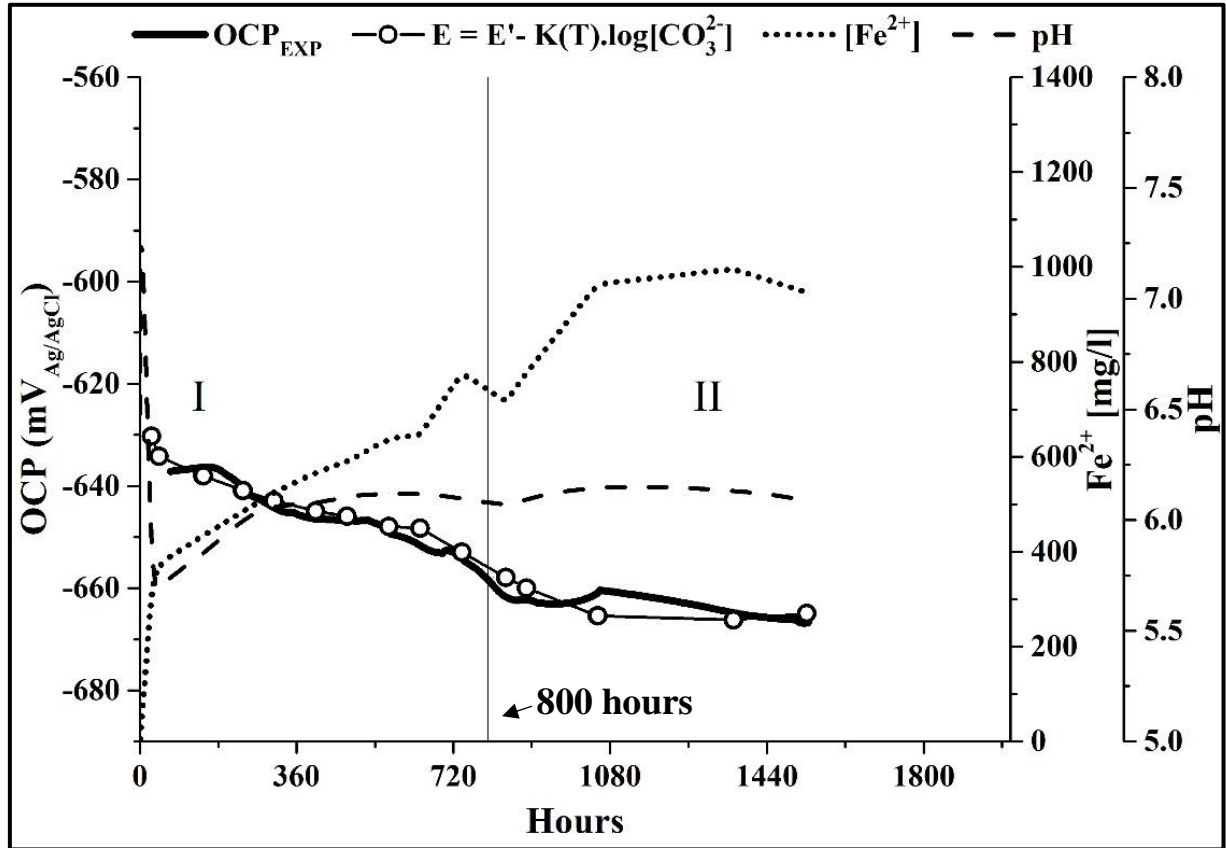
Source: AUTHOR.

Figure 68 shows the evolution of the Rp and CR_{LPR} for the high flow rate experiment. Though a considerable Rp (107468.8 Ohm.cm²) was seen at the beginning of the test, the maximum Rp has not been established within the test timeframe due to the shorter duration of the experiment. The minimum Rp observed was 1661.6 Ohm.cm² at the peak CR_{LPR}, which is very close to the minimum value seen for the low flow rate experiment (1612.3 Ohm.cm²).

The Rp analysis allows a direct comparison between the two flow rate conditions since it is independent of B. Therefore, Figure 69 shows the evolution of Rp with time for the two flow rates investigated that achieved the respective lowest Rp. Apart from the time needed to reach the minimum Rp, no substantial difference between them is seen.

Figure 68: Evolution of the LPR corrosion rate and polarisation resistance (Rp). Test conditions: V/S of 0.2 ml/cm², B of 36.7 mV/dec, 3.5%wt. NaCl brine, FR/SS of 0.0785 ml.min^{-1}.cm^{-2}, 1 atm of CO_2 and 30±2 °C.
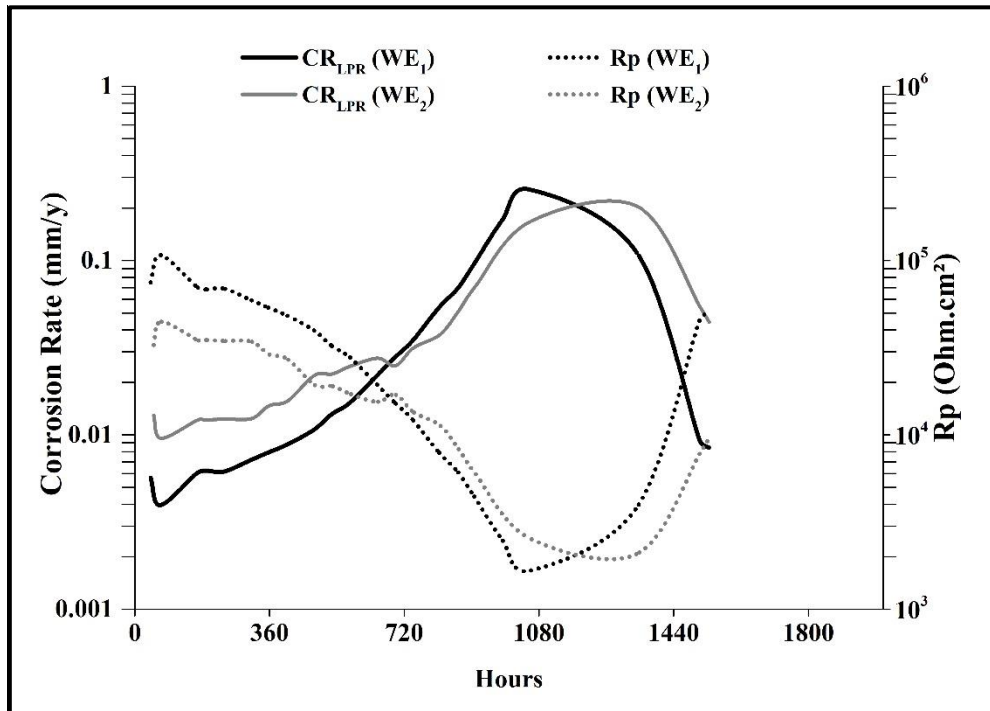
Source: AUTHOR.

Figure 69: Comparison of Rp of working electrodes with respect to the flow rates employed in the experiments. Test conditions V/S of 0.2 ml/cm², 3.5%wt. NaCl brine, 1 atm of CO_2 and 30±2 °C.
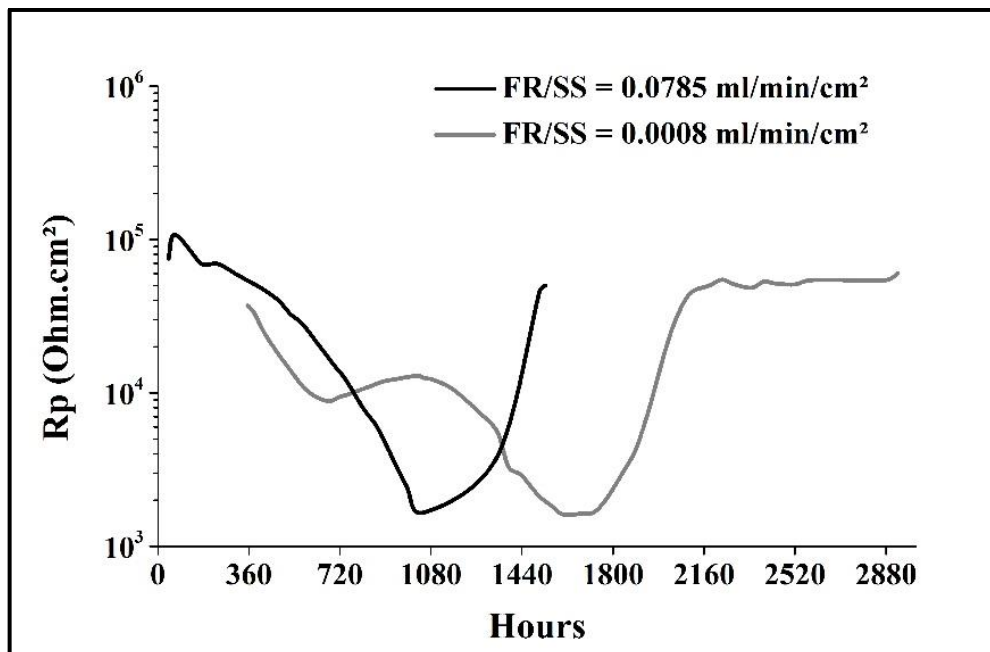
Source: AUTHOR.

Figure 70 shows a summary plot for the high flow rate experiment displaying the CR_{LPR}, OCP, iron concentration and pH. The behaviour between variables is similar to that seen for the low flow rate experiment, although the timescales and some absolute values are different. The OCP falls in-line with the increased Fe^{2+} and pH down to values similar to that seen for the slow flow rate experiment. Note that the trends of all monitored variables are consistent with what was described earlier and that the experiment seems to have been terminated before the third stage could be established.

Figure 70: Evolution of the LPR corrosion rate, OCP, pH and Fe^{2+}. Test conditions: V/S of 0.2 ml/cm², B of 36.7 mV/dec, 3.5%wt. NaCl brine, FR/SS of 0.0785 ml.min^{-1}cm^{-2}, 1 atm of CO_2 and 30±2 °C.
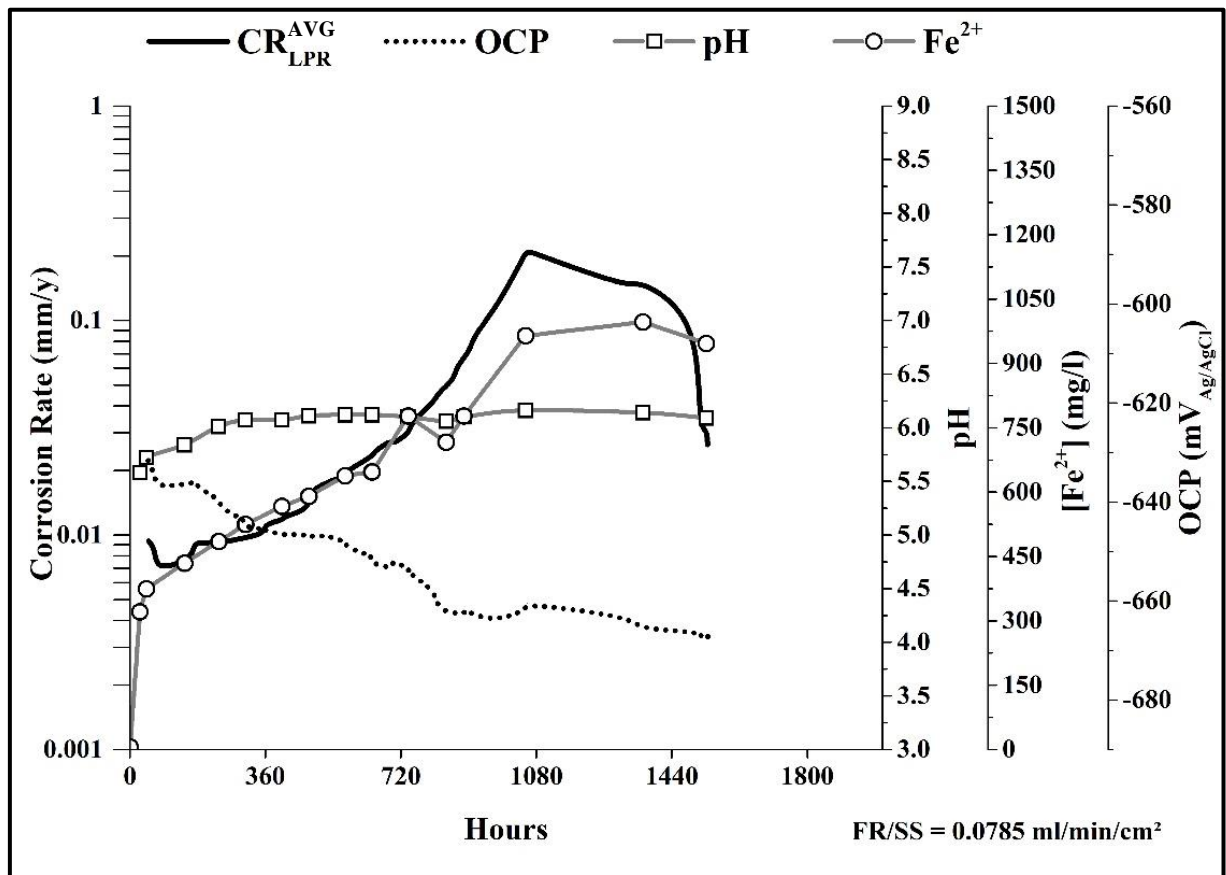
Source: AUTHOR.

Because B can change as the conditions alter during the course of the experiment, the calculated CR_{LPR} should vary in its accuracy. Nevertheless, the CR_{LPR} still serves as a useful indicator regarding the change in rates when the same value of B is used as the reference for both experiments. Keeping that in mind, Figure 71 shows the moving average of the CR_{LPR} from the two flow rate experiments. The plot demonstrates that the corrosion rates reach similar

maximas. Thus, a two-fold increase in the order of magnitude of the CO_2 supply shows no substantial influence on the maximum corrosion rates, even though subtle differences between absolute OCP and Fe^{2+} concentration were seen. Nothing can be assumed for the minimum CR_{LPR}, given the shorter period of the high flow rate test. However, based on the variations of Rp and all variables monitored, it would be reasonable to assume that the CR_{LPR} could be moving towards a plateau of similar magnitude, but the duration of the high flow rate experiment has prevented this from being a certain conclusion.

Figure 71: Comparison of the moving average CR_{LPR} with respect to the flow rates employed in the experiments. Test conditions V/S of 0.2 ml/cm², B of 36.7 mV/dec, 3.5%wt. NaCl brine, 1 atm of CO_2 and 30±2 °C.
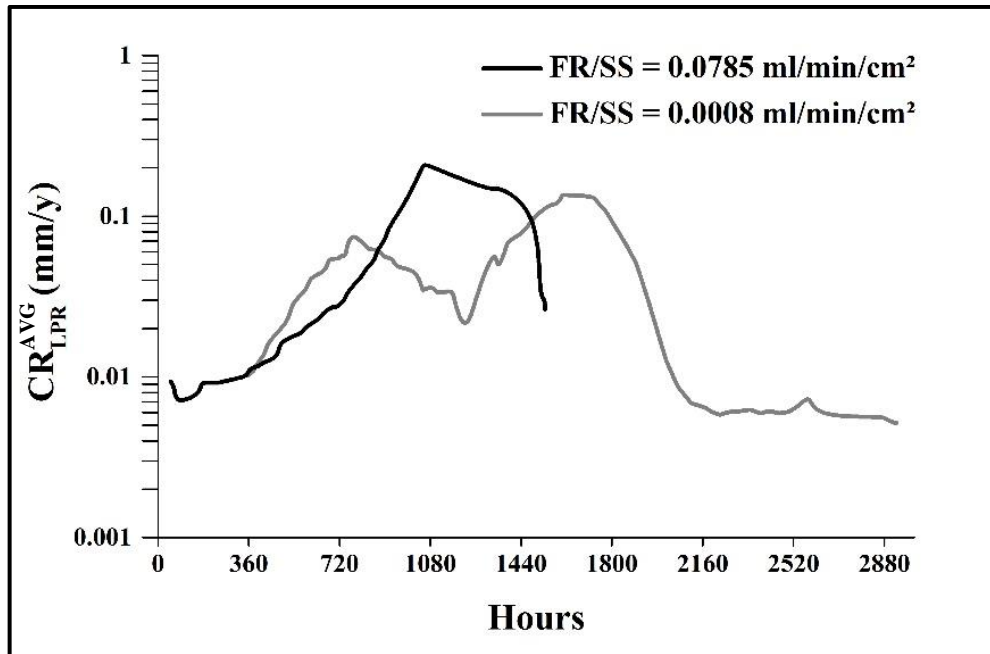
Source: AUTHOR.

A LSV was performed to measure the absolute CR and properties of the surface of the steel at the end of the high flow rate test. The results are shown in Figure 72 and Table 12, featuring a final CR_{LSV} of 0.0109 mm/y at the high flow rate. The two flow rate experiments were interrupted in different stages of evolution, and so it is no surprise that different B values are seen. Note that the long-term, low flow rate, experiment presents a B twice as large as the short-term test, high flow rate. This change mainly results from the evolution of anodic branches during the experiments as the variations of the cathodic portion were less. Observe that the high flow rate experiment presents a b_a almost four times lower (0.054 V/dec) than the one obtained from the low flow rate experiment (0.218 V/dec). In addition, the b_a of 0.054 V/dec is larger than the value attributed to the active dissolution of steel under CO_2-corrosion that ranges

between 0.022 to 0.040 V/dec, but almost half of the value attributed in literature for the mechanism of pre-passivation of steel (0.120 V/dec) (BARKER et al., 2018; KAHYARIAN; BROWN; NEŠIĆ, 2018). Therefore, considering the b_a reported by the literature, it could be presumed an incomplete coverage of scale in the surface of the samples in the high flow rate experiment, providing partial protection for the steel. Concerning the cathodic branch, the experiment with a higher flow rate exhibited a larger b_c that could be expected from the values observed in low flow rate experiment and literature (HERNANDEZ; MUÑOZ; GENESCA, 2012). To understand this result, more experiments would be required. Anyhow, the establishment of mixed mechanisms (charge and mass controlled) is a hypothesis that cannot be discarded.

Figure 72: Linear sweep voltammetry at test end. Test conditions: V/S of 0.2 ml/cm², 3.5%wt. NaCl brine, 1 atm of CO_2 and 30±2 °C.
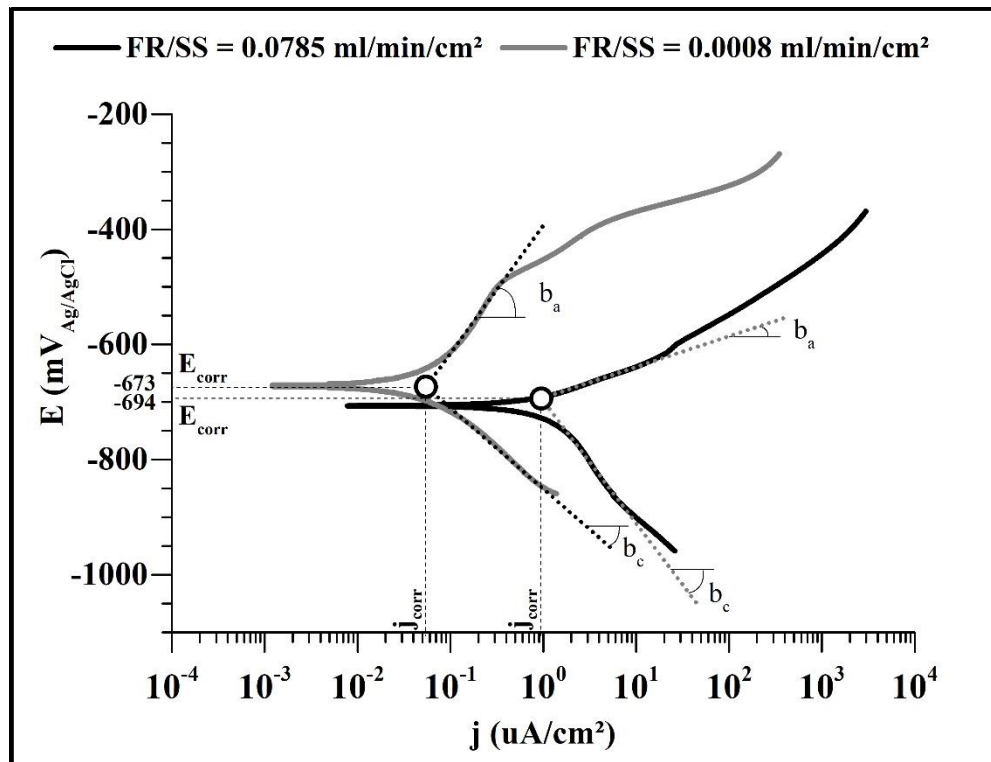
Source: AUTHOR.

Table 12: Linear sweep voltammetry at test end. Test conditions: V/S of 0.2 ml/cm², 3.5%wt. NaCl brine, 1 atm of CO_2 and 30±2 °C.

FR/SS [ml/min/cm²]	E_{corr} [VAg/AgCl]	j_{corr} [A/cm²]	CR [mm/y]	b_a [V/dec]	b_c [V/dec]	B [mV/dec]	Time [months]
0.0785	-0.694	9.4E-07	0.0109	0.054	0.211	18.6	2
0.0008	-0.673	5.4E-08	0.0006	0.218	0.138	36.7	4

Figure 73 compares the CR_{LSV} of the high flow rate experiment with the model proposed by Remita et al. (2008). It is observed that the corrosion rates in the high flow rate experiment fit a θ close to 0.5, instead of the value close to 0.99 observed in the low flow rate experiment. These results not only support that the coverage of the scale and the protection it offers is only partial in the high flow experiment, but also that the corrosion process has not reached a steady state after two months.

Figure 73: Comparison of the corrosion rates obtained by LSV to results described in the literature at various degrees of occlusion.
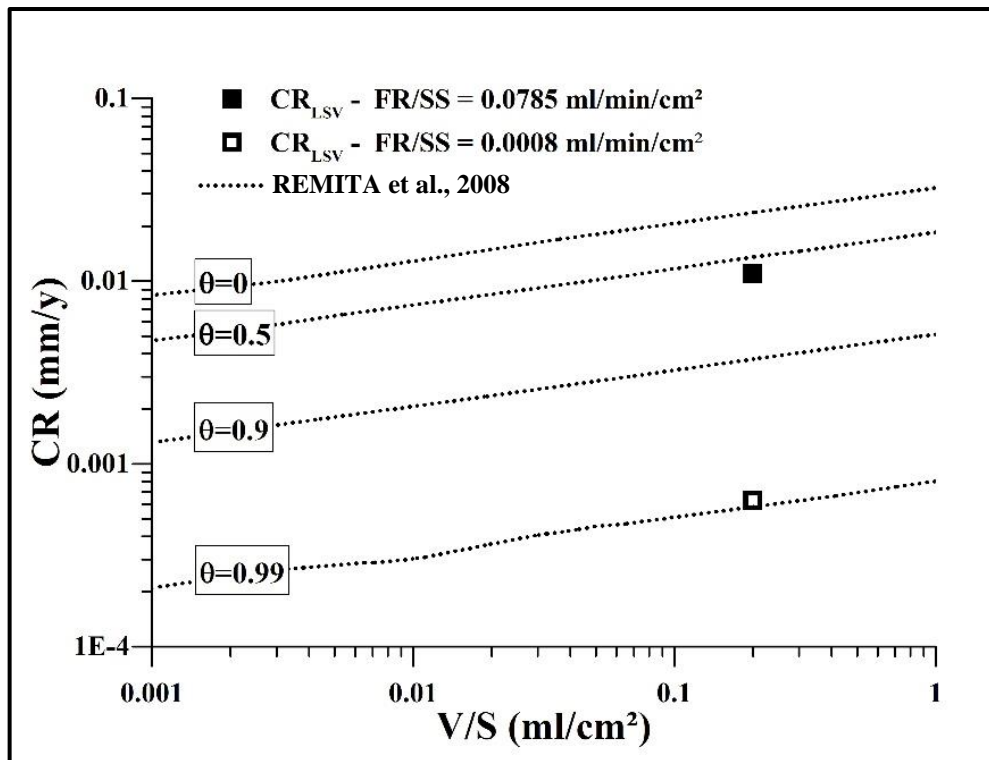
Source: AUTHOR with data extracted from (REMITA et al., 2008).

Table 13 shows the results of the weight change analyses. A nonparametric method was used to calculate the tolerances interval respective to the high flow rate experiment since the data distribution was non-normal. The attempts to transform the data to obtain a normal distribution were not successful. An ACR of 0.0211 mm/y (3.41E-04 mol/(m²h)) was obtained at the high flow rate. The apparent increase in ACR is likely due to the less extended duration of the test, which prevented the drop off in rate associated with precipitation and establishment of a steady state. As well as observed in the low flow rate experiment, the high flow rate experiment showed a considerable ASG in comparison to ACR. The ST obtained was 0.978, which is close to one; meaning that the scale covering the surface of the steel seems to be protective (see Table 14).

Table 13: Average corrosion rate (ACR) and average scale growth (ASG) of high strength steel tensile wires corroded in 1 atm of CO_2 and 30 ± 2 °C.

Test	ACR [mm/y]	Distribution	Outliers [Id. N°]	ASG [mol/(m²h)]	Outliers [Id. N°]	Distribution
FR/SS=0.0785 ml.min^{-1}cm^{-2} (2 Months, 0.2 ml/cm²)	$0.0211^{0.0653}_{0.0030}$	Non-normal	15,17, 28	$3.34E{-04}^{4.86E-04}_{2.03E-04}$	17,36	Non-normal
FR/SS=0.0008 ml.min^{-1}cm^{-2} (4 Months, 0.2 ml/cm²)	$0.0177^{0.0331}_{0.0023}$	Normal	04, 08, 14	$2.67E{-04}^{3.51E-04}_{1.83E-04}$	02, 04, 08	Normal

Table 14: Scaling tendencies of the laboratory experiments.

FR/SS [ml.min^{-1}cm^{-2}]	ACR [mol/(m²h)]	ASG [mol/(m²h)]	ST
0.0785	3.41E-04	3.34E-04	0.978
0.0008	2.84E-04	2.67E-04	0.938

Figure 74 show the corrosion surfaces of the high flow rate experiment viewed in low magnification, and Figure 75 viewed by light microscopy. The images show that the different environmental conditions studied produced similar corrosion products, i.e. darkening of the surface, with no pitting or localised corrosion. Scales uniformly distributed in the samples and disturbed by bubbles (black arrows) were also frequent for all laboratory experiments.

Figure 74: Representative corrosion surface of the samples, demonstrating the specimens before and after the test. Test conditions: V/S of 0.2 ml/cm², 3.5%wt. NaCl brine, FR/SS of 0.0785 ml.min^{-1}cm^{-2}, 1 atm of CO_2 and 30±2 °C.
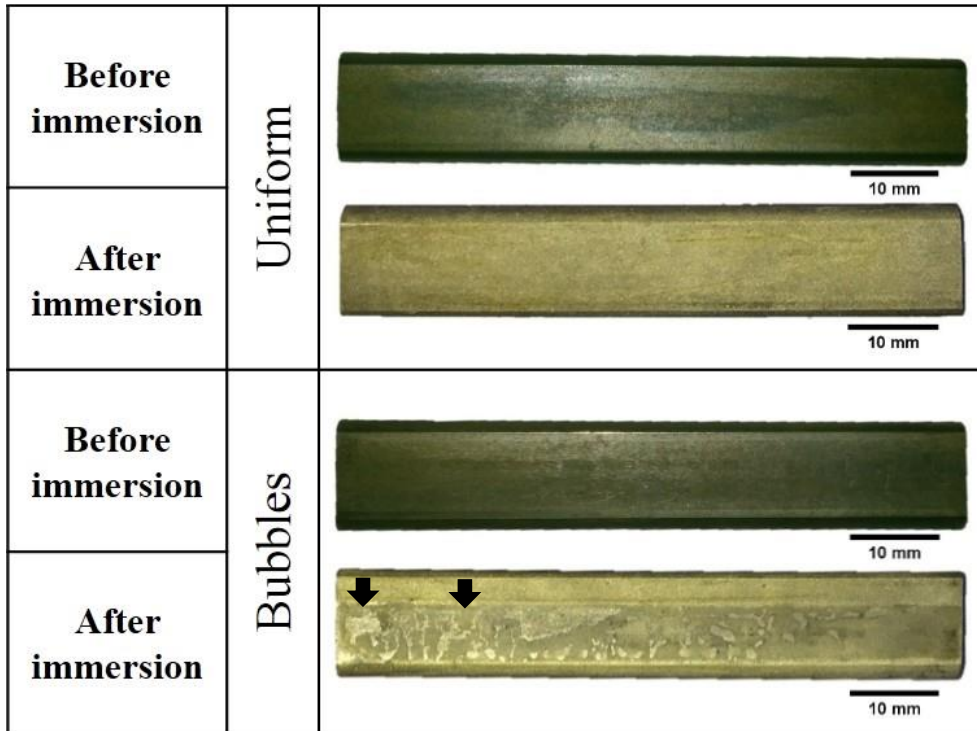
Source: AUTHOR.

Figure 75: Comparison of the corrosion surface of the working electrodes before and after the test. Test conditions: V/S of 0.2 ml/cm², 3.5%wt. NaCl brine, FR/SS of 0.0785 ml.min^{-1}cm^{-2}, 1 atm of CO_2 and 30±2 °C.

Source: AUTHOR.

Figure 76 shows the SEM image of corrosion scale formed during the high flow test over the shorter term of two months, which appeared to have less continuous scale coverage than seen for the low flow rate experiment. It is possible that the heterogeneous nature of the coverage could be resultant of the proximity or contact between adjacent specimens. Five zones were identified (A-E) as per the annotations. Zone A, shown in Figure 77, is a bare metal surface. Zone B shown in Figure 78, shows clusters of corrosion products that can also be seen in the literature (LIU et al., 2016, 2017). Zone C, shown in Figure 79, reveals fine corrosion products. Zone D, shown in Figure 80, features coarser corrosion particles. Perhaps, the presence of distinct grain sizes could be explained by the current stage in the iron carbonate crystallisation process, such as nucleation or crystal growth (BARKER et al., 2018; SUN;

NEŠIĆ, 2008). Zone E, shown in Figure 81, features a heterogeneous coverage that could be connected to a particular stage of the carbonate crystallisation process as well (BARKER et al., 2018). The XRD analysis shown in Figure 82 confirms the presence of $FeCO_3$.

Figure 76: SEM images of corrosion scale formed after two months of testing. Top and bottom surfaces of the selected tensile wire are shown. Test conditions: V/S of 0.2 ml/cm², 3.5%wt. NaCl brine, FR/SS of 0.0785 ml.min^{-1}cm^{-2}, 1 atm of CO_2 and 30±2 °C.
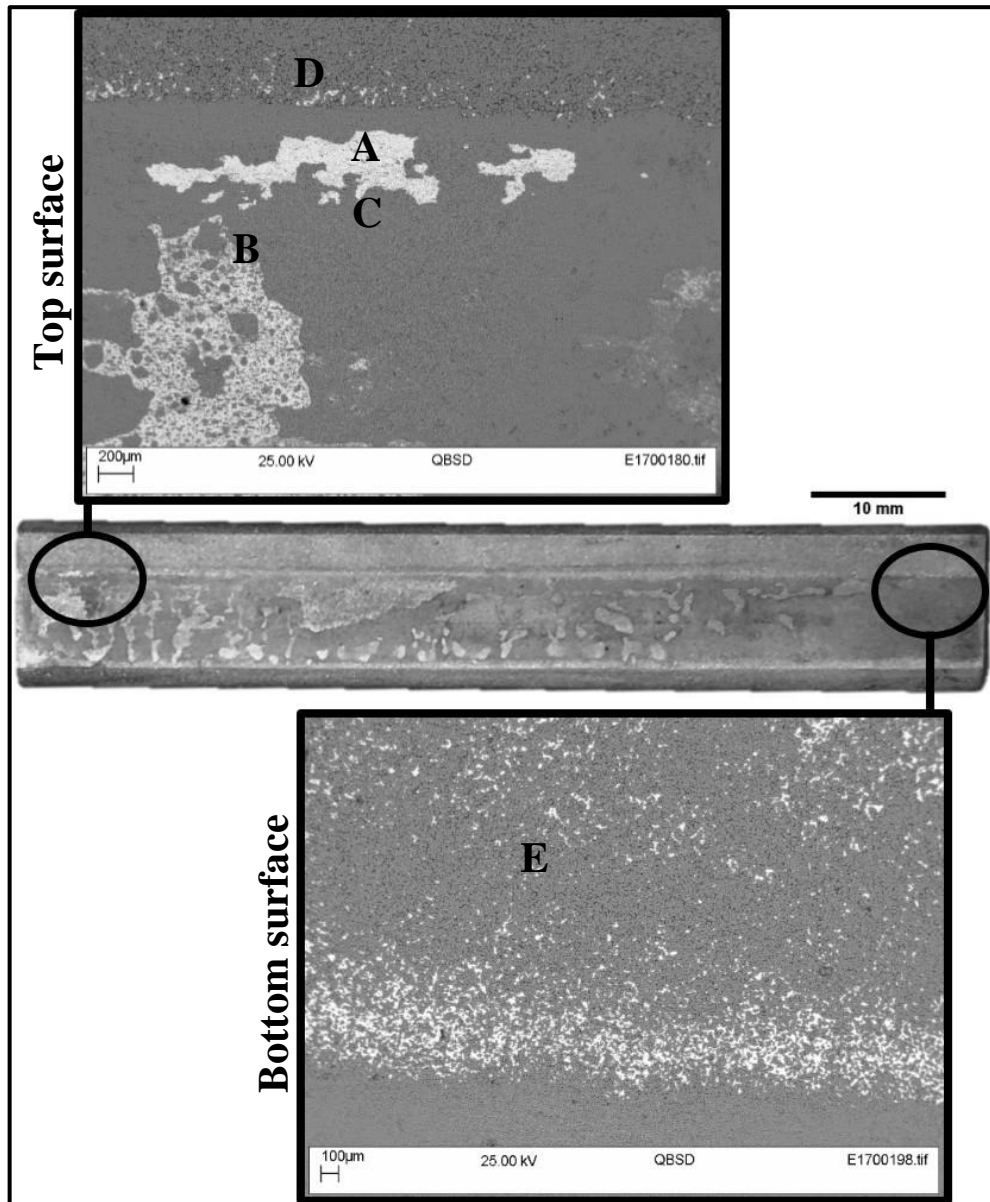
Source: AUTHOR.

Figure 77: Detail of zone A in Figure 76. Test conditions: V/S of 0.2 ml/cm², 3.5%wt. NaCl brine, FR/SS of 0.0785 ml.min^{-1}cm^{-2}, 1 atm of CO_2 and 30±2 °C.
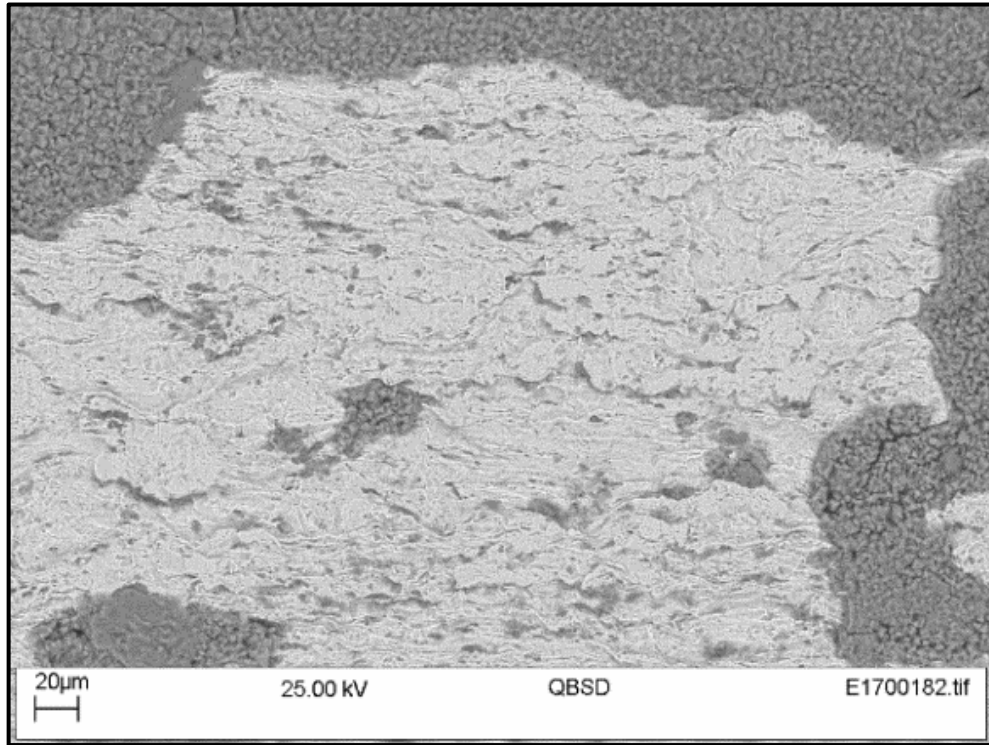
Source: AUTHOR.

Figure 78: Detail of zone B in Figure 76. Test conditions: V/S of 0.2 ml/cm², 3.5%wt. NaCl brine, FR/SS of 0.0785 ml.min^{-1}.cm^{-2}, 1 atm of CO_2 and 30±2 °C.
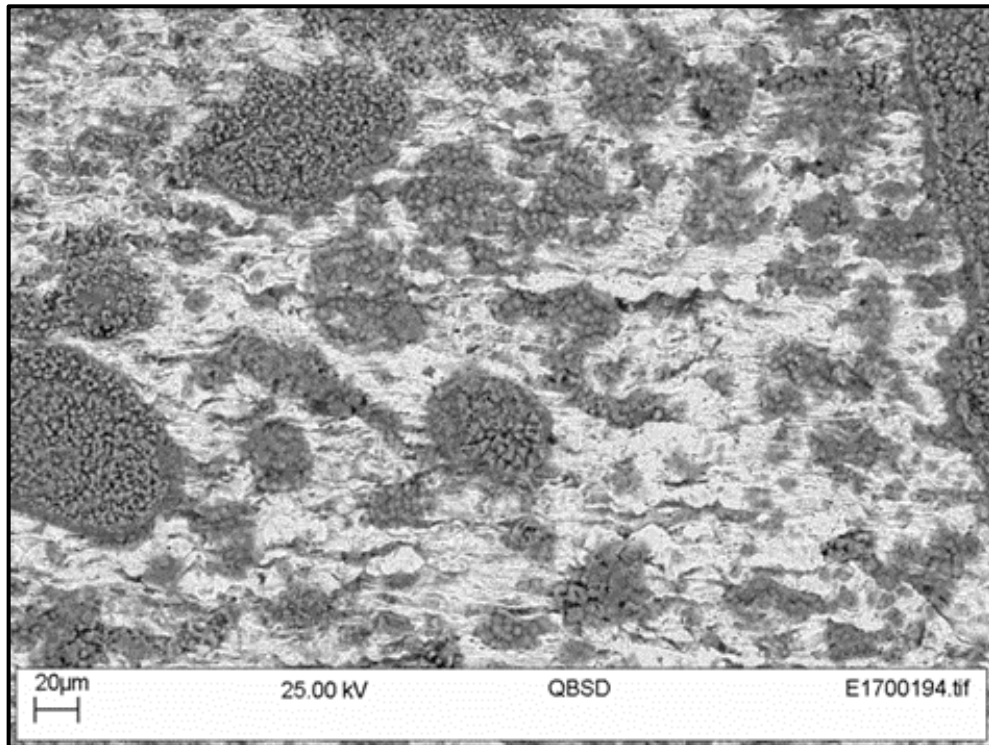
Source: AUTHOR.

Figure 79: Detail of zone C in Figure 76. Test conditions: V/S of 0.2 ml/cm², 3.5%wt. NaCl brine, FR/SS of 0.0785 ml.min^{-1}.cm^{-2}, 1 atm of CO_2 and 30±2 °C.
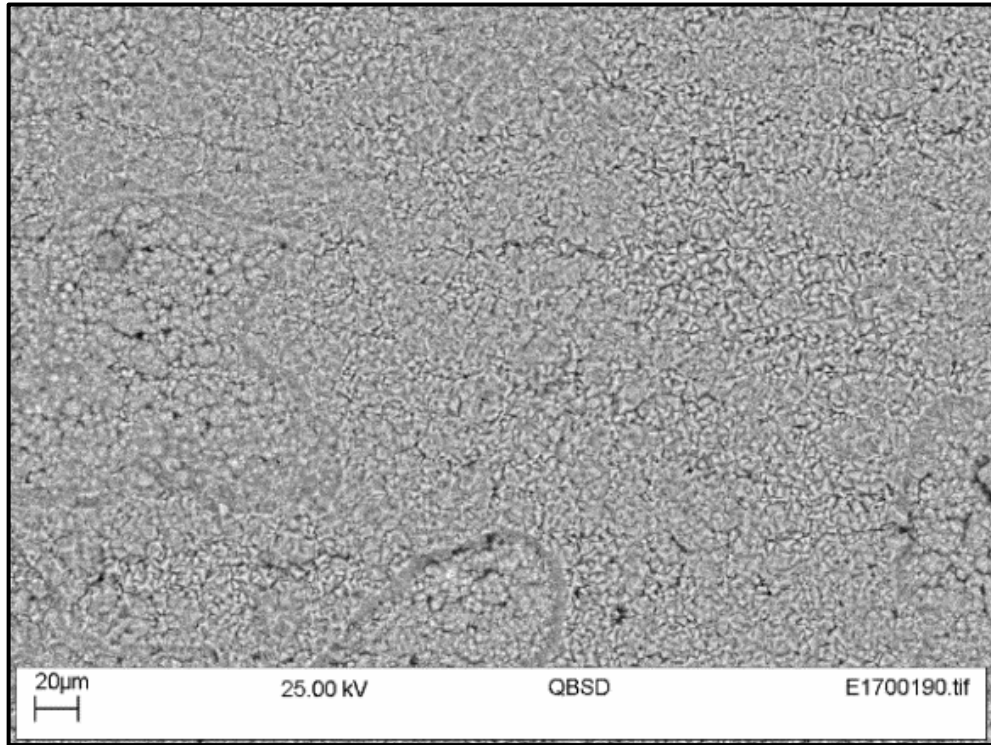
Source: AUTHOR.

Figure 80: Detail of zone D in Figure 76. Test conditions: V/S of 0.2 ml/cm², 3.5%wt. NaCl brine, FR/SS of 0.0785 ml.min^{-1}.cm^{-2}, 1 atm of CO_2 and 30±2 °C.
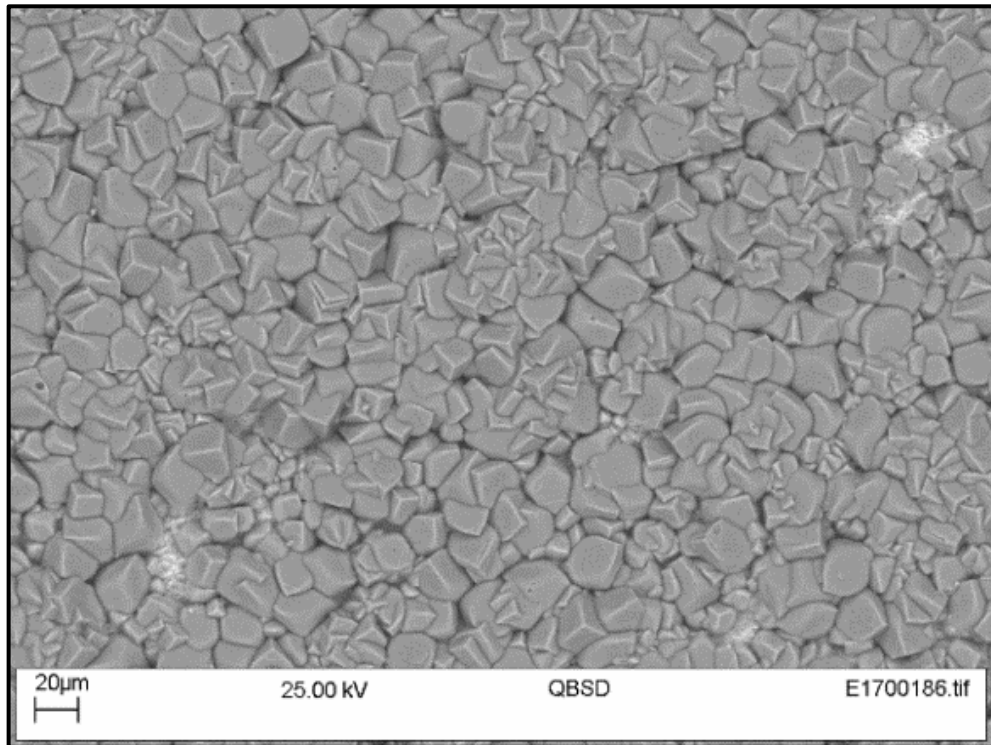
Source: AUTHOR.

Figure 81: Detail of zone E in Figure 76. Test conditions: V/S of 0.2 ml/cm², 3.5%wt. NaCl brine, FR/SS of 0.0785 ml.min^{-1}.cm^{-2}, 1 atm of CO_2 and 30±2 °C.
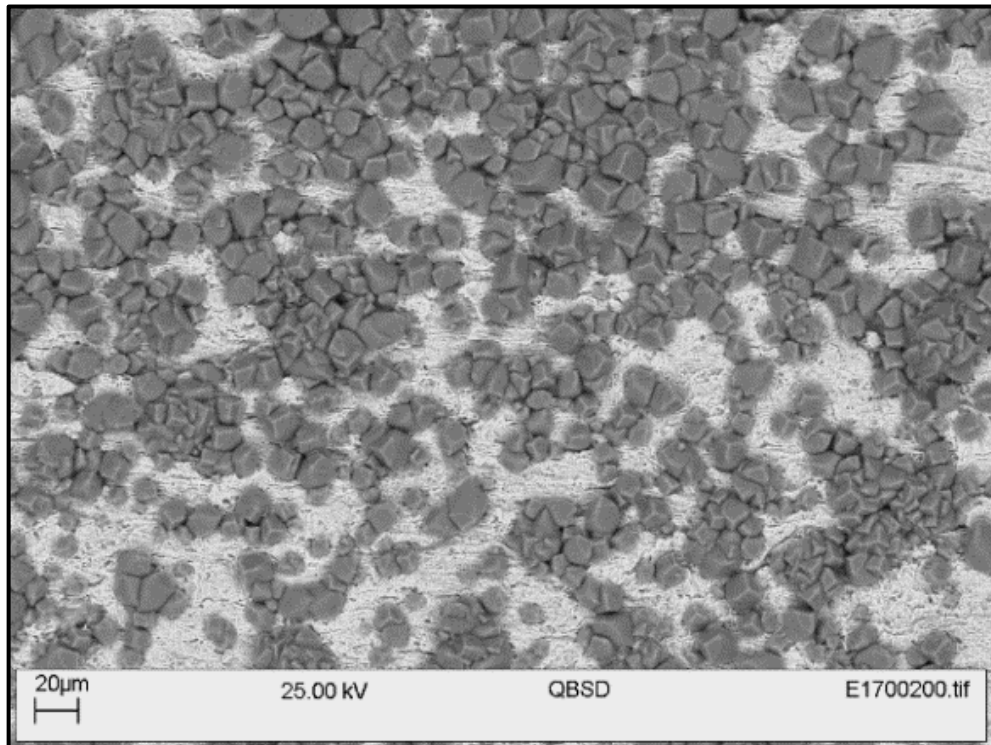
Source: AUTHOR.

Figure 82: XRD results confirming the presence of $FeCO_3$ on the surface of a sample after the test. Test conditions: 3.5%wt. NaCl, 1 atm of CO_2, FR/SS of 0.0785 ml.min^{-1}.cm^{-2} and 30±2 °C.
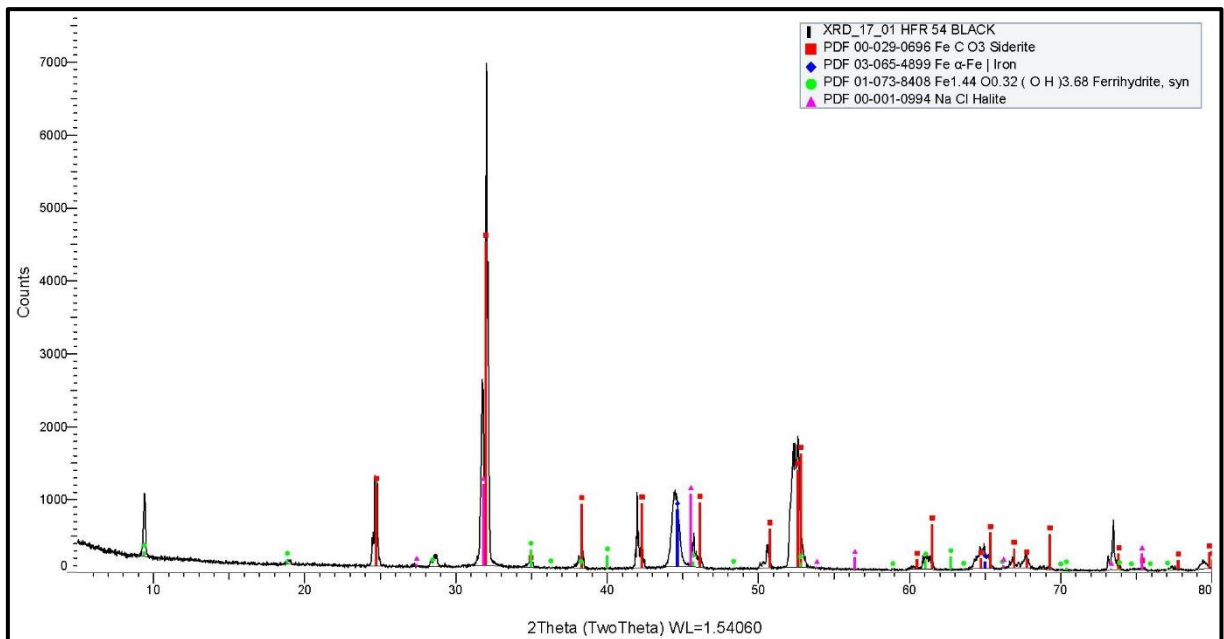
Source: AUTHOR.

Overall, the absence of considerable differences in the corrosion process after a two-fold increase in the flow rates seems, at first glance, to contradict the information reported by Haahr et al. (2016) and Désamais; Taravel-Condat (2009), where new steady state conditions were found. The authors assumed that the consumption of H_2S via corrosion is massive in comparison to the supply in sour service flexible pipes. Consequently, the remaining constituents of the gas (CO_2) would dominate the steady state of the system, i.e. a less aggressive steady state. However, this work realises that the same logic does not apply to pure CO_2-corrosion. It is believed that the specifics of the homogeneous chemical reactions of the H_2O/CO_2 system on the rate of electrochemical reactions are the cause of such difference. Note that carbon dioxide undergoes slight hydration to H_2CO_3 - only ~ 0.26 % (KAHYARIAN; BROWN; NEŠIĆ, 2018) - meaning that even when the flow rate was low, there was plenty reactant available to replenish the consumed H_2CO_3. Moreover, one may notice that basic theory also supports the results from tests carried in this work once FR/SS is a kinetic variable, and so, by definition, it shall not affect the thermodynamics of the system (AMERICAN SOCIETY FOR METALS INTERNATIONAL, 2003). In other words, the difference between the present case and the works of Haahr et al. (2016) and Désamais; Taravel-Condat (2009) lies in the types of gas employed and their interactions with the water and the electrochemical reactions.

4.7. FURTHER CHALLENGES, OPPORTUNITIES AND RESEARCH AREAS FOR EXPLORING THE ANNULUS CO_2-CORROSION OF HIGH STRENGTH STEEL

Based on all that has been observed from the laboratory experiments, from observing the correlations between multiple variables, from simulations, and also from the fact that the CO_2-corrosion essentially relies on the electrochemical interaction between the electrolyte and the surface of the steel; this topic explores the effect of the atmospheric variables by expanding the simulation towards various pressures, temperatures, and concentrations of dissolved iron in the solution. Plausible states of the electrolyte are investigated in search for more critical corrosion patterns. However, it is not intended to provide an assessment or a holistic view of the corrosion process; instead, it is intended to feed the discussion with more data. This chapter recognise the possibility of the potential existence of unknown variables required to represent the harsher environmental conditions in the annulus. However, it was impractical to study a bigger number of variables in the current stage, as additional field information or laborious laboratory investigations would be required.

4.7.1. Effects of atmospheric variables on CO_2-containing brines

A screening of pressure and temperature was performed to explore the hydrochemistry of the brine in the absence of iron ions. The focus is on defining the most aggressive electrolytes when the iron concentration can be neglected. That is, to the initial stages of corrosion or at unrepaired failures of the outer sheath revealing a portion of tensile armour directly to the seawater, currents and tides.

This work assumes that the combination of lower temperatures and higher hydrostatic pressures resemble the case of breaches of the outer sheath at greater depths, whereas high temperatures combined with low pressures could characterise unrepaired failures near the surface; because, the temperature of seawater decreases with depth and pressure increase by 1 atmosphere with every 10 metres of depth. Bearing that in mind, Figure 83 shows the pH of the NaCl 3.5%wt. brine at pressures and temperatures below and above the critical point of CO_2 (31.1 °C and 72.9 atm). The results reveal acidification of the brine as the pressure increase, which is explained by the fact that pressure raises the solubility limit of H_2CO_3, favouring the release of hydrogen ions in the solution, after the chemical dissociation reactions. Consequently, the steeper slopes of acidification at pressures below 7~10 atmospheres would suggest a substantial increase of corrosion rates, but also indicate that the effect of pressure in the corrosion rates could be smaller beyond the range of 1-10 atm. The work of Choi and Nešić (2011) seems to be in line with this assumption, as the authors performed CO_2-corrosion tests in a pressure range between 40 to 80 bar (39.5 to 79 atm) that resulted on high corrosion rates but no considerable increase with pressure at the range evaluated.

Figure 83: Effect of pressure and temperature on the pH of 3.5%wt. NaCl solution saturated with carbon dioxide.
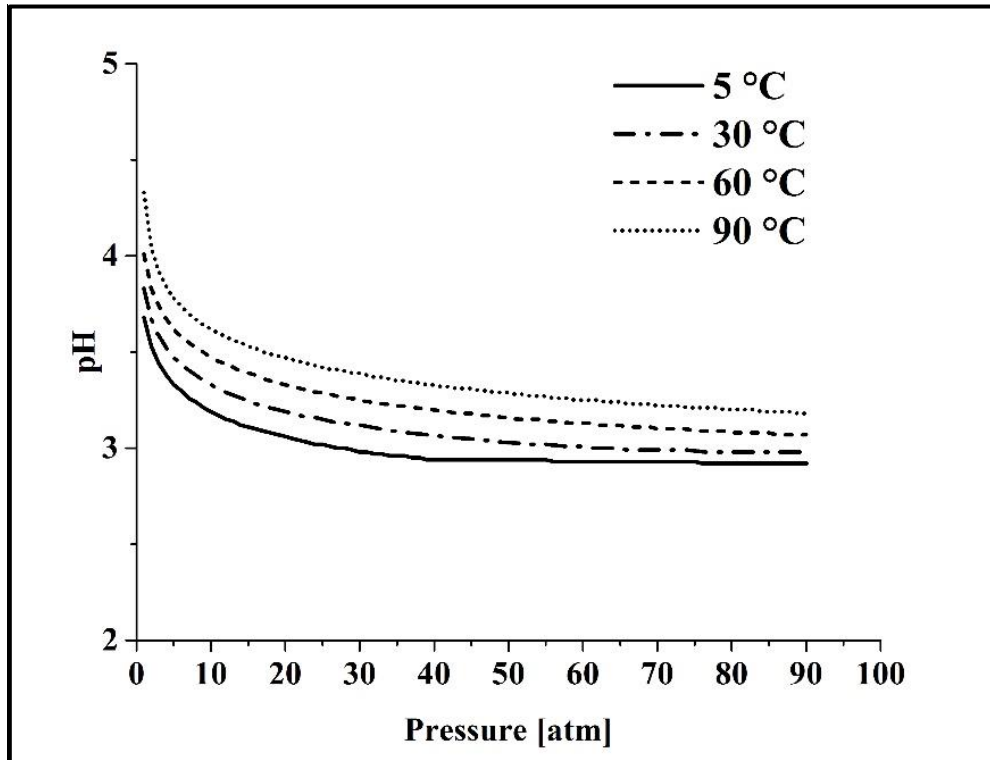
Source: AUTHOR.

It is known that substantial variations on the corrosion rates can occur when the temperatures of the flooded sections of the pipe change, due to variations in the kinetics of the system. In general, the increase of temperature increases the corrosion rates. However, in the range evaluated, the statement above contrasts with the thermodynamic point of view presented by Figure 84, because it shows that the increase of temperature decrease the solubility of carbon dioxide, which shall result in less aggressive solutions. Therefore, to understand the effect of the variables and to select the variables of further testing of the annulus, it is imperative to bear in mind the consequences in the field of kinetics and thermodynamics.

Figure 84: Solubility limit of carbon dioxide and pH in 3.5%wt. NaCl brine as a function of temperature and pressure. a) 5 °C. b) 30 °C. c) 60 °C. d) 90 °C. e) Comparative.
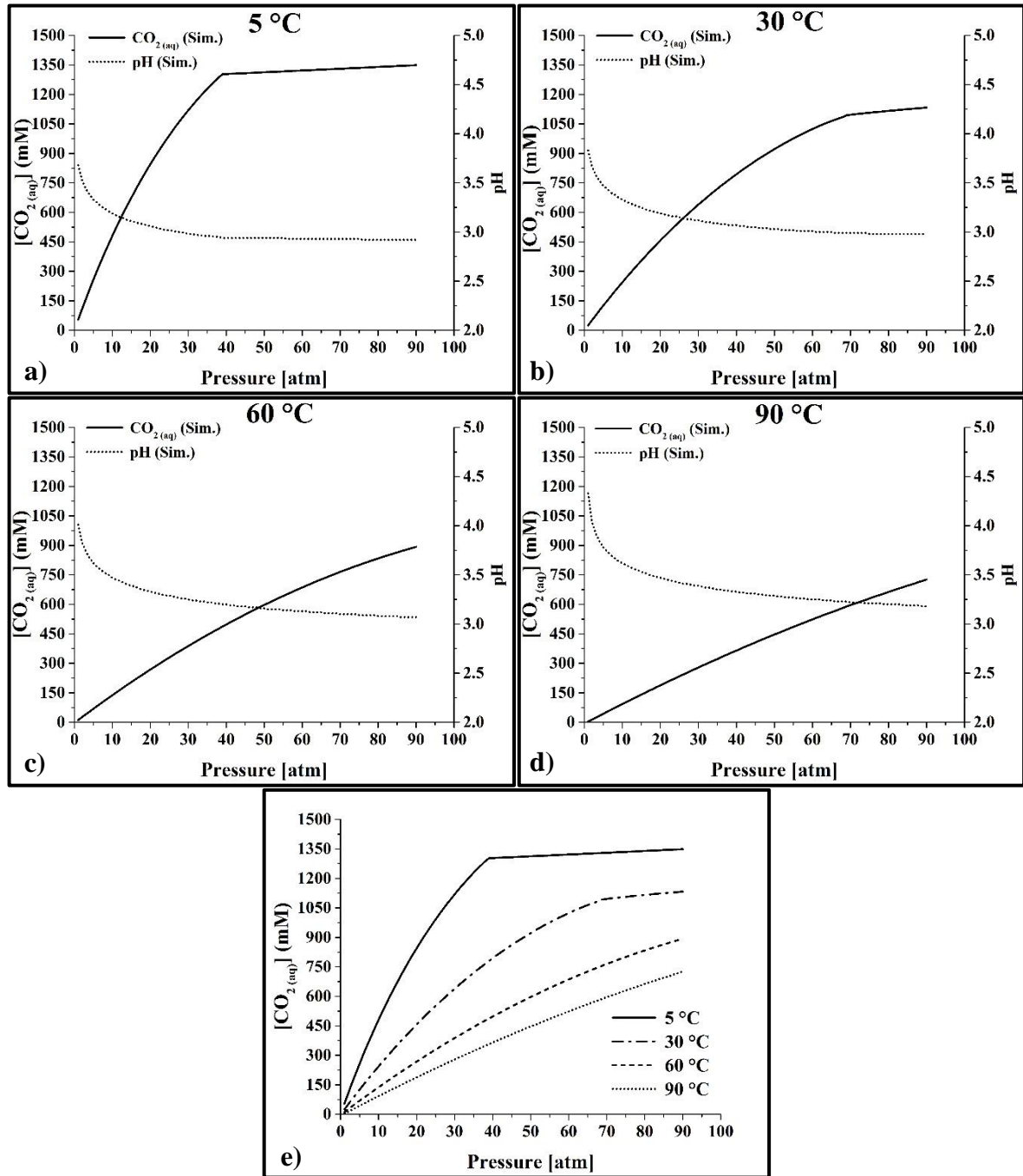
Source: AUTHOR.

Furthermore, the curves beneath the critical temperature of the carbon dioxide (31.1 °C) present a discontinuity coinciding to the point where the carbon dioxide change from gas to a liquid phase. This way, the concentration of carbon dioxide and the pH stabilise after the transition. Such a behaviour can be beneficial for further experimental testing of the annulus CO_2-since it shows that it may not be advantageous to increase the pressure much beyond the phase transition at temperatures below the critical point because [$CO_{2(aq)}$] would not change

that much. The fact that safety and practical test requirements usually escalate with the working pressure of the test vessel would justify this approach. Above the supercritical temperatures and pressures, the fluid cannot be clearly distinguished between gas and liquid. This is portrayed by the smoother curves of CO_2 solubilities and pH.

Another opportunity to simplify further corrosion testing involves the typical procedures of pre-saturation or re-saturation with CO_2 for tests at higher pressures and warm temperatures. These procedures generally involve bubbling of gas in an auxiliary vessel to achieve the saturation of the solution with carbon dioxide before transferring to the test vessel. Because of the pressure, this procedure can sometimes be complicated or expensive. Thus, using colder temperatures at lower pressures for pre-saturations or re-saturations can produce an alternative solution, analogous to the specified environment. Table 15 shows an arbitrary example. In this example, two brines with different pressures and temperatures would show similar concentrations of CO_2 and pH according to simulation. An alternative pre-saturation or re-saturation in ambient temperature at 1 atmosphere would offer almost half of the concentration of $CO_{2(aq)}$ and a slightly higher pH.

Table 15: Analogous 3.5%wt. NaCl brines saturated with carbon dioxide.

Solution	Temperature/Pressure	pH	$CO_{2(aq)}$
3.5%wt. NaCl/CO_2 brine	45 °C/3 atm	3.66	54.06 mM
3.5%wt. NaCl/CO_2 brine	5 °C/1 atm	3.67	54.02 mM
3.5%wt. NaCl/CO_2 brine	25 °C/1 atm	3.80	28.23 mM

4.7.2. Annulus environment – iron-saturation.

The long-term laboratory experiment revealed that the composition of the electrolyte returned towards the saturation point. Then, based on this evidence, simulations were carried out to investigate properties of the saturation of 3.5%wt. NaCl/CO_2 brines with CO_2 and iron ions under various pressures and temperatures. Also, this work assumes that the form of corrosion, the mechanism, and the corrosion rate of the occluded tensile wires shall depend on the electrochemical interaction between the electrolyte and the surface of the steel. This means that understanding the electrolyte and the aspects related to its aggressiveness in equilibrium could help to anticipate the long-term impact on the corrosion of the occluded HSS wires after the steady state is reached.

Figure 85 displays the simulation of the composition of 3.5%wt. NaCl solution saturated with iron ions and carbon dioxide at various temperatures and pressures. In the range studied,

with the increase of temperature on the low-pressure range it is observed an increase in the pH and carbonate, but a decrease in the solubility of iron, carbon dioxide and bicarbonate. The opposite behaviour is observed for the increase of pressure on the low-temperature range. Further combinations of pressure and temperatures make the interpretation of the results complex, due to the inter-related outcomes. Hence, in order to improve comprehension and to propose further testing of the annulus, the data was combined into six zones of risk shown in Table 16.

Figure 85: Composition of 3.5%wt. NaCl solution saturated with iron ions and carbon dioxide at various temperatures and pressures. a) pH_{sat}, b) $[CO_{2sat}]$, c) $[HCO_3^-{}_{sat}]$, d) $[CO_3^{-2}{}_{sat}]$ and e) $[Fe^{2+}{}_{sat}]$.
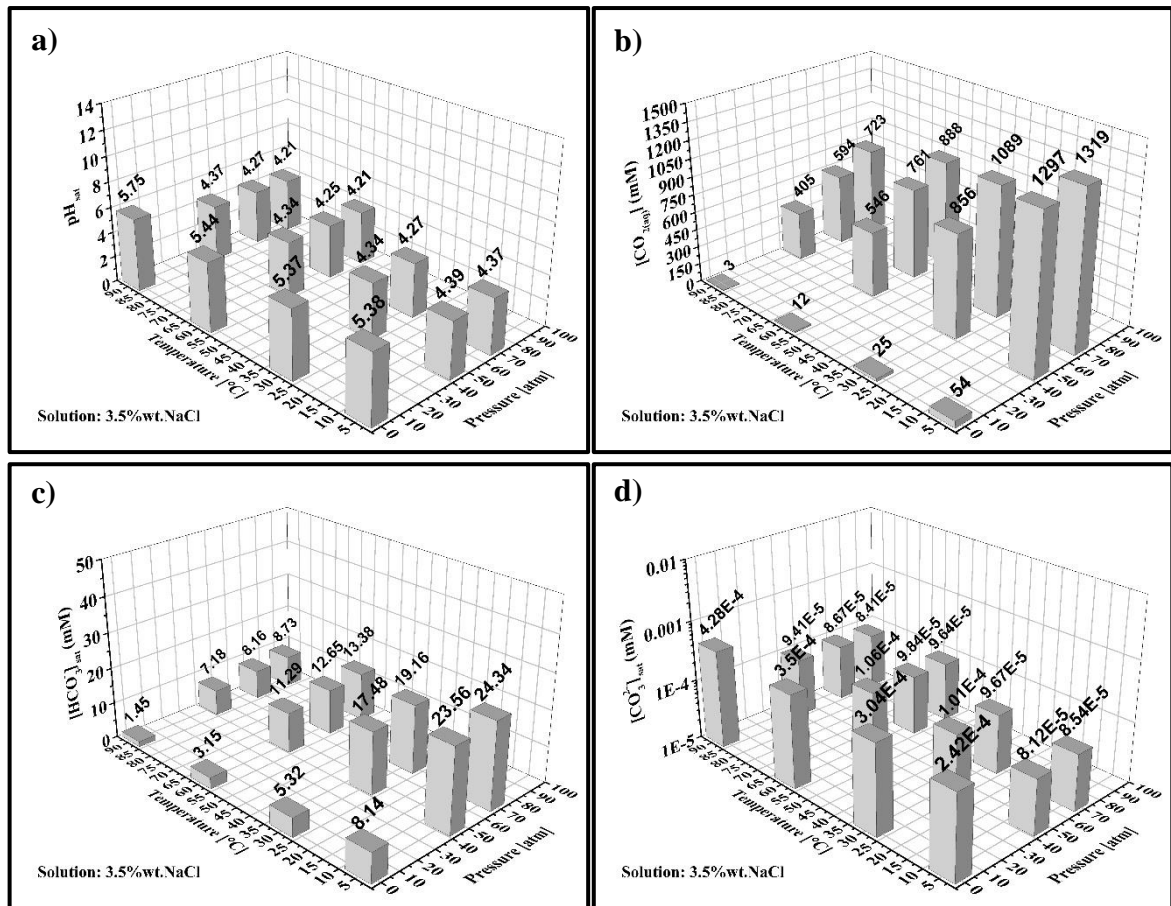
Continuation of the Figure 85
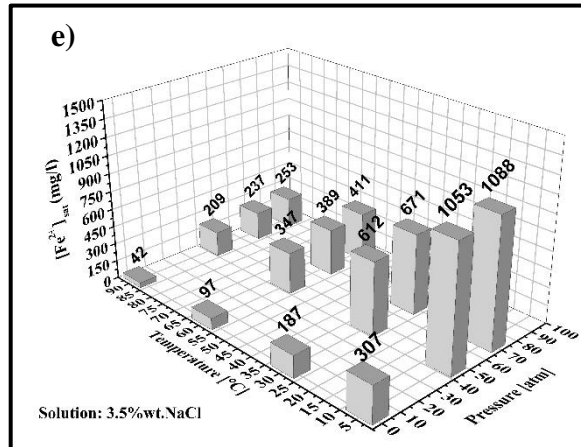
Source: AUTHOR.

Table 16: Six zones for the study of CO_2-corrosion of unbounded flexible pipes according to simulation.

Zone	Pressure	Temperature
(a)	(1<P<10) atm → Low	(65<T<90) °C → High
(b)	(1<P<10) atm → Low	(25<T<65) °C → Moderate
(c)	(1<P<10) atm → Low	(5<T<25) °C → Low
(d)	(10<P<90) atm → High	(65<T<90) °C → High
(e)	(10<P<90) atm → High	(25<T<65) °C → Moderate
(f)	(10<P<90) atm → High	(5<T<25) °C → Low

Zones (a) and (b) are characterised by the low solubility of iron, the pH closer to neutrality and a fair amount of carbonates. Therefore, given the state of the electrolyte, it can be argued that HSS tensile wires in brines in these zones could lead to the fast formation of protective scales and low corrosion rates after the steady state. The data presented in the long-term (low flow rate) experiment is in line with this statement as a considerable growth of protective scales, and low corrosion rates were seen. Given the low solubility of iron, it can be assumed that these solutions require less corrosion of the wires to reach the supersaturation domains, i.e. the precipitation of process could begin sooner. Barker et al. (2018) demonstrated that environmental conditions producing lower solubilities of $FeCO_3$ lead to faster precipitation rates, in line with the statement above. Because of the considerable difference in temperatures, zones (a) and (b) could diverge concerning scale morphology and other kinetic factors. Furthermore, the unbounded flexible pipes wires may undergo considerable mechanical stress caused by the self-weight of the structure, bending or tidal action. This aspect can potentially increase the risks of failure by SCC or localised corrosion if the applied stresses happen to break the protective scales, whose morphology could be temperature dependent.

Assuming the temperature range of zones (d) and (e), the formation of protective scales could potentially occur as well as in zones (a) and (b). However, in the face of the more substantial pressures, the pH shall decrease, raising the corrosion rates at steady state. It is also reasonable that kinetic factors and scale morphology would change, making an experimental investigation of such an interesting subject, in particular, for assessing the chemical stability of the $FeCO_3$ and the risk of SCC given the potential risk of chemical destabilisation induced by the high concentration of CO_2. According to Han et al. (2007) and others (SCHMITT; HÖRSTEMEIER, 2006), the risk of localised corrosion or aggravation on the susceptibility to SCC are connected to the acidity and concentration of H_2CO_3.

Zones (c) and (f) can be connected to service in extremely cold exploitation sites or at considerable depths, respectively. The brine in these zones would tend to be somewhat acid and display high solubilities of iron. Because of these properties, such electrolytes would allow considerable corrosion of the confined wires before any precipitation or formation of protective scales. Consequently, scale-free corrosion processes may be stable. However, notice that the colder temperatures can decrease the rate of electrochemical processes. Then, the magnitude of the corrosion rate becomes difficult to predict, as the effect of the acidic pH would compete against the decrease in the rate of electrochemical processes. Therefore, additional long-term occluded CO_2-corrosion testing would be vital to narrow the gaps in knowledge and learn more about the effect of pressure in colder temperatures.

4.7.3.   Annulus environment – undersaturation and supersaturation with iron.

The work already addressed the situation where the concentration of iron in the electrolyte evolves to the saturation point. However, it is possible that the solution would remain undersaturated or that the concentration of iron would never return to the saturation point during the life cycle of the pipe. The real-scale tests of unbounded flexible risers, performed by Borges (2017) and Ke et al. (2017) confirmed the possibility of the annulus remaining for considerable time above the saturation frontier. The degree of occlusion, flow rate, pressure, temperature, fluid dislocation and kinetics are examples of plausible factors that could affect the evolution of the dissolved iron in the solution and properties of the corrosion process.

In view of this, Figure 86 display simulations combining temperature, pH and $[Fe^{2+}]$. The typical range of pH found in the annulus of unbounded flexible pipes is seen by the grey shadows. The simulations indicate that such a range can be reached at 1 atmosphere in the undersaturation with iron ions domain, whereas at higher pressures it can only be achieved after

high supersaturations with iron. This implies that, in pressurised brines, the structural layers of the pipe could undergo more corrosion just to reach the commonly accepted range of pH expected for the annulus. In such case, due to the more aggressive environment, the maximum concentration of iron in the solution could potentially increase as well.

Moreover, using the plot as guideline and the information available in the literature as reference, it is possible to propose the risk of different corrosion mechanisms in HSS tensile wires based on aggressiveness aspects of the solution. For instance, assuming the long-term interaction between the metal surface and brine with a high degree of supersaturation with iron, it is possible to presume the formation of strong protective scales of iron carbonates and decreasing corrosion rates. On the other hand, flooded annulus with moderate supersaturation with iron can trigger localised galvanic mechanisms and cause the initiation and growth of localised corrosion. However, when the annulus is flooded with iron-undersaturated solutions, there would be the potential risk of scale-free uniform corrosion, iron dissolution and chemical destabilisation of protective scales. These assumptions find support on the information available in the literature concerning the mechanisms of CO_2-corrosion (BARKER et al., 2018; HAN et al., 2007; MITZITHRA; PAUL, 2016; SCHMITT; HÖRSTEMEIER, 2006; SUN, 2006).

Figure 86: Combined effect of temperature and [Fe^{2+}] on the pH of the 3.5%wt. NaCl brine at a) 1 atm of CO$_2$, b) 45 atm of CO$_2$, c) 70 atm of CO$_2$ and d) 90 atm of CO$_2$. The hollow points show the pH respective to the point of solubility limit with iron. The shadow indicates a range of pH considered for annulus environments.
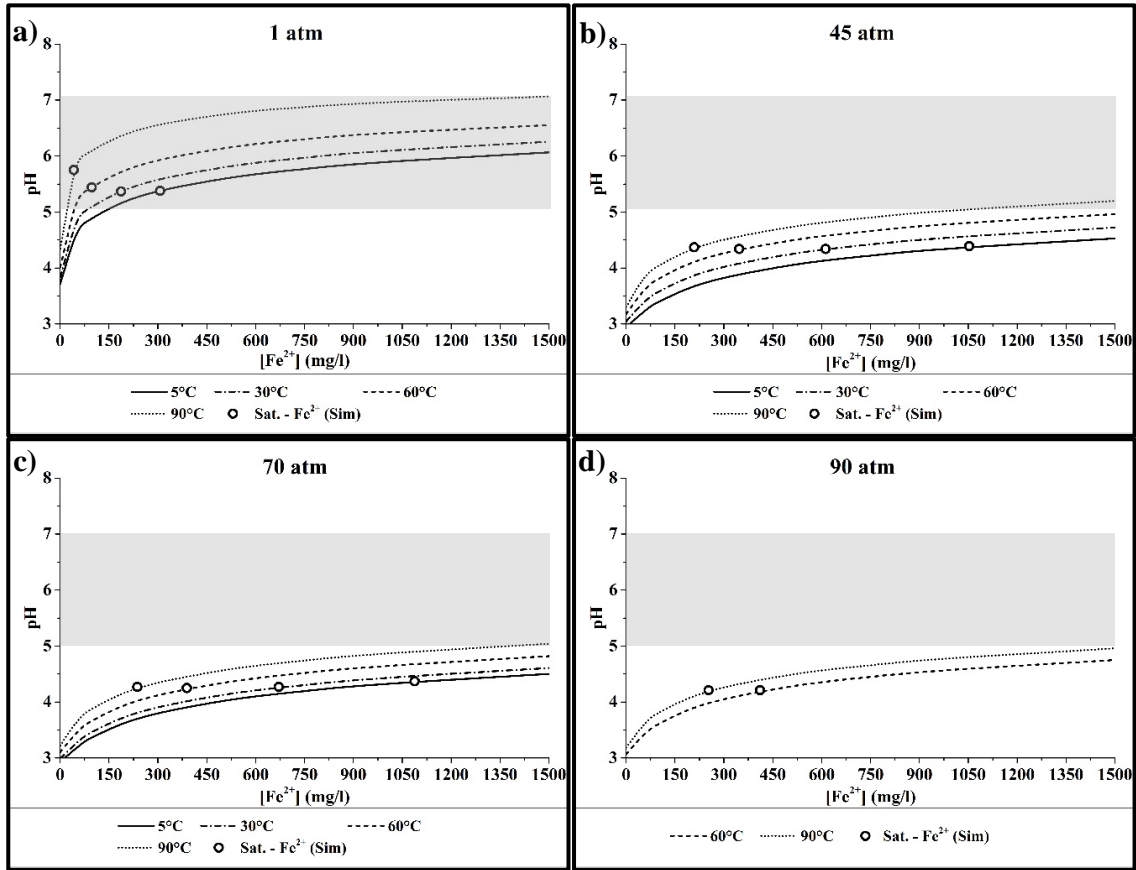
Source: AUTHOR.

5.   CONCLUDING REMARKS

The following conclusions are drawn by the investigation of the annulus CO_2-corrosion of high strength steels and the influence of flow rates and atmospheric variables:

- A clear dependence between the properties of the electrolyte and the occluded corrosion of the high strength steel at the different flow rate regimes was observed. Changes in the open circuit potential, in the corrosion rates, in the pH and the concentration of iron ions in the solution were monitored over time, being able to describe three stages of the annulus CO_2-corrosion. These were: I - iron dissolution and super-saturation in solution up to a peak corrosion rate; II – intense precipitation and gradual reduction of corrosion rates; III - steady state corrosion at a reduced rate. In other words, the corrosion phenomenon was strongly influenced by the trade-off between the corrosion and the precipitation of iron carbonate.

- The images of the corrosion surfaces show darkening of the surface, with no pitting or localised corrosion. Scales uniformly distributed in the samples and disturbed by bubbles were present in all laboratory experiments.

- The change of two orders of magnitude in the flow rate of CO_2 caused no relevant effect on the absolute corrosion rates and general behaviour. It is believed that the specifics of the homogeneous chemical reactions of the H_2O/CO_2 system on the rate of electrochemical reactions are the cause of such behaviour.

- The occluded electrolyte consisting of the 3.5%wt. NaCl brine in contact with carbon dioxide was reproduced by commercial models, regarding pH and composition. This evaluation provided a basis for further investigation on more critical corrosion patterns, studied through simulation of plausible states of the electrolyte in respect to variations of pressure, temperature and concentration of iron ions in the solution. The risk of activating different corrosion mechanisms was predicted at harsher environmental conditions.

REFERENCES

4SUBSEA. **Unbonded flexible risers – Recent field experience and actions for increased robustness**. Hvalstad, Norway: 4SUBSEA, 2013.

ALMEIDA, T. das C. et al. New insights on the role of CO_2 in the mechanism of carbon steel corrosion. **Corrosion Science**, v. 120, p. 239–250, 2017.

AMERICAN PETROLEUM INSTITUTE. **Recommended practice for flexible pipe**, American Petroleum Institute, 2008.

AMERICAN SOCIETY FOR METALS INTERNATIONAL. **Corrosion: fundamentals, testing, and protection**. Materials Park, United States of America. v. 13A

AMERICAN SOCIETY FOR TESTING AND MATERIALS. **Standard practice for calculation of corrosion rates and related information from electrochemical measurements**, ASTM International, 1989.

AMERICAN SOCIETY FOR TESTING AND MATERIALS. **Standard test method for conducting potentiodynamic polarization resistance measurements**, ASTM International, 1997.

AMERICAN SOCIETY FOR TESTING AND MATERIALS. **Standard practice for preparing, cleaning, and evaluating corrosion test specimens**, ASTM International, 2003.

AMERICAN SOCIETY FOR TESTING AND MATERIALS. **Standard guide for laboratory immersion corrosion testing of metals**, ASTM International, 2012.

AMERICAN SOCIETY FOR TESTING AND MATERIALS. **Standard guide for conducting and evaluating galvanic corrosion tests in electrolytes**, ASTM International, 2014. a.

AMERICAN SOCIETY FOR TESTING AND MATERIALS. **Standard guide for development and use of a galvanic series for predicting galvanic corrosion performance**, ASTM International, 2014. b.

AMERICAN SOCIETY FOR TESTING AND MATERIALS. **Standard practice for conventions applicable to electrochemical measurements in Corrosion Testing**, ASTM International, 2014. c.

AQION. **Hydrochemistry**. 2018. Available in: <http://www.aqion.de/>. Access in: 2 Jul. 2018.

ATLAS STEELS (ED.). **Atlas tech note No. 7**, 2010.

AZOULAY, I. **Corrosion des aciers à long terme : propriétés physico-chimiques des hydroxysels ferreux**. 2013. PhD - l'Université de La Rochelle, La Rochelle, France, 2013.

BABOIAN, R. et al. (EDS.). **Galvanic and pitting corrosion - field and laboratory studies**. West Conshohocken, United States of America: ASTM International, 1976.

BAI, Y.; BAI, Q. **Subsea engineering handbook**. Burlington, United States of America: Gulf Professional Pub, 2010.

BAI, Y.; BAI, Q. Design of Deepwater Risers. In: **Subsea Engineering Handbook**. Second Edition ed. Oxford, United Kingdom: Elsevier, 2019. v. 4p. 968.

BARKER, R. et al. A review of iron carbonate ($FeCO_3$) formation in the oil and gas industry. **Corrosion Science**, v. 142, p. 312–341, 2018.

BENJELLOUN-DABAGHI, Z. et al. MOLDI^{TM}: a fluid permeation model to calculate the annulus composition in flexible pipes. **Oil & Gas Science and Technology**, v. 57, n. 2, p. 177–192, 2002.

BORGES, M. F. **Correlação numérica-experimental da redução da vida em fadiga de dutos flexíveis operando com anular alagado na presença de CO_2.** 2017. PhD - Universidade Federal do Rio Grande do Sul, Porto Alegre, Brazil, 2017.

BRAESTRUP, M. W. et al. **Design and installation of marine pipelines**. 1. ed. Oxford, United Kingdom: Blackwell Science, 2005.

BRONDEL, D. et al. **Corrosion in the oil industry**, Schlumberger Limited, 1994.

CARROLL, J. J.; SLUPSKY, J. D.; MATHER, A. E. The solubility of carbon dioxide in water at low pressure. **Journal of Physical and Chemical Reference Data**, v. 20, n. 6, p. 1201–1209, 1991.

CHEMISTRY BLOG. **Chemistry Lab Demonstrations: LIQUID CO_2 Extraction**, 2018. Available in: <http://www.chemistry-blog.com/2009/02/04/chemistry-lab-demonstrations-liquid-co2-extraction/>. Access in: 29 Jun. 2018.

CHETWYND, G. Petrobras acts to quell rising corrosion fears. **Upstream**, p. 5, 2017.

CHOI, Y.-S.; NEŠIĆ, S. Determining the corrosive potential of CO_2 transport pipeline in high pCO_2–water environments. **International Journal of Greenhouse Gas Control**, v. 5, n. 4, p. 788–797, 2011.

CHOU, Y.-M.; POLANSKY, A. M.; MASON, R. L. Transforming non-normal data to normality in statistical process control. **Journal of Quality Technology**, v. 30, n. 2, p. 133–141, 1998.

CLEMENTS, R. Corrosion assessment prediction for a confined flexible pipe annulus. In: THE EUROPEAN CORROSION CONGRESS 2008, Edinburgh, United Kingdom. In: EUROCORR. Edinburgh, United Kingdom: DECHEMA e. V., 2008.

CLEMENTS, R.; ETHRIDGE, A. D. Corrosion testing of armour wire in simulated annulus environments of flexible pipelines - An update. In: 22ND INTERNATIONAL

CONFERENCE ON OCEAN, OFFSHORE AND ARCTIC ENGINEERING 2003, Cancun, Mexico. In: OMAE. Cancun, Mexico: ASME, 2003.

CROLET, J. L.; THEVENOT, N.; NEŠIĆ, S. Role of conductive corrosion products in the protectiveness of corrosion layers. **CORROSION**, v. 54, n. 3, p. 194–203, 1998.

DAVIS, J. R. **Corrosion: understanding the basics**. Materials Park, United States of America: ASM International, 2000.

DE ALMEIDA, S. R. M. **Solubility measurements for supercritical CO_2 in polymers for offshore applications**. 2012. MSc - Universidade do Porto, Porto, Portugal, 2012.

DE MIRANDA, R. G. **Um modelo para a análise da capacidade de processos com ênfase na transformação de dados**. 2005. MSc - Universidade Federal de Santa Catarina, Florianópolis, Brazil, 2005.

DE NEGREIROS, L. A. S. **Avaliação da resistência à fadiga e corrosão-fadiga de arames corroídos de armadura de tração de um riser flexível retirado de operação**. 2016. MSc - Porto Alegre, Brazil, 2016.

DE SOUSA, J. R. M. **Análise numérica de risers flexíveis**. 1999. MSc - Universidade Federal do Rio de Janeiro, Rio de Janeiro, Brazil, 1999.

DE SOUSA, J. R. M. et al. On the axisymmetric response of a damaged flexible pipe. In: 33RD INTERNATIONAL CONFERENCE ON OCEAN, OFFSHORE AND ARCTIC ENGINEERING 2014, San Francisco, United States of America. In: OMAE. San Francisco, United States of America: ASME, 2014.

DENZINE, A. F.; READING, M. S. A critical comparison of corrosion monitoring techniques used in industrial applications. In: CORROSION 1997 1997, New Orleans, United States of America. In: CORROSION. New Orleans, United States of America: NACE International, 1997.

DÉSAMAIS, N.; TARAVEL-CONDAT, C. On the beneficial influence of a very low supply of H_2S on the hydrogen embrittlement resistance of carbon steel wires in flexible pipe annulus. In: OFFSHORE TECHNOLOGY CONFERENCE 2009, Houston, United States of America. In: OTC. Houston, United States of America: OTC, 2009.

DOS SANTOS, F. P. **Avaliação dos efeitos da pressão parcial de CO_2 no processo de corrosão-fadiga em armaduras de tração de dutos flexíveis**. 2011. MSc - Centro Federal de Educação Tecnológica, Rio de Janeiro, Brazil, 2011.

DUGSTAD, A. et al. Corrosion testing of steel armour wires in flexible pipes – a parametric study. In: CORROSION 2015 2015, Houston, United States of America. In: CORROSION. Houston, United States of America: NACE International, 2015.

DUGSTAD, A. et al. Corrosion of steel armour wires in flexible pipes - history effects. In: SPE INTERNATIONAL OILFIELD CORROSION CONFERENCE AND EXHIBITION 2018, Aberdeen, Scotland. In: SOCIETY OF PETROLEUM ENGINEERS. Aberdeen, Scotland

EL MILIGY, A. A.; GEANA, D.; LORENZ, W. J. A theoretical treatment of the kinetics of iron dissolution and passivation. **Electrochimica Acta**, v. 20, n. 4, p. 273–281, 1975.

ERIKSEN, M.; ENGELBRETH, K. I. Outer cover damages on flexible pipes: corrosion and integrity challenges. In: 33RD INTERNATIONAL CONFERENCE ON OCEAN, OFFSHORE AND ARCTIC ENGINEERING 2014, San Francisco, United States of America. In: OMAE. San Francisco, United States of America: ASME, 2014. Access in: 25 May 2018.

FANG, H.; BROWN, B.; NEŠIĆ, S. Sodium chloride concentration effects on general CO_2 corrosion mechanisms. **CORROSION**, v. 69, n. 3, p. 297–302, 2013.

FERGESTAD, D.; LØTVEIT, S. A. **Handbook on design and operation of flexible pipes**. Trondheim, Norway: 4Subsea AS, 2014.

GENTIL, V. **Corrosão**. 6. ed. Rio de Janeiro, Brazil: LTC, 2011.

GHALI, E. **Corrosion resistance of aluminum and magnesium alloys: understanding, performance, and testing**. Hoboken, United States of America: John Wiley & Sons, Inc., 2010.

GIBBS, J. W. A method of geometrical representation of the thermodynamic properties of substances by means of surfaces. **Transactions of the Connecticut Academy of Arts and Sciences**, New Haven, United States of America, v. 2, p. 382–404, 1873.

GLEJBØL, K. **A flexible unbonded pipe and an offshore system**, WO/2011/120525, 2011.

HAAHR, M. et al. H_2S consumption and the derivation of a new annulus prediction model for offshore flexible pipes. In: 35TH INTERNATIONAL CONFERENCE ON OCEAN, OFFSHORE AND ARCTIC ENGINEERING 2016, Busan, South Korea. In: OMAE. Busan, South Korea: ASME, 2016.

HAN, J. et al. Electrochemical investigation of localized CO_2 corrosion on mild steel. In: CORROSION 2007 2007, Houston, United States of America. In: CORROSION. Houston, United States of America: NACE International, 2007.

HANGX, S. J. T. **Rate of CO_2 mineralisation and geomechanical effects on host and seal formations**. Utrecht, Nederlands: Utrecht University, 2005.

HEIDERSBACH, R. **Metallurgy and corrosion control in oil and gas production**. Hoboken, United States of America: John Wiley & Sons, Inc., 2011.

HENRY, W. Experiments on the quantity of gases absorbed by water, at different temperatures, and under different pressures. **Philosophical Transactions of the Royal Society**, London, United Kingdom, v. 93, p. 29–43, 1803. III.

HERNANDEZ, J.; MUÑOZ, A.; GENESCA, J. Formation of iron-carbonate scale-layer and corrosion mechanism of API X70 pipeline steel in carbon dioxide-saturated 3% sodium chloride. **Afinidad**, v. 560, p. 251–258, 2012.

JOEL, J. **Reinforcing wire corrosion in flexible pipe**. Derbyshire, United Kingdom: Health & Safety Laboratory, 2009.

KAHYARIAN, A.; BROWN, B.; NEŠIĆ, S. Mechanism of CO_2 corrosion of mild steel: a new narrative. In: CORROSION 2018 2018, Houston, United States of America. In: CORROSION. Houston, United States of America: NACE International, 2018.

KE, L. et al. Optimizing the design of unbonded flexible pipelines with more realistic predictions of pH and H_2S content in the annulus. In: 36TH INTERNATIONAL CONFERENCE ON OCEAN, OFFSHORE AND ARCTIC ENGINEERING 2017, Trondheim, Norway. In: OMAE. Trondheim, Norway: ASME, 2017.

KELLY, R. et al. **Electrochemical techniques in corrosion science and engineering**. New York, United States of America: CRC Press, 2002.

KERMANI, M. B.; MORSHED, A. Carbon dioxide corrosion in oil and gas production - a compendium. **CORROSION**, v. 59, n. 8, p. 659–683, 2003.

KLOPFFER, M. H.; FLACONNECHE, B. Transport properties of gases in polymers: bibliographic review. **Oil & Gas Science and Technology**, v. 56, n. 3, p. 223–244, 2001.

KORDAČ, M.; LINEK, V. Dynamic measurement of carbon dioxide volumetric mass transfer coefficient in a well-mixed reactor using a pH probe: analysis of the salt and supersaturation effects. **Industrial & Engineering Chemistry Research**, v. 47, n. 4, p. 1310–1317, 2008.

KRISHNAMOORTHY, K.; MATHEW, T. **Statistical tolerance regions: theory, applications, and computation**. Hoboken, United States of America: John Wiley & Sons, Inc., 2009. Access in: 31 Jul. 2018.

LANGLO, S. A. W. **Enhanced Oil Recovery by CO_2 and CO_2-foam injection in fractured limestone rocks**. 2013. MSc - University of Bergen, Bergen, Norway, 2013.

LEMOS, M. F. **Avaliação da vida em fadiga de juntas soldadas do aço API 5L X65 em meios aquosos salinos saturados com diferentes pressões parciais de CO_2**. 2009. MSc - Universidade Federal do Rio Grande do Sul, Porto Alegre, Brazil, 2009.

LIN, H.; FREEMAN, B. D. Gas solubility, diffusivity and permeability in poly(ethylene oxide). **Journal of Membrane Science**, v. 239, n. 1, p. 105–117, 2004.

LIU, Z. et al. Corrosion behaviour of low-alloy martensite steel exposed to vapour-saturated CO_2 and CO_2-saturated brine conditions. **Electrochimica Acta**, v. 213, p. 842–855, 2016.

LIU, Z.-G. et al. Comparison of corrosion mechanism of low-alloy pipeline steel used for flexible pipes at vapor-saturated CO_2 and CO_2-saturated brine conditions. **Materials and Corrosion**, v. 68, n. 11, p. 1200–1211, 2017.

LOPEZ, D. A. et al. The influence of carbon steel microstructure on corrosion layers An XPS and SEM characterization. **Applied Surface Science**, v. 207, n. 1–4, p. 69–85, 2003.

LÓPEZ, D. A.; PÉREZ, T.; SIMISON, S. N. The influence of microstructure and chemical composition of carbon and low alloy steels in CO_2 corrosion. A state-of-the-art appraisal. **Materials & Design**, v. 24, n. 8, p. 561–575, 2003.

MAJER, V.; SEDLBAUER, J.; BERGIN, G. Henry's law constant and related coefficients for aqueous hydrocarbons, CO_2 and H_2S over a wide range of temperature and pressure. **Fluid Phase Equilibria**, v. 272, p. 65–74, 2008.

MITZITHRA, M. E.; PAUL, S. Corrosion performance of API 5l X65 steel in a low temperature saline environment containing CO_2. In: CORROSION 2016 2016, Houston, United States of America. In: CORROSION. Houston, United States of America: NACE International, 2016.

MOHAMED, M. F. et al. Water chemistry for corrosion prediction in high-pressure CO_2 environments. In: CORROSION 2011 2011, Houston, United States of America. In: CORROSION. Houston, United States of America: NACE International, 2011.

MORA-MENDOZA, J.; TURGOOSE, S. Fe3C influence on the corrosion rate of mild steel in aqueous CO_2 systems under turbulent flow conditions. **Corrosion Science**, v. 44, n. 6, p. 1223–1246, 2002.

MORAN, M. J.; SHAPIRO, H. N. **Princípios de termodinâmica para engenharia**. 4. ed. Rio de Janeiro: LTC, 2002.

MUREN, J. **Failure modes, inspection, testing and monitoring**, SEAFLEX, 2007.

NAITO, Y. et al. Permeation of high-pressure gases in poly(ethylene-co-vinyl acetate). **Journal of Polymer Science Part B: Polymer Physics**, v. 31, n. 6, p. 693–697, 1993.

NEŠIĆ, S. Key issues related to modelling of internal corrosion of oil and gas pipelines – A review. **Corrosion Science**, v. 49, n. 12, p. 4308–4338, 2007.

NEŠIĆ, S.; POSTLETHWAITE, J.; OLSEN, S. An electrochemical model for prediction of corrosion of mild steel in aqueous carbon dioxide solutions. **CORROSION**, v. 52, n. 4, p. 280–294, 1996.

NOV. **Flexibles**, National Oilwell Varco, 2015.

ODEH, R. E. Tables of two-sided tolerance factors for a normal distribution. **Communications in Statistics - Simulation and Computation**, v. 7, n. 2, p. 183–201, 1978.

OLDONI, V. P.; RIBEIRO, R. F.; WERNER, L. Análise de capacidade de um processo siderúrgico: utilização de transformação de dados para processo não-normal. In: XXII SIMPEP 2015, Bauru, Brazil. In: SIMPÓSIO DE ENGENHARIA DE PRODUÇÃO. Bauru, Brazil: SIMPEP, 2015.

OLI STUDIO (ED.). **A guide to using OLI Studio/OLI Analyzer Stream**, 2016.

ORGANIZATION OF THE PETROLEUM EXPORTING COUNTRIES. **World oil outlook 2040**. Vienna, Austria. Available in: <http://www.opec.org>

PATIL, V. E. et al. Permeation of supercritical carbon dioxide through polymeric hollow fiber membranes. **Journal of Membrane Science**, v. 271, n. 1–2, p. 77–85, 2006.

PAUL, S. **Materials technology gap analysis for handling CO₂ in carbon capture and storage (CCS) and oil and gas service.** Cambridge, United Kingdom: The Welding Institute, 2010.

PEREZ, N. **Electrochemistry and corrosion science**. Boston, United States of America: Kluwer Academic Publishers, 2004.

POURBAIX, M. J. N. **Thermodynamique des solutions aqueuses diluées representation graphique du róle du pH et du potentiel**. 1945. PhD - Technische Universiteit Delft, Delft, Nederland, 1945.

POURBAIX, M. J. N. **Lições de corrosão electroquímica**. 3. ed. Brussels, Belgium: CEBELCOR, 1987.

REMITA, E. et al. Experimental and theoretical investigation of the uniform corrosion in the annulus of offshore flexible pipelines. In: CORROSION 2008 2008, Houston, United States of America. In: CORROSION. Houston, United States of America: NACE International, 2008.

RIBEIRO, R. F. **Avaliação da resistência à corrosão de uma junta de aço inoxidável dúplex UNS S31803 soldada por processo a fricção com pino consumível**. 2014. MSc - Universidade Federal do Rio Grande do Sul, Porto Alegre, Brazil, 2014.

ROBERGE, P. R. **Handbook of corrosion engineering**. New York, United States of America: McGraw-Hill, 2000.

ROGOWSKA, M. et al. Effect of Fe ion concentration on corrosion of carbon steel in CO₂ environment. **Corrosion Engineering, Science and Technology**, v. 51, n. 1, p. 25–36, 2016.

ROPITAL, F. et al. Methodology to study the general corrosion of steel armours in simulated conditions of flexible pipe annulus influence of confinement and evaluation of the pH. In: EUROCORR 2000, London, United Kingdom. In: THE EUROPEAN CORROSION CONGRESS. London, United Kingdom

ROSLI, N. R. et al. Corrosion of UNS G10180 steel in supercritical and subcritical CO₂ with O2 as a contaminant. In: CORROSION 2016 2016, Houston, United States of America. In: CORROSION. Houston, United States of America: NACE International, 2016.

RUBIN, A. et al. Corrosion rates of carbon steel in confined environments. In: CORROSION 2012 2012, Houston, United States of America. In: CORROSION. Houston, United States of America: NACE International, 2012.

SANDER, R. Compilation of Henry's law constants (version 4.0) for water as solvent. **Atmospheric Chemistry and Physics**, v. 15, n. 8, p. 4399–4981, 2015.

SANTOS, F. et al. Corrosion fatigue behavior of flexible pipe tensile armor wires in a CO₂ environment. **Materials Science Forum**, v. 758, p. 77–82, 2013.

SCHMITT, G.; HÖRSTEMEIER, M. Fundamental aspects of CO₂ metal loss corrosion – Part II: influence of different parameters on CO₂ corrosion mechanisms. In: CORROSION 2006 2006, Houston, United States of America. In: CORROSION. Houston, United States of America: NACE International, 2006.

SCHÜTZE, M.; ISECKE, B.; BENDER, R. **Corrosion protection against carbon dioxide**. Frankfurt, Germany: John Wiley & Sons, 2011. v. 1

SCRIPPS INSTITUTION OF OCEANOGRAPHY. **Educational resources in earth, marine, environmental and planetary sciences**. 2013. Available in: <http://earthguide.ucsd.edu/>. Access in: 14 Jul. 2018.

SK, M. H. et al. Local supersaturation and the growth of protective scales during CO_2 corrosion of steel: Effect of pH and solution flow. **Corrosion Science**, v. 126, p. 26–36, 2017.

STANDARDS NORWAY. **CO_2 corrosion rate calculation model**, STANDARDS NORWAY, 2005.

SUHOR, M. F. et al. Corrosion of mild steel in high CO_2 environment: effect of FeCO3 layer. In: CORROSION 2012 2012, Houston, United States of America. In: CORROSION. Houston, United States of America: NACE International, 2012.

SUN, W. **Kinetics of iron carbonate and iron sulfide scale formation in CO_2/H_2S corrosion**. 2006. PhD - Russ College of Engineering and Technology of Ohio University, Ohio, United States of America, 2006.

SUN, W.; NEŠIĆ, S. Kinetics of corrosion layer formation: Part 1—Iron carbonate layers in carbon dioxide corrosion. **CORROSION**, v. 64, n. 4, p. 334–346, 2008.

SYED, S. Atmospheric corrosion of carbon steel at marine sites in Saudi Arabia. **Materials and Corrosion**, v. 61, n. 3, p. 238–244, 2010.

TANUPABRUNGSUN, T. et al. Construction and verification of Pourbaix diagrams for CO_2 corrosion of mild steel valid up to 250 °C. In: CORROSION 2012 2012, Houston, United States of America. In: CORROSION. Houston, United States of America: NACE International, 2012.

TARAVEL-CONDAT, C.; GUICHARD, M.; MARTIN, J. MOLDI^{TM}: a fluid permeation model to calculate the annulus composition in flexible pipes — validation with medium scale tests, full scale tests and field cases. In: 22ND INTERNATIONAL CONFERENCE ON OFFSHORE MECHANICS AND ARCTIC ENGINEERING 2003, Cancun, Mexico. In: OMAE. Cancun, Mexico: ASME, 2003.

TECHNIP. **Flexible pipe**, 2015.

THOMAS, M. **A rising tide**. 2012. Available in: <https://www.epmag.com/rising-tide-685301>. Access in: 16 Oct. 2018.

THU, T.; BROWN, B.; NEŠIĆ, S. Corrosion of mild steel in an aqueous CO_2 environment – basic electrochemical mechanisms revisited. In: CORROSION 2015 2015, Houston. In: CORROSION. Houston: NACE International, 2015.

TRELLEBORG. **Distributed buoyancy modules - subsea buoyancy**. 2018. Available in: <http://www.trelleborg.com/en/offshore/products/subsea--buoyancy/subsea--distributed--buoyancy--modules>. Access in: 11 Jun. 2018.

UNDERWOOD, N. J. Corrosion testing of reinforcement in simulated annulus environments of flexible pipelines. In: 21ST INTERNATIONAL CONFERENCE ON OFFSHORE MECHANICS 2002, Oslo, Norway. In: OMAE. Oslo, Norway: ASME, 2002.

UNIVERSITY OF CAMBRIDGE. **Kinetics of aqueous corrosion**. 2018. Available in: <https://www.doitpoms.ac.uk/tlplib/aqueous_corrosion/intro.php>. Access in: 24 Jun. 2018.

VAN HUNNIK, E. W. J.; POTS, B. F. M.; HENDRIKSEN, E. L. J. A. The formation of protective FeCO3 corrosion product layers in CO_2 corrosion. In: CORROSION 2016 1996, Houston, United States of America. In: CORROSION. Houston, United States of America: NACE International, 1996.

WOLYNEC, S. **Técnicas eletroquímicas em corrosão**. São Paulo, Brazil: EDUSP, 2003.

WORLEYPARSONS. **Subsea 7 riser buoys**. 2015. Available in: <http://offshore.worleyparsons.com/project/subsea-7-riser-buoys/>. Access in: 11 Jun. 2018.

XAVIER, F. G. **Avaliação da vida em fadiga de um novo modelo de terminal conector para dutos flexíveis**. 2009. PhD - Universidade Federal do Rio Grande do Sul, Porto Alegre, Brazil, 2009.

YANG, Y. **Removal mechanisms of protective iron carbonate layer in flowing solutions**. 2012. PhD - Russ College of Engineering and Technology of Ohio University, Ohio, United States of America, 2012.
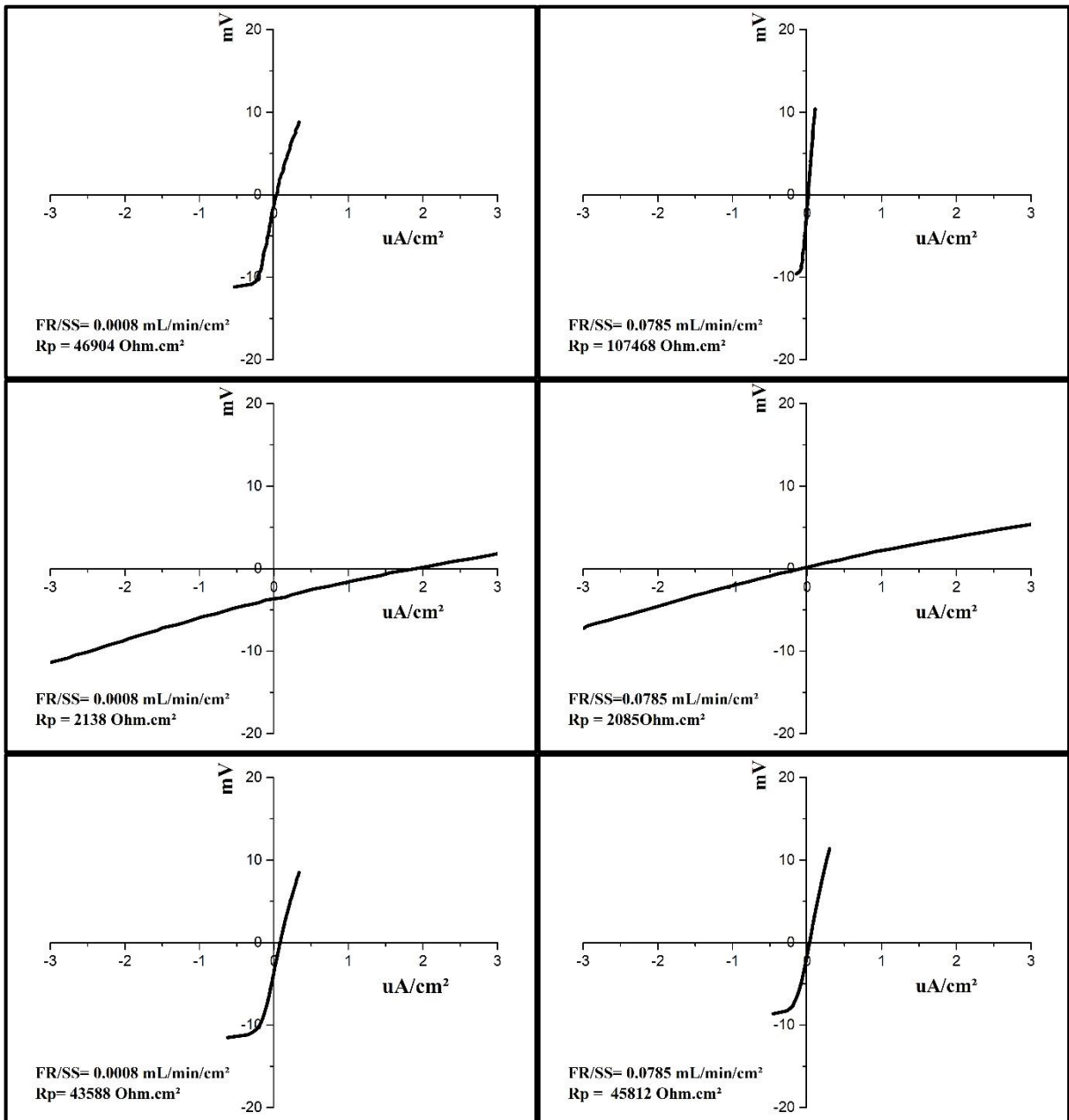
ZENG, Z.; LILLARD, R. S.; CONG, H. Effect of salt concentration on the corrosion behavior of carbon steel in CO_2 environment. **Corrosion**, v. 72, n. 6, p. 805–823, 2016.

APPENDIX

A.   Linear polarisation resistance:

Figure 87 shows examples of the LPR in the different stages of evolution (I, II and III).

Figure 87: Examples of linear polarisation resistance plots obtained in this work.
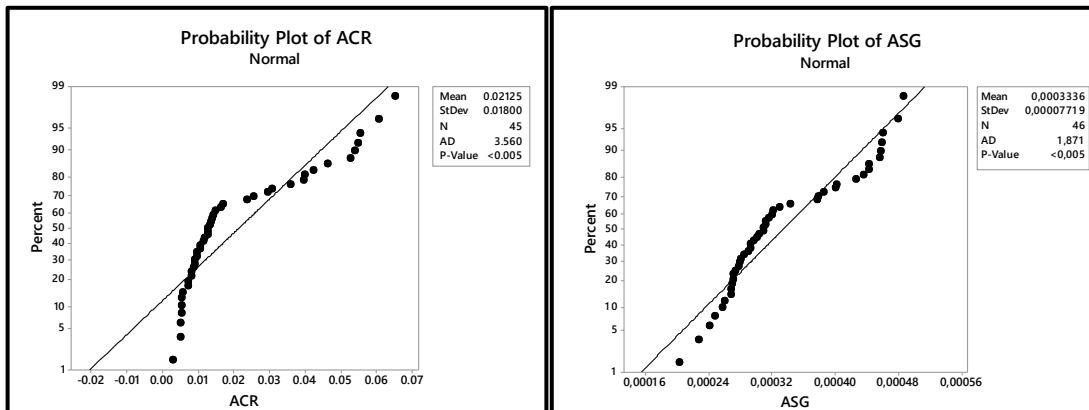

Source: AUTHOR.

B.   Normality test:

Figure 88 presents the normality tests for the low flow rate experiment. The plots show a P-value greater than 0.005, which means that the null hypothesis is accepted and the probability that both plots are normally distributed is greater than 95%. Figure 89 reveals the normality tests for the high flow rate experiment, where the data cannot be regarded as normally distributed once the P-value is below 0.005.

Figure 88: Normality test of ACR and ASG. Test conditions: V/S of 0.2 ml/cm², 3.5%wt. NaCl brine, FR/SS of 0.0008 ml.min^{-1}.cm^{-2}, 1 atm of CO_2 and 30±2 °C.
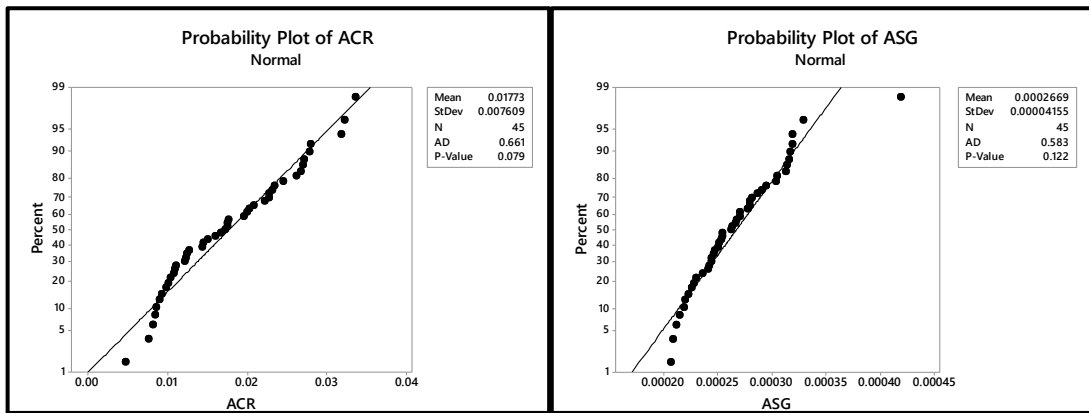
Source: AUTHOR.

Figure 89: Normality test of ACR and ASG. Test conditions: V/S of 0.2 ml/cm², 3.5%wt. NaCl brine, FR/SS of 0.0785 ml.min^{-1}.cm^{-2}, 1 atm of CO_2 and 30±2 °C.
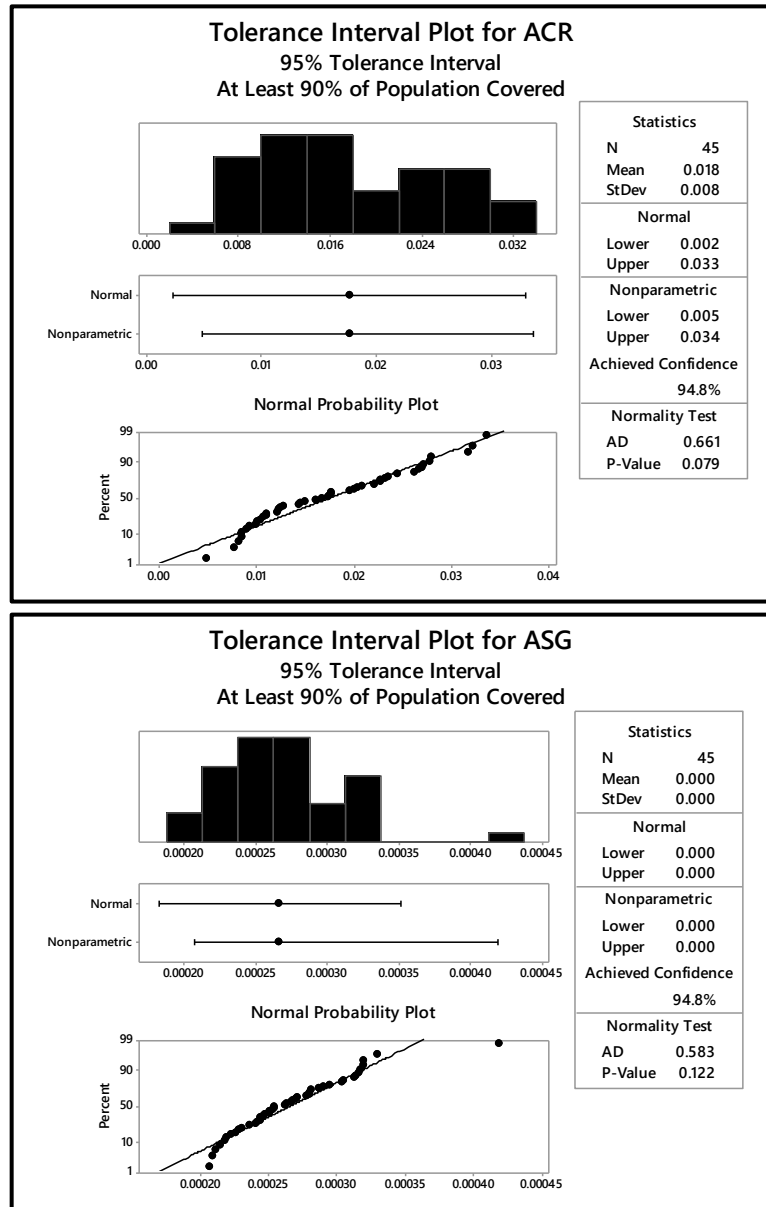

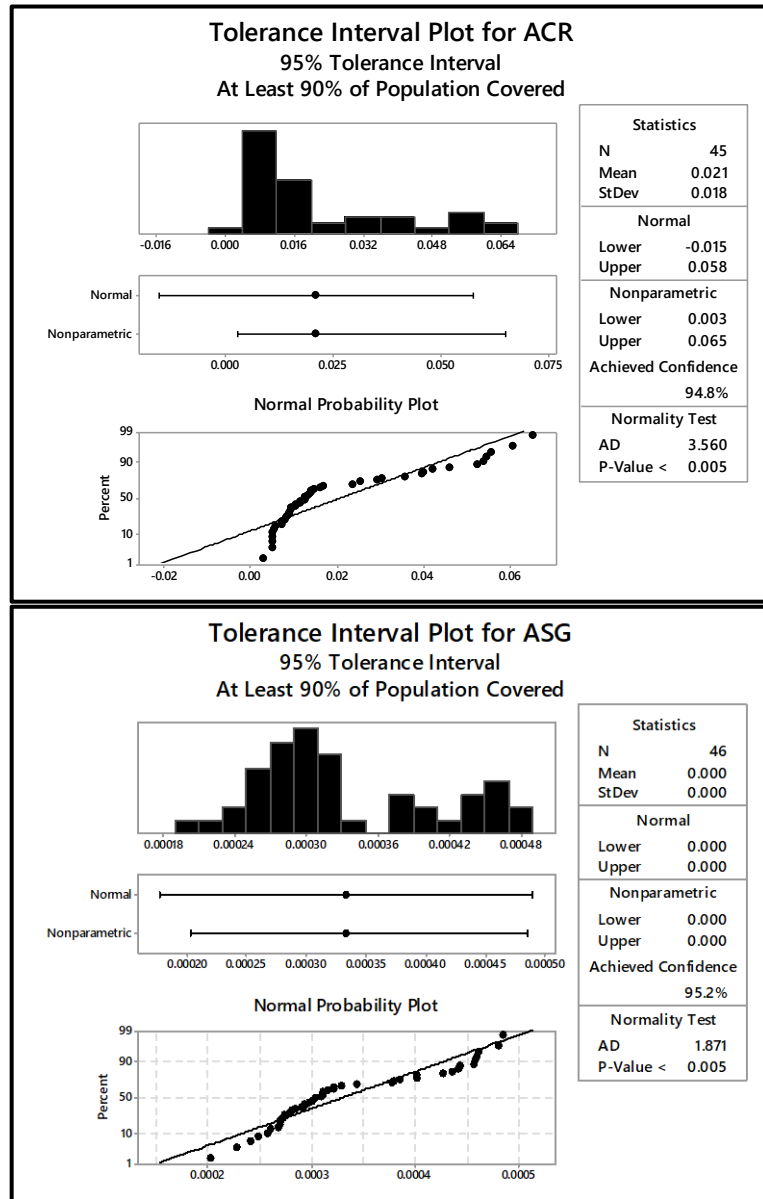Source: AUTHOR.

C.   Tolerance interval:

Figure 90 and Figure 91 show the results of the tolerance intervals.

Figure 90: Tolerance intervals of ACR and ASG. Test conditions: V/S of 0.2 ml/cm², 3.5%wt. NaCl brine, FR/SS of 0.0008 ml.min^{-1}.cm^{-2}, 1 atm of CO_2 and 30±2 °C.

Source: AUTHOR.

Figure 91: Tolerance intervals of ACR and ASG. Test conditions: V/S of 0.2 ml/cm², 3.5%wt. NaCl brine, FR/SS of 0.0785 ml.min⁻¹.cm⁻², 1 atm of CO_2 and 30±2 °C.
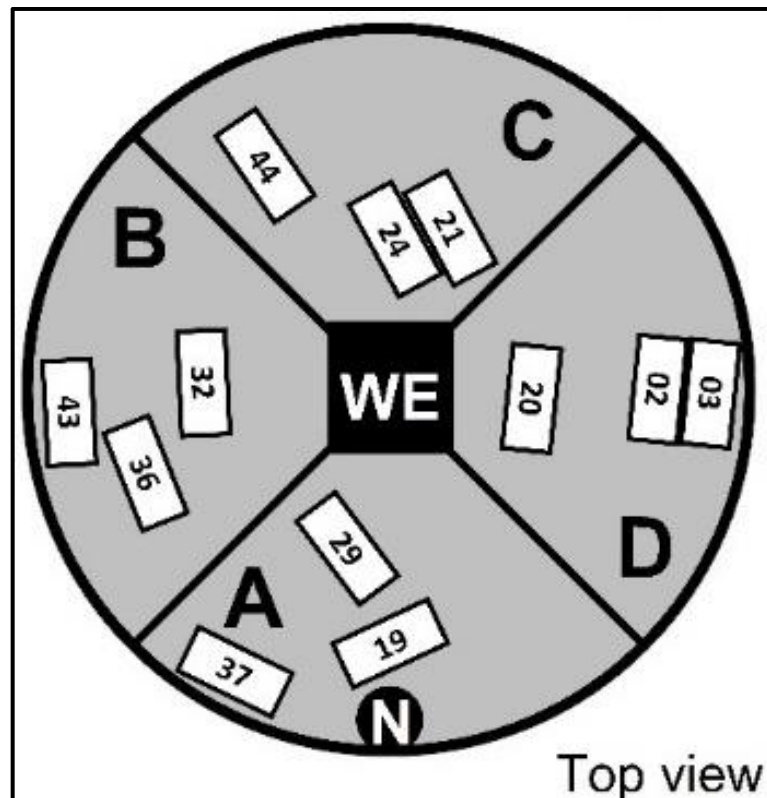

Source: AUTHOR.

D. Verification of the effect of the geometry of the test vessel

The results of experimental investigations shall not be a function of experimental setups themselves, but from the studied variables instead. Accordingly, the proximity of the samples to the inlet nozzle was investigated to observe whether geometry affects or not the ACR and ASG. Ideally, the corrosion rates and scale growth must remain independent from the test setup. Bearing that in mind, Figure 92 shows a sketch of the test vessel demonstrating the identification number and the position of the samples in respect to the inlet nozzle (N). The sketch shows zone A, closer to the inlet nozzle, zones B and D, at intermediate distances, and

zone C, further distant from the nozzle. Figure 93.a. shows the results of the ACR analysis, which reveal similar mean values and amplitudes despite the various distances to the inlet nozzle. Figure 93.b. show comparable ASG for the zones A, B and C but a considerable variation for zone D. Such variation is explained by the presence of the sample #02 in the calculus, once this sample was identified as an outlier (see Table 11), meaning that the variation of zone D can be disregarded. Therefore, the analysis of the geometry of the test vessel indicates that the samples corroded in similar atmospheres, independent from the distance to the inlet nozzle or geometry of the test vessel. Moreover, the result confirms the work of Rubin et al. (2012) that observed no correlation with the position of the CO_2.

Figure 92: A sketch of the test vessel and samples, grouped by the proximity to the inlet nozzle (N). The working electrodes (WE) are positioned in the centre of the vessel. Zone A - samples closer to the inlet nozzle. Zones B and D - samples at intermediate distances to the inlet nozzle. Zone C – samples at the largest distance to the inlet nozzle. Test conditions: V/S of 0.2 ml/cm², 3.5%wt. NaCl brine, FR/SS of 0.0008 ml.min^{-1}.cm^{-2}, 1 atm of CO_2 and 30±2 °C.
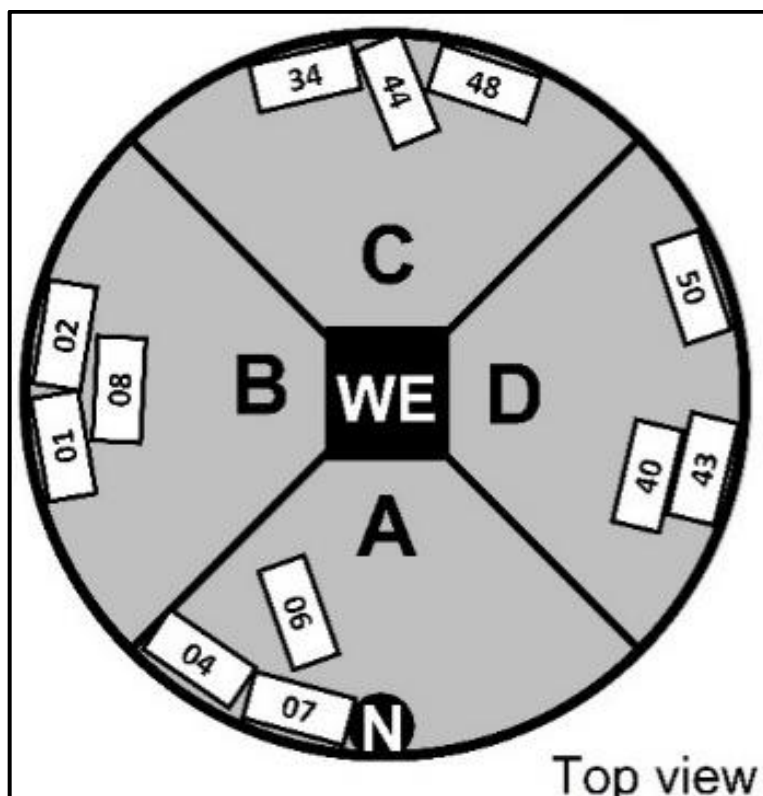

Source: AUTHOR.

Figure 93: Means and amplitudes of ACR and ASG, in respect to the proximity to the inlet nozzle. The grey horizontal lines show the tolerance interval. Test conditions: V/S of 0.2 ml/cm², 3.5%wt. NaCl brine, FR/SS of 0.0008 ml.min^{-1}.cm^{-2}, 1 atm of CO_2 and 30±2 °C.
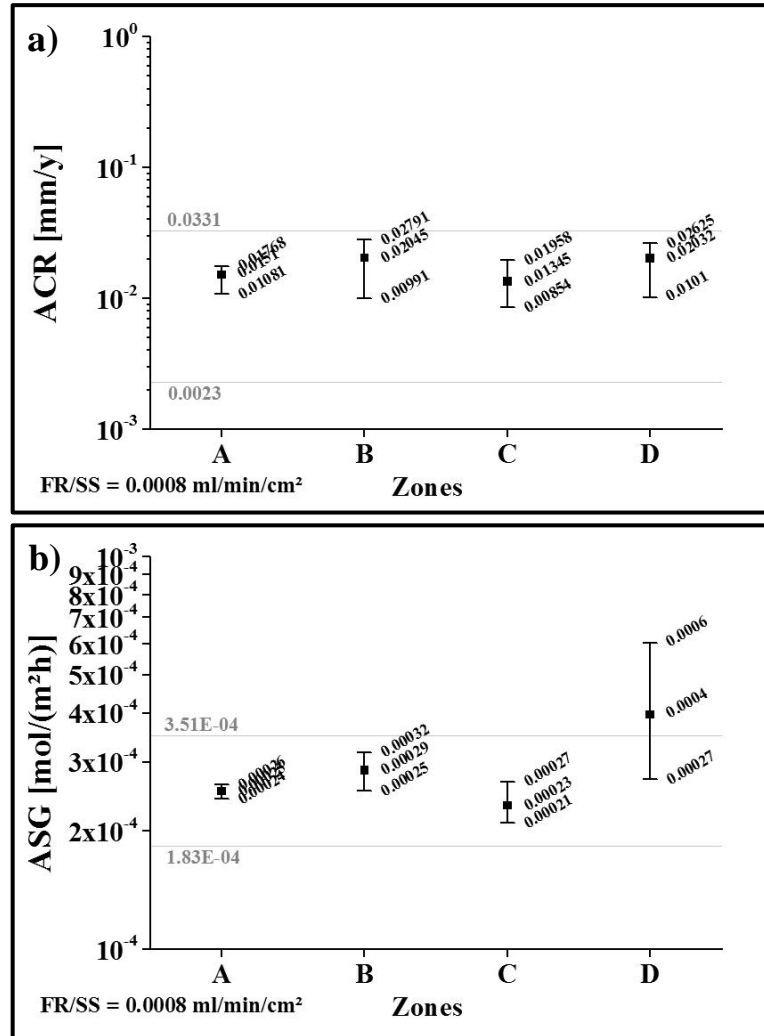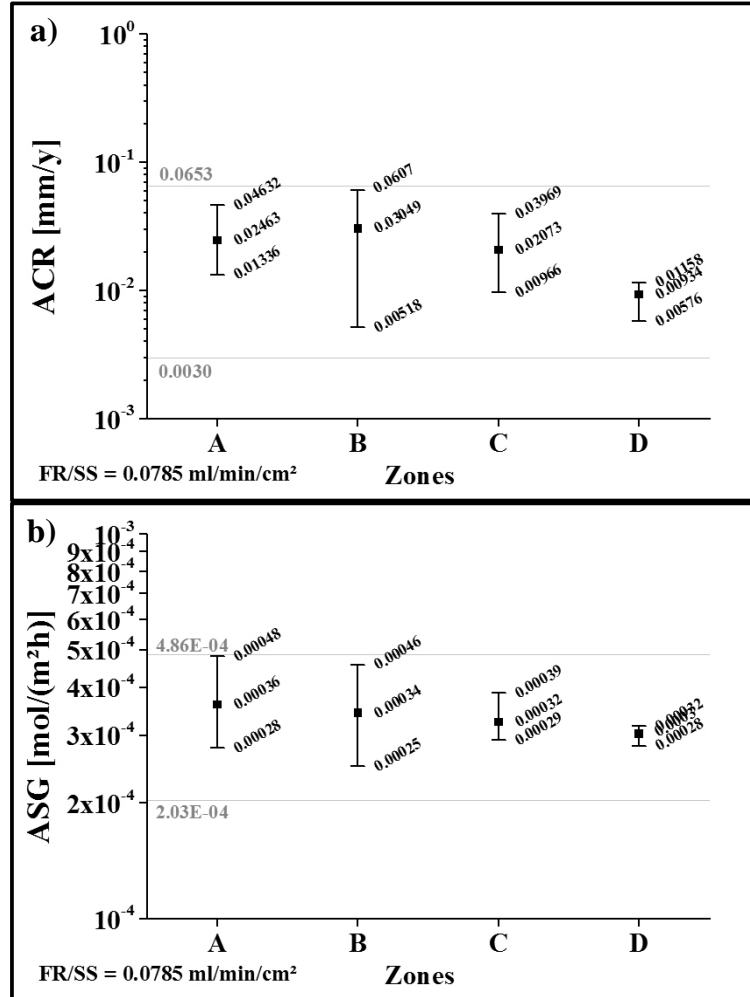

Source: AUTHOR.

A verification of the proximity of the samples to the inlet nozzle was also carried to identify if the vessel set up at the high flow rate condition has affected the ACR and ASG results. Figure 94 shows a sketch of the test vessel demonstrating the identification number and the position of the samples that were grouped concerning the distance of the inlet nozzle. Figure 95 shows the mean values and amplitudes of the ACR and ASG. As well as observed in the low flow rate experiments, the means and amplitudes of the results remained similar to each other despite the distances to the inlet nozzle. Then, this work assumes that all samples were tested in similar atmospheres, independent from the setup of the test vessel.

Figure 94: A sketch of the test vessel and samples, grouped by the proximity to the inlet nozzle (N). The working electrodes (WE) are positioned in the centre of the vessel. Zone A - samples closer to the inlet nozzle. Zones B and D - samples at intermediate distances to the inlet nozzle. Zone C – samples at the largest distance to the inlet nozzle. Test conditions: V/S of 0.2 ml/cm², 3.5%wt. NaCl brine, FR/SS of 0.0785 ml.min^{-1}.cm^{-2}, 1 atm of CO_2 and 30 ± 2 °C.

Source: AUTHOR.

Figure 95: Means and amplitudes of ACR and ASG, in respect to the proximity to the inlet nozzle. The grey horizontal lines show the tolerance interval. Test conditions: V/S of 0.2 ml/cm², 3.5%wt. NaCl brine, FR/SS of 0.0785 ml.min^{-1}.cm^{-2}, 1 atm of CO_2 and 30±2 °C.

Source: AUTHOR.